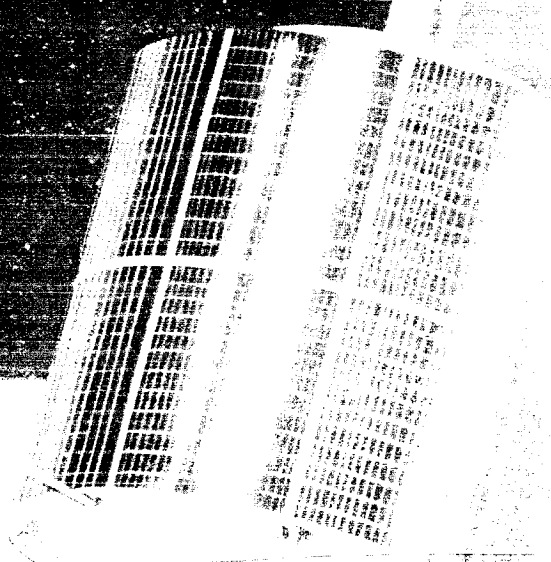


R. Dancer

SYNCO



December 1963

MONTHLY PROGRESS REPORT

NASA Contract 5-2797
SSD 31261R

FACILITY FORM 802

N66-83657	(THIRD)
(ACCESSION NUMBER)	NONE
307	(CODE)
(PAGES)	
CR 74587	(CATEGORY)
(NASA CR OR TMX OR AD NUMBER)	

AEROSPACE GROUP
SPACE SYSTEMS DIVISION
HUGHES AIRCRAFT COMPANY
CULVER CITY, CALIFORNIA

HUGHES

HUGHES AIRCRAFT COMPANY

AEROSPACE GROUP

SPACE SYSTEMS DIVISION

EL SEGUNDO, CALIFORNIA

15 December 1963

Subject: Advanced Syncom Monthly Progress
Report for December 1963
Contract NAS 5-2797

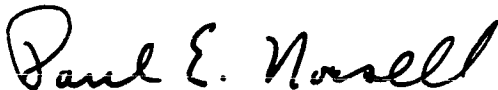
To: Mr. Robert J. Darcey
SYNCOM Project Manager
Goddard Space Flight Center, Code 621
Greenbelt, Maryland

The reaction control system study has been completed. Results of the study and recommendations were presented to GSFC personnel at a design review in mid-December. The resulting agreements with GSFC define the reaction control system for the three spacecraft configurations. Completion of structural detail is now proceeding rapidly. Thermal analysis of the spacecraft has continued and a resulting insulated design for the gravity-gradient spacecrafts has evolved.

An initial allotment of experimental packages has been made for each of the proposed launches. Power profiles, space requirements, solar panel access, and mass properties have been determined for each configuration and system integration effort is proceeding.

The Goddard and Hughes analyses of the gravity-gradient stabilization system have been integrated. Resulting spacecraft engineering considerations and dynamic limits are defined. Thermal effects, boom dynamics, boom material, and other factors have been evaluated and the results assessed relative to the program objectives.

HUGHES AIRCRAFT COMPANY



Paul E. Norsell
Manager, Advanced Syncom

cc: H. A. Zaret
Goddard Space Flight Center
Code 247
Greenbelt, Maryland

Advanced SYNCOM

December 1963

MONTHLY PROGRESS REPORT

•

*NASA Contract 5-2797
SSD 31261R*

AEROSPACE GROUP
SPACE SYSTEMS DIVISION
HUGHES AIRCRAFT COMPANY
CULVER CITY, CALIFORNIA

HUGHES

CONTENTS

	Page
1. INTRODUCTION	1-1
2. COMMUNICATION SYSTEM DESIGN AND ANALYSIS	2-1
3. LAUNCH AND ORBITAL ANALYSIS	
Launch Vehicle Payload Optimization for Medium Altitude Orbit	3-1
Preliminary Visibility Contours—Medium Altitude Orbit	3-3
Injection Error Analysis	3-9
Micro-Thrusting Intervals for Small Eccentricity	3-21
Changes of Near Circular Orbits	3-29
References	3-29
4. GRAVITY-GRADIENT STABILIZATION SYSTEM SUMMARY	4-1
System Parameter Optimization	4-16
Boom Dynamics	4-19
Structural Analysis	4-20
Structural Dynamics	4-28
Velocity Control System Study	4-32
Mechanisms	4-33
Instrumentation Package	4-37
References	4-39
5. SPACECRAFT SYSTEMS DESIGN	
General Status Report	5-1
6. EXPERIMENTAL PAYLOADS	
Meteorological Equipment	6-1
Radiation and Micrometeorite Detection Equipment	6-2
Navigation Equipment	6-4
Nuclear Arms Control Equipment	6-6
Mechanically Despun Antenna	6-8
Spacecraft Engineering Instrumentation Experiment	6-8

7.	GROUND HANDLING AND SERVICING EQUIPMENT	
	Semiautomatic System Test Equipment Recording System	7-1
	Telemetry and Command System and Control Item Test Equipment	7-3
	Communication System and Control Item Test Equipment	7-6
	Handling Equipment	7-8
8.	PROJECT REFERENCE REPORTS	8-1

1. INTRODUCTION

The Advanced Syncom spacecraft, currently under study for feasibility and advanced technological development, will demonstrate the stationary, or equatorial, synchronous orbit and the 6000 n. mi. circular orbit with a vehicle providing a relatively large, adaptable payload capability, achievement of long life in orbit, wide-band communications, and new multiple-access communications. Scientific instruments will be carried to measure the radiation environment and to assess radiation damage occurring during the orbiting process and throughout satellite life.

The spacecraft systems design is adaptable to the substitution of alternate mission payload equipment in lieu of one or more of the multiple sets of communication equipment. The systems of the spacecraft are currently being studied to define changes to optimize this alternate mission payload capability. In addition, the vehicle configurations resulting from inclusion of a Goddard gravity-gradient stabilization system, to replace the spin stabilization in some models of the spacecraft, are under study.

2. COMMUNICATION SYSTEM DESIGN AND ANALYSIS

Work is proceeding on the analysis of the communication system capabilities of projected gravity-gradient versions of Advanced Syncom spacecraft. Principal effort has been devoted to investigating the effects on multiple-access operation of the relatively high doppler rates encountered in connection with the medium altitude vehicle. The biggest difficulty appears to be the apparent spreading in frequency of the baseband due to differential doppler shift occurring between the lowest and the highest baseband channels. A writeup giving the results of this investigation is currently in preparation.

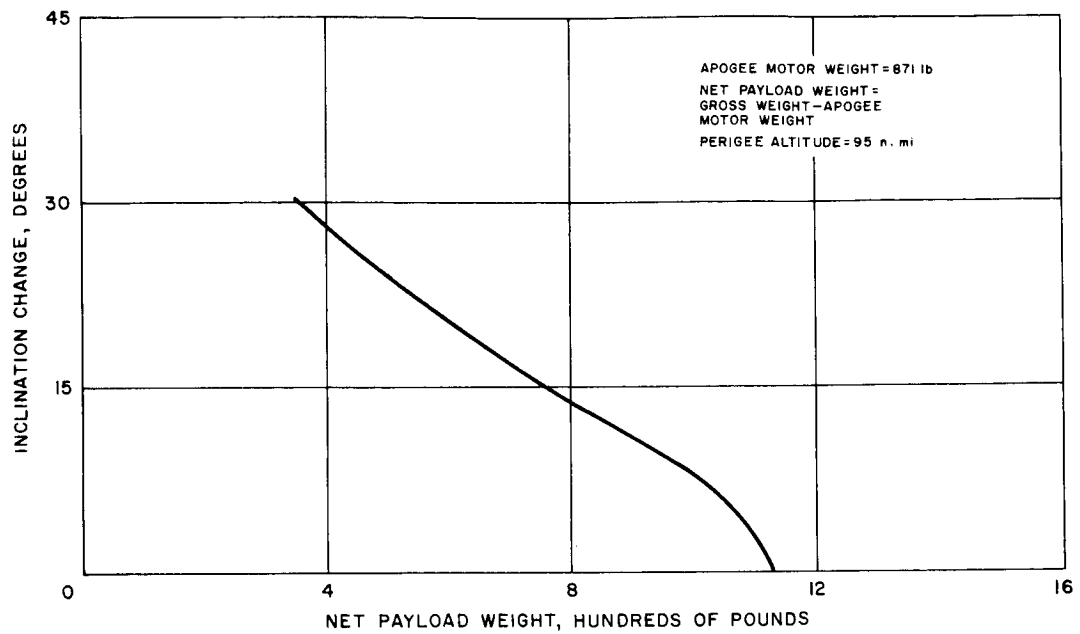
3. LAUNCH AND ORBITAL ANALYSIS

LAUNCH VEHICLE PAYLOAD OPTIMIZATION FOR MEDIUM ALTITUDE ORBIT

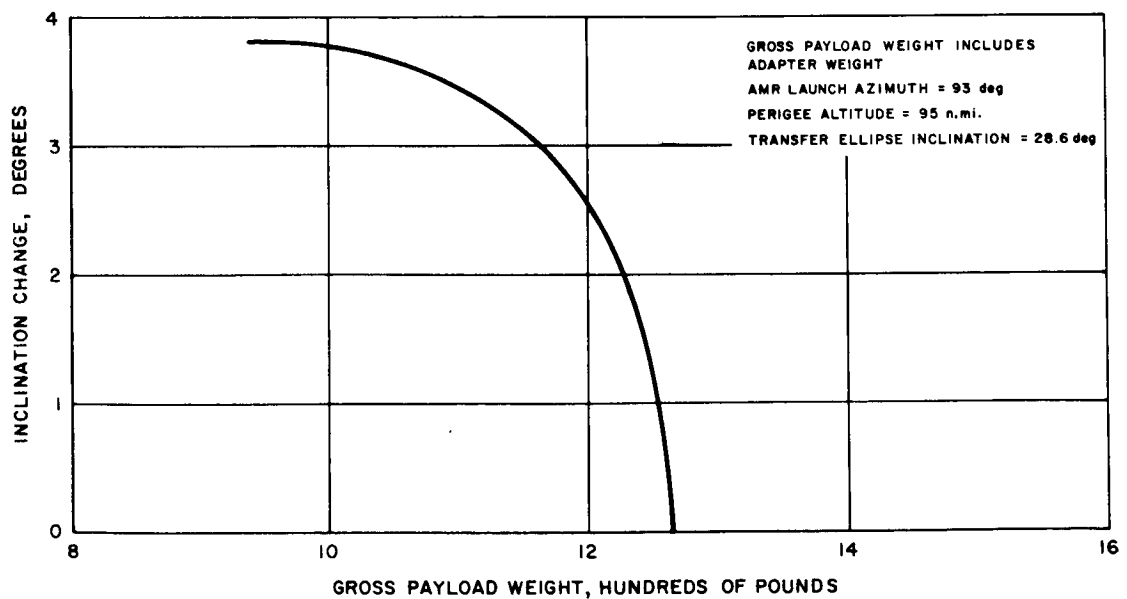
A computer simulation of the Atlas-Agena vehicle to conduct payload studies and perform trajectory analyses has been established. The Advanced Syncom spacecraft in a stationary synchronous orbit was used as a test to determine the effectiveness of the simulation. The test case checked within 10 pounds of the Advanced Syncom spacecraft payload. The test case spacecraft and orbital information for comparison came from a Hughes document on launch and orbital analysis (Reference 3-1). A payload study using an apogee motor was made for the 6000-n.mi. orbit. The Atlas and the first Agena burn were used to place the spacecraft into a 95-n.mi. circular orbit. The second Agena burn was then used to place the spacecraft into a transfer orbit with a 6000-n.mi. apogee, and the apogee motor was fired to circularize the orbit and remove as much inclination as possible. Figure 3-1 shows the change in inclination possible as a function of net payload when using the apogee motor. The net payload is the gross payload weight minus the apogee motor weight (871 pounds when fully loaded). The motor considered was the same as used in the Advanced Syncom to obtain the stationary synchronous orbit.

The payload capability of using only the dual agena firings to burn into a 6000-n.mi. circular orbit was then considered. The first Agena firing was used to place the spacecraft on a transfer orbit to a 6000-n.mi. apogee. The second Agena firing was then used to circularize and remove as much inclination as possible. Results of the Hughes simulation plotted in Figure 3-1b agrees with the reported results of Lockheed (within 10 pounds). The payload differences are due mainly to slight differences in the burning history of the Agena D. Further studies will be conducted to determine the reasons for this difference and to present a more complete study of the dual Agena payload capability. Tentative conclusions indicated by Figure 3-1b are:

- 1) Only small inclination changes are feasible with a dual Agena burn
- 2) Missions requiring large inclination changes should employ either a triple Agena burn or a dual burn with a solid apogee motor.



a) With Apogee Motor



b) With Dual Agena Burn

Figure 3-1. Possible Inclination Changes for 6000 n.mi. Circular Orbit

Consideration was given to using the Agena for a triple burn. However, because of the expense and time involved in booster modification and requalification, the investigation was terminated.

PRELIMINARY VISIBILITY CONTOURS - MEDIUM ALTITUDE ORBIT

The following discussion of visibility from various ground stations is presented to facilitate the planning of suitable stations equipped with telemetry, command, and communication facilities to accommodate spacecraft and experiment control.

For nominally circular orbits (with altitude = 6000 n. mi.) and the assumption of a spherical earth, it is possible to graphically represent the visibility contours of various ground stations on a Mercator map of the world for a given minimum ground antenna elevation angle, for example, $\epsilon = 6$ degrees. This is shown in the geometry of Figure 3-2 and the expressions

$$\rho = (r^2 - R^2 \cos^2 \epsilon)^{1/2} - R \sin \epsilon = 8439.7 \text{ n. mi.}$$

$$\sin \psi = \frac{\rho}{r} \cos \epsilon = \sin 62.743 \text{ degrees}$$

where

ρ = slant range from ground station to spacecraft, n. mi.

r = geocentric radius of circular orbit
= 9441.85 n. mi.

R = earth radius
 ≈ 3441.85 n. mi.

ϵ = minimum elevation angle of ground station antenna
= 6 degrees

ψ = maximum central angle between spacecraft local vertical and ground station geocentric vertical
= 62.743 degrees

The visibility arcs associated with ψ are constructed on a globe of the earth and replotted on the Mercator map of Figure 3-3 for the ground stations locations listed in Table 3-1.

For orbit inclinations $i \leq 33$ degrees, the spacecraft is visible from each of the above ground stations when the subsatellite point is on the concave side of the corresponding contours in Figure 3-3.

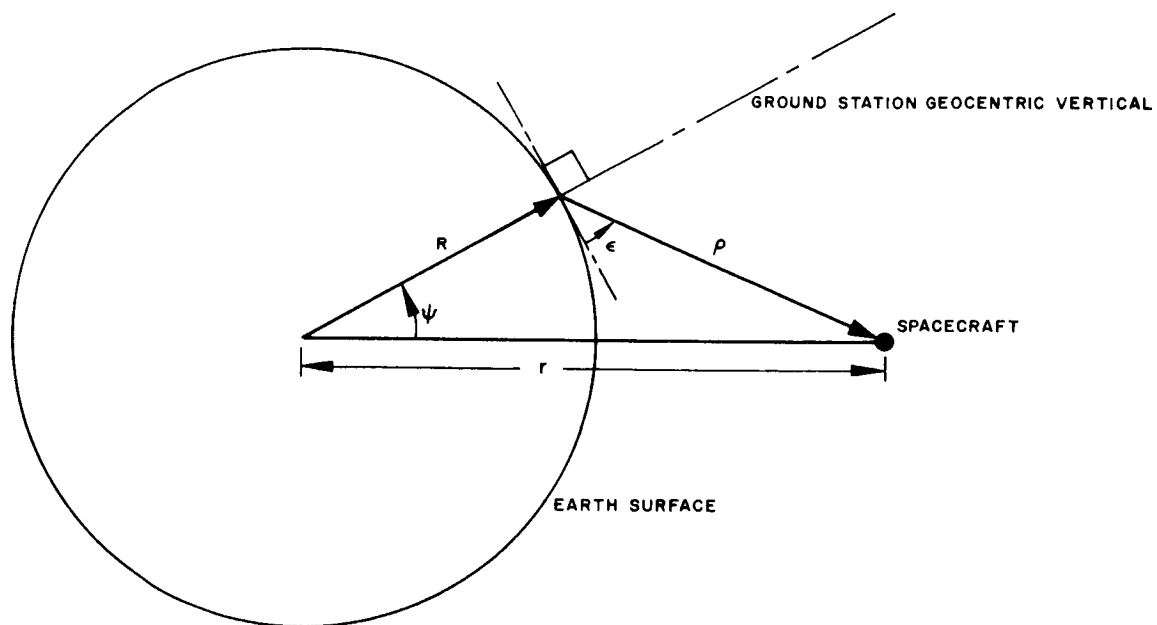


Figure 3-2. Visibility Limit Geometry

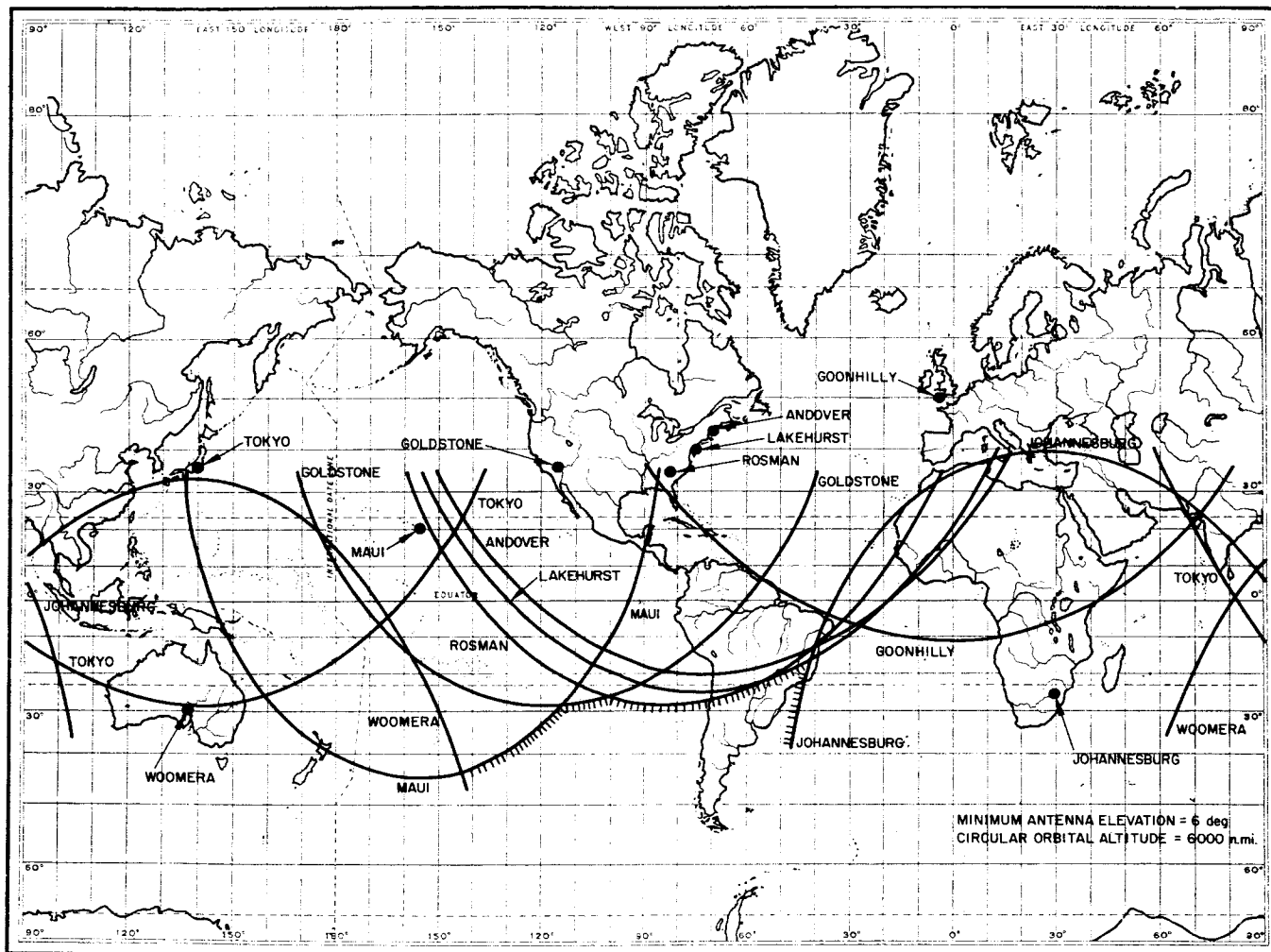


Figure 3-3. Ground Station Visibility Limits

TABLE 3-1. GROUND STATION LOCATIONS

Station Name	Latitude, degrees	Longitude, degrees
Andover, Maine	44.63 N	70.7 W
Lakehurst, New Jersey	39.9 N	74.4 W
Rosman, North Carolina	35.2 N	82.9 W
Goldstone, California	35.39 N	116.85 W
Maui, Hawaii	20.7 N	156.3 W
Tokyo, Japan	35.7 N	139.5 E
Woomera, Australia	31.1 S	136.8 E
Johannesburg, South America	25.9 S	27.7 E
Goonhilly Downs, United Kingdom	50.3 N	5.2 W

The region outlined by the cross-hatched arcs indicates no visibility from any of the stations considered when the subsatellite ground track passes through this area (bounded on the south side by Latitude $\leq 33^\circ$ S). A typical ground track history is presented in Figure 3-4 for a time interval of about 37 hours with an (arbitrary) epoch located at the nodal longitude of 18° E. The relative geometry of the ground track with respect to the ground stations is approximately repeated at the fourth earth circuit (not orbital period)*. The superposition of a ground track history and the contour plots of Figure 3-4 should yield a quantitative estimate of visibility and intervisibility time intervals for different ground station and orbital inclination combinations. For example, Figure 3-5 shows the antenna elevation angle histories of Johannesburg, Goonhilly Downs, Tokyo, and Woomera when tracking a spacecraft in an orbit with an inclination of 33 degrees. Note the waxing and waning of the antenna elevation histories for stations located at similar longitudes but at oppositely sensed latitudes. This is due to the longitudinal shift (with time) of the maximum north-south excursion of the spacecraft induced by the orbital inclination. A similar but less pronounced effect is shown in Figure 3-5b for a 10-degree orbital inclination. Only some of the ground station elevation angle histories were plotted in Figure 3-5 for the sake of clarity.

* The nodal longitude shift eastward per orbit = 360 degrees - (earth rate, deg/hr) (orbital period, hours) = 360 degrees - (15 deg/hr) (6.3945 hours) = 264 degrees.

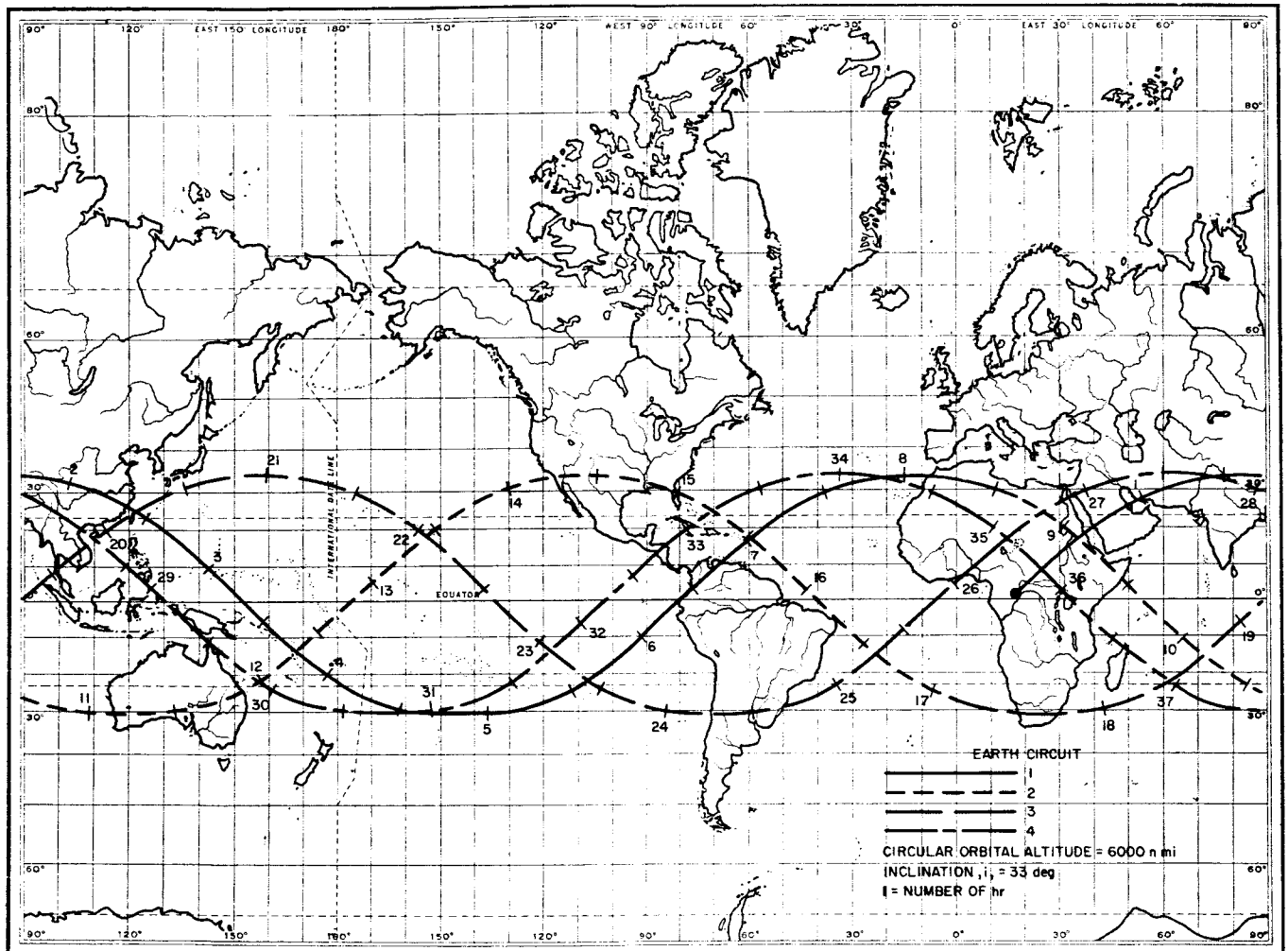


Figure 3-4. Typical Ground Track History

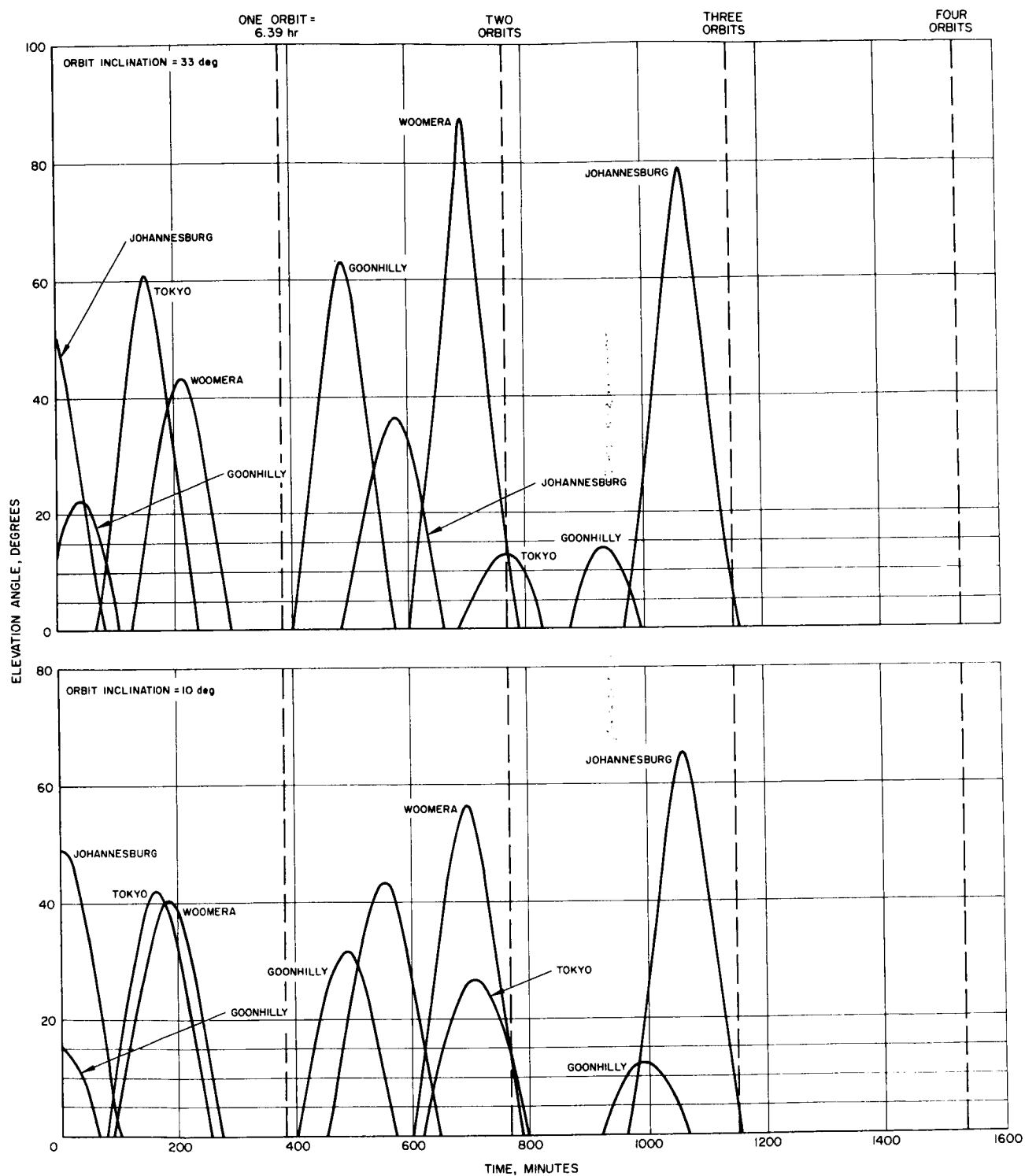


Figure 3-5. Antenna Elevation Angle History

Nodal longitude at $t = 0$ is 342°W
 Circular orbital period = 6.3945 hours

Figure 3-6 shows the antenna elevation angle histories of all nine ground stations listed above for an equatorial orbit. Since the longitude drift rate is linear with time for an equatorial orbit, longitude and time are listed along the abscissa of Figure 3-4, repeating this pattern every 360 degrees of longitude.

Additional antenna elevation angle histories will be presented when a final nodal longitude at injection is determined from powered flight simulations of the recommended medium altitude orbit inclination (about 28 degrees).

INJECTION ERROR ANALYSIS

Spin-Table Spinup Analysis

Spinup of the spacecraft on a spin table attached to the Agena launch vehicle before separation is an alternate method of providing spin.

The objective of this analysis is to calculate the attitude dispersion after separation and the resulting nutation angle caused by tipoff and initial tumbling rate. The attitude dispersion during spinup while attached to the Agena can be conservatively estimated at approximately 0.25 degree. At the time of separation, a possible tumbling rate may exist because of the limit cycle of the Agena attitude control. A conservative assumption of this initial tumbling rate is 0.3 degree per second.

Referring to Figure 3-7, the attitude angle α is defined as the average direction of the spin axis in the inertia frame. For a free spinning body, this average direction of the spin axis coincides with the direction of the angular momentum of the body. Furthermore, the nutation angle ξ is defined as the angle between the spin axis and the angular momentum vector.

The moment equations for a spinning body after the spinup process is completed reduce to (Reference 3-3)

$$\dot{\omega} + i \lambda \omega = \frac{M}{I_x} \quad (3-1)$$

where

ω = complex transverse angular rate

$$= \omega_x + i \omega_y$$

$$i = \sqrt{-1}$$

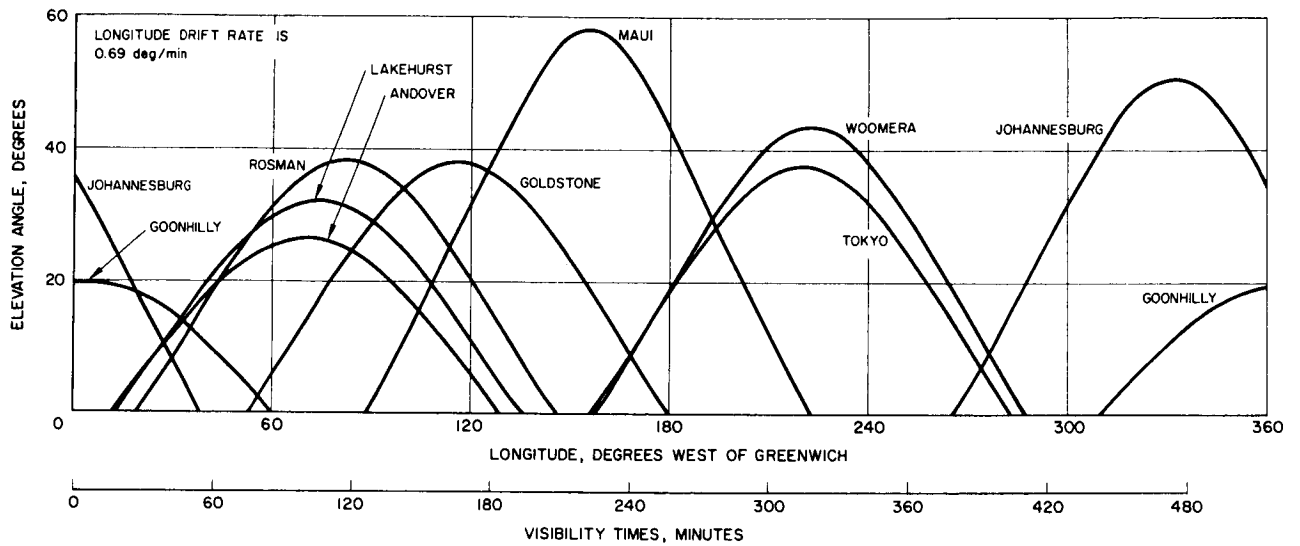


Figure 3-6. Ground Station Antenna Elevation Angles for
Equatorial Medium Altitude
6000 n.mi. orbit

$$\lambda = \omega_z \left(1 - \frac{I_z}{I_x} \right)$$

ω_z = spin rate, (assumed constant)

$I_x = I_y$, I_z = principal moment of inertia of the spacecraft

M = applied transverse moment. In this case, $M = N \delta(t)$ where $\delta(t)$ is the delta function with the unit per second, and $N = N_x + i N_y$ the complex moment impulse with units lb-in-sec.

The solution of Equation 3-1 with $\omega(0) = \omega_o$ is

$$\omega = \left(\omega_o + \frac{N}{I_x} \right) e^{-i\lambda t} \quad (3-2)$$

To find the angle α , it is necessary to relate the moment equation to a fixed reference frame. This is done by means of Euler angles. Defining the instantaneous direction of the spin axis as the angle θ measured with respect to the inertia frame, it can be shown (Reference 3-3) that for small θ and constant ω_z the following relation holds

$$\theta e^{i\psi} = \int_0^t \omega e^{i\omega_z z} dz \quad (3-3)$$

where

θ and ψ are the Euler angles as shown in Figure 3-8. Substituting Equation 3-2 into Equation 3-3 and assuming $\theta(0) = 0$, the integral is immediately evaluated and after rearrangement of terms

$$\theta e^{i\psi} = \left(\frac{I_x \omega_o + N}{I_z \omega_z} \right) \left\{ \sin \left(\frac{I_x}{I_z \omega_z} t \right) + i \left[1 - \cos \left(\frac{I_x}{I_z \omega_z} t \right) \right] \right\} \quad (3-4)$$

The attitude α is by definition

$$\alpha = |\theta|_{\text{ave}}$$

or since $\theta(0) = 0$

$$\alpha = \frac{1}{2} |\theta|_{\text{max}}$$

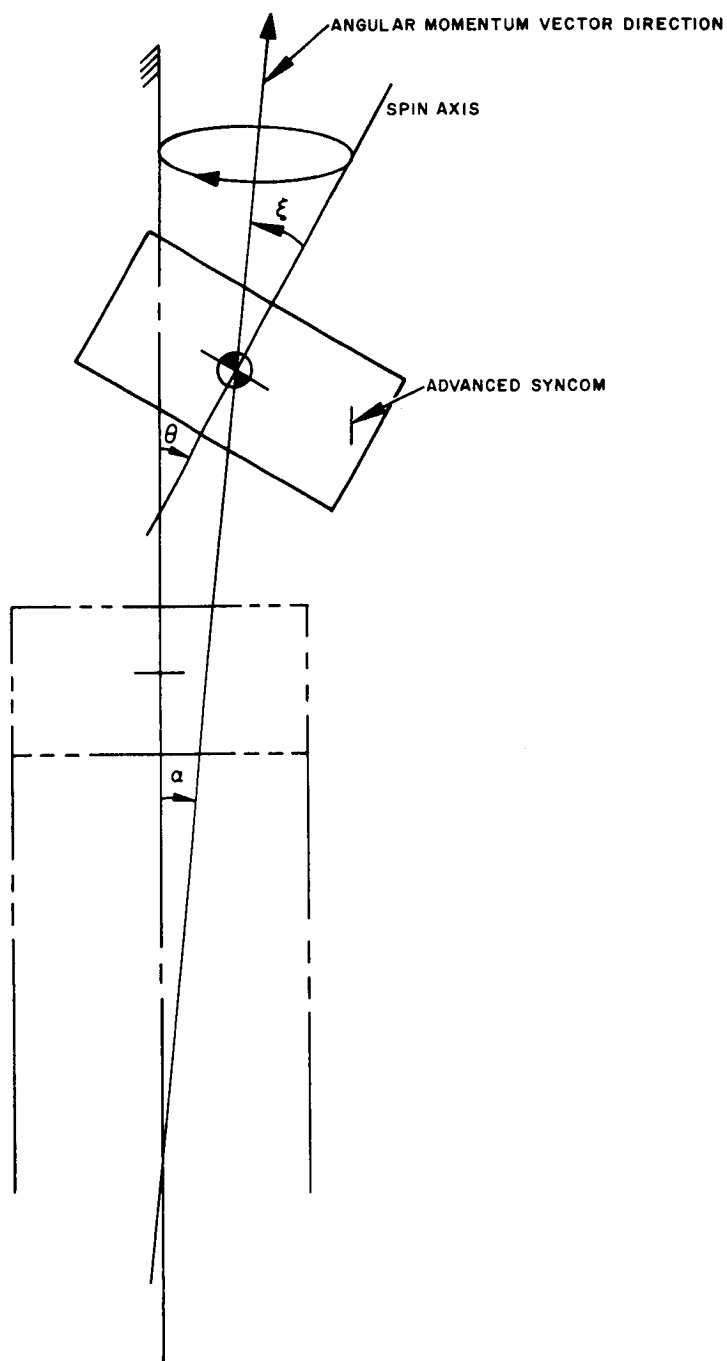


Figure 3-7. Geometry of Separation

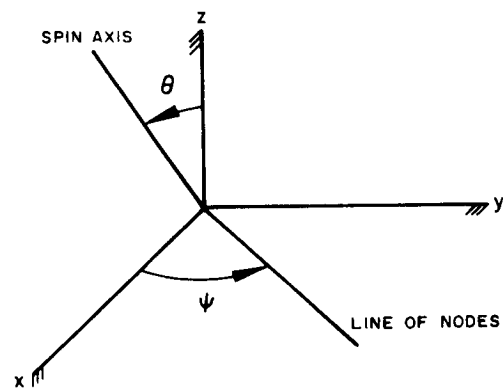


Figure 3-8. Euler Angles

Then from Equation 3-4

$$|\theta| = \left| \frac{I_x \omega_o + N}{I_z \omega_z} \right| \left[2 - 2 \cos \left(\frac{I_x}{I_z \omega_z} t \right) \right]^{\frac{1}{2}} \quad (3-5)$$

and

$$|\theta|_{\max} = 2 \left[\left(\frac{I_x \omega_{ox} + N_x}{I_z \omega_z} \right)^2 + \left(\frac{I_x \omega_{oy} + N_y}{I_z \omega_z} \right)^2 \right]^{\frac{1}{2}} \quad (3-6)$$

hence

$$\alpha = \left[\left(\frac{I_x \omega_{ox} + N_x}{I_x \omega_z} \right)^2 + \left(\frac{I_x \omega_{oy} + N_y}{I_z \omega_z} \right)^2 \right]^{\frac{1}{2}} \quad (3-7)$$

The greatest attitude change caused by a given initial tumbling rate of the launch vehicle $|\omega_o|$ and an initial tipoff impulsive moment $|N|$ can be written in mathematical terms; find the maximum of α with the constraints:

$$|\omega_o| = (\omega_{ox}^2 + \omega_{oy}^2)^{\frac{1}{2}} \quad (3-8)$$

$$|N| = (N_x^2 + N_y^2)^{\frac{1}{2}} \quad (3-9)$$

By the use of Lagrange multipliers, Equation 3-7 is maximized to give:

$$\alpha_{\max} = \frac{I_x |\omega_o| + |N|}{I_z \omega_z} \quad (3-10)$$

The nutation angle is given by definition:

$$\tan \xi = \frac{I_x |\omega|}{I_z \omega_z}$$

For small angles and using Equation 3-2

$$\xi \approx \frac{1}{I_z \omega_z} \left[(I_x \omega_{ox} + N_x)^2 + (I_x \omega_{oy} + N_y)^2 \right]^{\frac{1}{2}} \quad (3-11)$$

Again using the same arguments and procedure as before:

$$\xi_{\max} \simeq \frac{I_x |\omega_o| + |N|}{I_z \omega_z} \quad (3-12)$$

The fact that $\alpha = \xi$ can also be obtained by geometry from Figure 3-7. During the process of spinning up, an attitude deviation α_o may occur because of spinner misalignment, mass unbalance, etc. Since the direction of this angle can be considered random and statistically independent of α_{\max} , the expected attitude deviation caused by spinup process plus separation is:

$$\alpha_{\text{total}} = \left[\alpha_{\max}^2 + \alpha_o^2 \right]^{\frac{1}{2}} \quad (3-13)$$

The application of the above results is straightforward and for the Advanced Syncom yields the following numerical values:

$$|\omega_o| = 0.3 \text{ deg/sec} = 5.23 \times 10^{-3} \text{ rad/sec assumed initial tumbling rate of the Agena}$$

$$\alpha_o = 0.25 \text{ degree}$$

$$\omega_z = 10.4 \text{ rad/sec}$$

$$|N| = 9.6 \text{ in -lb-sec}$$

$$I_x = 916 \text{ in -lb-sec}^2$$

$$I_z = 1062 \text{ in -lb-sec}^2$$

Substituting the above values into Equations 3-10, 3-12, and 3-13

$$\alpha_{\max} = \xi_{\max} = 0.075 \text{ degree}$$

$$\alpha_{\text{total}} = 0.264 \text{ degree}$$

This value is less than would be obtained by free-body spinup and is less than the 1 degree permitted by orbital requirements.

Free-Body Spinup

A computer study has been performed of the attitude dispersion of a spacecraft having rotational dissymmetry due to free body spin. The results of this study are presented in Tables 3-2 and 3-3 and represent the cases that are considered the worst. This study considers perturbations in attitude caused by the Agena tumbling rate plus the separation tipoff rate ($\omega_0 = 0.6$ deg/sec), a transverse disturbing moment M_t due to spinner misalignment, and the attitude dispersion between the time of separation and the start of spinup (0.12 degree) due to ω_0 alone. The nutation damper should make these results conservative. In Table 3-3 the following moments of inertia ratios are assumed

$$I_z : I_y : I_x = 1.10 : 1.00 : 0.95$$

whereas for Table 3-3

$$I_z : I_y : I_x = 1.10 : 1.05 : 1.00$$

Stability of Free Spinning Body with Energy Dissipation

This analysis was made to determine the effects of kinetic energy dissipation on the stability of a free spinning body. Rotational symmetry about the spin axis was assumed to simplify the mathematics. The results may be summarized by considering the body to be a) an oblate (disc-like) spheroid or, b) a prolate (rod-like) spheroid. It is shown in an oblate spheroid that any tumble rate present will tend to decrease with any dissipation of kinetic energy and if there is no tumble rate initially present, none will be induced by dissipation of kinetic energy. In a prolate spheroid it is shown that any dissipation of kinetic energy will result in an increased tumbling rate even if none is present initially. The equations developed permit the prediction of tumble rate if the kinetic energy dissipation is known.

Consider a body spinning in space and in free flight. If no external moments are present, then

$$\dot{\bar{H}} = \bar{M} = 0 \quad (3-14)$$

where

\bar{H} = angular momentum

\bar{M} = external moment acting on the body

TABLE 3-2. RESULTS OF SPINUP STUDIES

$$\frac{I_z}{I_y} = 1.10 ; \frac{I_z}{I_x} = 1.16$$

System		Attitude Error, degree	Nutation Angle		Tumble Rate	
			Minimum, degree	Maximum, degree	Minimum, deg/sec	Maximum, deg/sec
Spin nozzles on center of gravity	$M_t = M_x$ $\omega_o = \omega_x$	0.63	0.30	0.38	3.7	4.5
	$M_t = M_y$ $\omega_o = \omega_x$	0.62	0.19	0.23	2.4	2.8
Spin nozzles 10 inches off center of gravity	$M_t = M_x$ $\omega_o = \omega_x$	1.08	0.67	0.83	8.0	10.9
	$M_t = M_y$ $\omega_o = \omega_x$	0.77	0.51	0.64	6.3	8.6

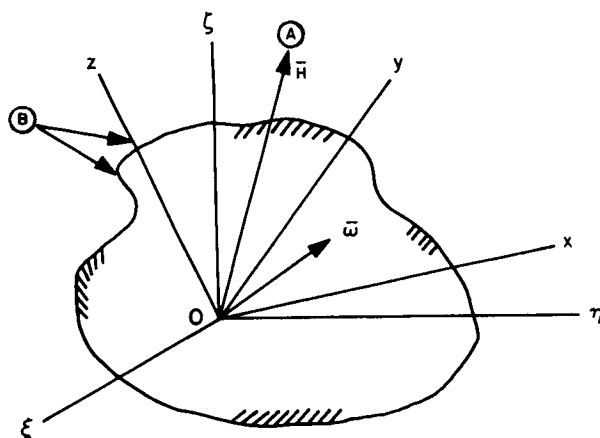
TABLE 3-3. RESULTS OF SPINUP STUDIES

$$\frac{I_z}{I_y} = 1.05 ; \frac{I_z}{I_x} = 1.10$$

System	Attitude Error, degree	Nutation Angle		Tumble Rate	
		Minimum, degree	Maximum, degree	Minimum, deg/sec	Maximum, deg/sec
Spin nozzles on center of gravity	$M_t = M_x$ $\omega_o = \omega_x$	0.35	0.49	4.8	5.5
	$M_t = M_y$ $\omega_o = \omega_x$	0.20	0.28	2.4	3.2
Spin nozzles 10 inches off center of gravity	$M_t = M_x$ $\omega_o = \omega_x$	0.77	1.08	9.2	12.5
	$M_t = M_y$ $\omega_o = \omega_x$	0.52	0.70	6.3	8.7

Since Oxyz are principal axes

$$\bar{H} = A\omega_x \bar{i} + B\omega_y \bar{j} + C\omega_z \bar{k} \quad (3-15)$$



Oxyz principal axes
of inertia of B

(A) Galilean frame

(B) Body

The kinetic energy T of B is given by

$$2T = \bar{H} \cdot \bar{\omega} = A\omega_x^2 + B\omega_y^2 + C\omega_z^2 \quad (3-16)$$

if B is a body of revolution such the

$$A = B \neq C \quad (3-17)$$

then

$$2T = A(\omega_x^2 + \omega_y^2) + C\omega_z^2 \quad (3-18)$$

and

$$\begin{aligned} \bar{H} &= A(\omega_x \bar{i} + \omega_y \bar{j}) + C\omega_z \bar{k} \\ \bar{H}^2 &= A^2(\omega_x^2 + \omega_y^2) + C^2\omega_z^2 \end{aligned} \quad (3-20)$$

Let

$$\omega_x^2 + \omega_y^2 = \omega_r^2 \quad (3-21)$$

and designate initial angular rates with o subscript

$$2T = A\omega_r^2 + C\omega_z^2 \quad (3-22)$$

$$\bar{H}_o^2 - \bar{H}^2 = A^2(\omega_{ro}^2 - \omega_r^2) + C^2(\omega_{zo}^2 - \omega_z^2) = 0 \quad (3-23)$$

$$\left. \begin{aligned} A\omega_r^2 + C\omega_z^2 &= 2T \\ A^2\omega_r^2 + C^2\omega_z^2 &= A^2\omega_{ro}^2 + C^2\omega_{zo}^2 \end{aligned} \right\} (3-24)$$

$$\left. \begin{aligned} \omega_r^2 + \frac{C}{A}\omega_z^2 &= \frac{2T}{A} \\ \omega_r^2 + \frac{C^2}{A^2}\omega_z^2 &= \left[\omega_{ro}^2 + \frac{C^2}{A^2}\omega_{zo}^2 \right] \end{aligned} \right\} (3-25)$$

Solving for ω_r and ω_z

$$\left. \begin{aligned} \omega_r &= \left[\frac{2TC - A^2\omega_{ro}^2 - C^2\omega_{zo}^2}{A(C - A)} \right]^{1/2} \\ \omega_z &= \left[\frac{\omega_{ro}^2 + \left(\frac{C}{A}\right)^2\omega_{zo}^2 - \frac{2T}{A}}{\frac{C}{A} \left(\frac{C}{A} - 1\right)} \right]^{1/2} \end{aligned} \right\} (3-26)$$

and

$$T = T_o - \Delta T = \frac{1}{2}A\omega_{ro}^2 + \frac{1}{2}C\omega_{zo}^2 - \Delta T$$

Equation 3-26 should now be considered for two cases.

Case A. B is an oblate spheroid (disc-like) $A < C$

$$1) \quad \omega_{ro} = 0 \quad \therefore T_o = \frac{1}{2} C \omega_{zo}^2$$

(-) or 0

$$\omega_r = \left[\frac{\overbrace{2TC - C^2 \omega_{zo}^2}^{(-)}}{\underbrace{A(C - A)}_{(+)}} \right]^{1/2} = 0$$

With dissipation of kinetic energy, T gets smaller and ω_r becomes imaginary, indicating that no tumble rate can be expected.

$$2) \quad \omega_{ro} > 0 \quad \therefore T_o = \frac{1}{2} A \omega_{ro}^2 + \frac{1}{2} C \omega_{zo}^2$$

ω_r goes to zero when

$$2TC \leq A^2 \omega_{ro}^2 + C^2 \omega_{zo}^2$$

$$2T \leq \frac{A^2}{C} \omega_{ro}^2 + C \omega_{zo}^2$$

$$A \omega_{ro}^2 + C \omega_{zo}^2 - 2\Delta T \leq \frac{A^2}{C} \omega_{ro}^2 + C \omega_{zo}^2$$

or

$$\Delta T \geq \frac{1}{2} \left(1 - \frac{A}{C}\right) A \omega_{ro}^2$$

Dissipation of a small amount of kinetic energy even when $A \approx C$ but $A < C$ will result in quick stabilization of rotation about the Z axis.

Case B. B is a prolate spheroid (rod-like). $A > C$

$$1) \quad \omega_{ro} = 0 \quad \therefore \quad T_o = \frac{1}{2} C \omega_{zo}^2$$

(-) or 0

$$\omega_r = \left[\frac{2TC - C^2 \omega_{zo}^2}{A(C - A)} \right]^{1/2}$$

(-)

Any dissipation of kinetic energy will result in a tumble rate

$$\omega_r = \left[\frac{2\Delta T}{A(A - C)} \right]^{1/2}$$

and a reduced spin rate ω_z , which can be easily computed by Equation 3-26.

$$2) \quad \omega_{ro} > 0 \quad \therefore \quad T_o = \frac{1}{2} A \omega_{ro}^2 + \frac{1}{2} C \omega_{zo}^2$$

(+)

$$\omega_r = \left[\frac{A(A - C) \omega_{ro}^2 + 2C\Delta T}{A(A - C)} \right]^{1/2}$$

(+)

Any dissipation of kinetic energy will result in an increased tumble rate.

MICRO-THRUSTING INTERVALS FOR SMALL ECCENTRICITY CHANGES OF NEAR CIRCULAR ORBITS

Summary

Beginning with the Lagrange planetary equation for the variation of eccentricity with time (de/dt) due to the in-plane perturbing influence of a small constant radial (R) or circumferential (S) acceleration (normal to R), the additional assumption of a small maximum eccentricity ($e_{\max} \leq 0.02$)

after N intervals of unidirectional thrusting (with each thrusting interval less than an orbital period) yield the following approximate expressions for required equivalent* velocity increment ΔV_c to effect an eccentricity change, Δe (Figure 3-9).

$$\Delta V_c = N \cdot \frac{\delta V_e}{\text{orbit}} \approx \frac{(\Delta e) V_o (f_2 - f_1)}{2(\sin f_2 - \sin f_1)} \quad ; \quad \begin{matrix} R = 0 \\ S = \text{constant} \end{matrix} \quad (3-27)$$

$$\Delta V_c = N \cdot \frac{\delta V_e}{\text{orbit}} \approx \frac{(\Delta e) V_o (f_2 - f_1)}{(\cos f_1 - \cos f_2)} \quad ; \quad \begin{matrix} S = 0 \\ R = \text{constant} \end{matrix} \quad (3-28)$$

where V_o is the circular orbital velocity associated with the product of the mean motion and semimajor axis, (na) . Also f_1 and f_2 are the values of the true anomaly at which the thrusting begins and ends respectively for each orbit, (assumed constant for all N orbits and $|f_2 - f_1| < 2\pi$).

Since the impulsive velocity increment ΔV_i required to effect a change Δe is approximated by

$$\Delta V_i \approx \frac{(\Delta e)}{2} V_o \quad (3-29)$$

a measure of eccentricity correction efficiency of the impulsive mode may be obtained relative to the continuous thrusting mode by forming the ratio (assuming equal specific impulse for both modes).

$$\frac{\Delta V_i}{\Delta V_c} \approx \frac{\sin f_2 - \sin f_1}{f_2 - f_1} \quad ; \quad R = 0 \quad (3-30)$$

$$\frac{\Delta V_i}{\Delta V_c} \approx \frac{\cos f_1 - \cos f_2}{2(f_2 - f_1)} \quad ; \quad S = 0 \quad (3-31)$$

In Equation 3-27, minimum time to generate Δe corresponds approximately to the most efficient condition, $f_2 = -f_1 = \pi/2$, so that Equation 3-30 becomes

$$\left(\frac{\Delta V_i}{\Delta V_c} \right)_{\text{min time}} \approx \frac{2}{\pi} = 0.6366 \quad ; \quad R = 0 \quad (3-32)$$

* As compared with an impulsive velocity increment.

In Equation 3-28, the minimum time case occurs when $f_1 = 0$ and $f_2 = \pi$, so that Equation 3-31 becomes

$$\left(\frac{\Delta V_i}{\Delta V_c} \right)_{\min \text{ time}} \approx \frac{1}{\pi} = 0.3183 \quad ; \quad S = 0 \quad (3-33)$$

A comparison of Equations 3-32 and 3-33 shows that circumferential (~tangential) thrusting is the preferred continuous mode to change eccentricity (at least from an efficiency viewpoint) for a given constant thrust.

If both the constant radial (R) and circumferential (S) accelerations are turned on at true anomaly f_1 and off at f_2 , the eccentricity change per orbit is approximated for small eccentricities ($e \leq 0.02$) by

$$\frac{\delta e}{\text{orbit}} \approx \frac{a^2}{\mu} \left[(\cos f_1 - \cos f_2) \cdot R + 2 (\sin f_2 - \sin f_1) \cdot S \right] ; \quad (3-34)$$

$$|f_2 - f_1| < 2\pi$$

where

$$\begin{aligned} a^2 &= \text{square of semi-major axis} \\ \mu &= \text{constant of attraction} = n^2 a^3 \\ &= 62\,627.75 \text{ (n.mi.)}^3 / \text{sec}^2 \end{aligned}$$

Now for a 6000 n.mi. altitude circular orbit

$$\frac{a^2}{\mu} \approx 0.2341 \frac{\text{sec}^2}{\text{ft}} \quad (3-35)$$

whereas for a circular synchronous orbit

$$\frac{a^2}{\mu} \approx 1.360 \left(\frac{\text{sec}^2}{\text{ft}} \right) \quad (3-36)$$

If satellite libration damping considerations permit two intervals of equal and opposite thrust per orbit spaced symmetrically about $f = 0, \pi$ for the circumferential (tangential) mode (Figure 3-10) and spaced symmetrically about $f = -\pi/2, \pi/2$ for the radial mode, the time required to accrue or remove a given value of Δe is reduced to half that required for the single, unidirectional thrust interval per orbit case. The relative efficiency measure of Equations 3-30 and 3-31 will remain the same.

Finally, if in Equation 3-30, $f_2 = -f_1 = f \leq \pi/2$ the expression reduces to the tabulated function

$$\frac{\Delta V_i}{\Delta V_c} \approx \frac{\sin f}{f} \quad ; \quad f \leq \frac{\pi}{2} \quad (3-37)$$

Analysis

Consider a spacecraft in a closed orbit with osculating elements $a, e, i, \Omega, \omega, \sigma$ under the influence of three orthogonal acceleration components R, S, W with R, S in the orbit plane as in Figure 3-11, the Lagrange planetary equations for the time variation of the above elements may be expressed as, (e.g., Moulton, Reference 3-4, or Deutsch, Reference 3-5).

$$\begin{aligned} \frac{da}{dt} &= \frac{2}{n \sqrt{1-e^2}} \left(e \sin f \cdot R + \frac{p}{r} S \right) ; \\ \frac{dn}{dt} &= \frac{-3}{a \sqrt{1-e^2}} \left[e \sin f \cdot R \right. \\ &\quad \left. + (1 + e \cos f) S \right] \end{aligned} \quad (3-38)$$

$$\frac{de}{dt} = \frac{\sqrt{1-e^2}}{na} \left[\sin f \cdot R + (\cos f + \cos E) S \right] \quad (3-39)$$

$$\frac{di}{dt} = \frac{r \cos(\omega + f)}{na^2 \sqrt{1-e^2}} W \quad (3-40)$$

$$\frac{d\Omega}{dt} = \frac{r \sin(\omega + f)}{na^2 \sqrt{1-e^2} \sin i} W \quad (3-41)$$

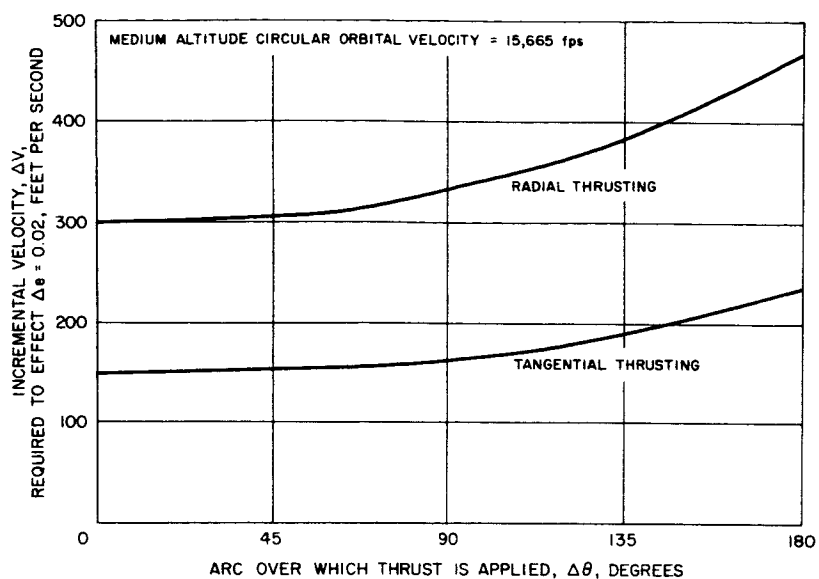


Figure 3-9. Velocity Increment for Eccentricity Changes of 0.02

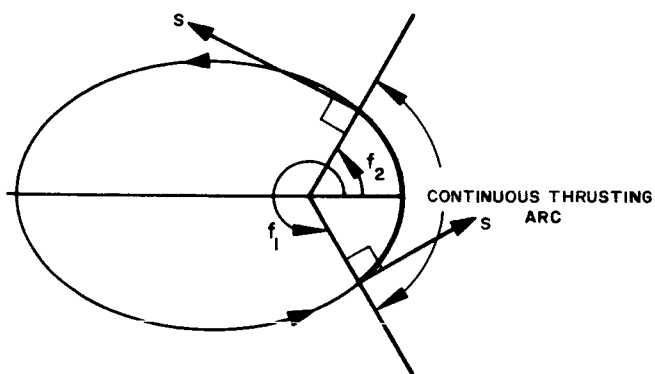


Figure 3-10. Typical Thrusting Arc

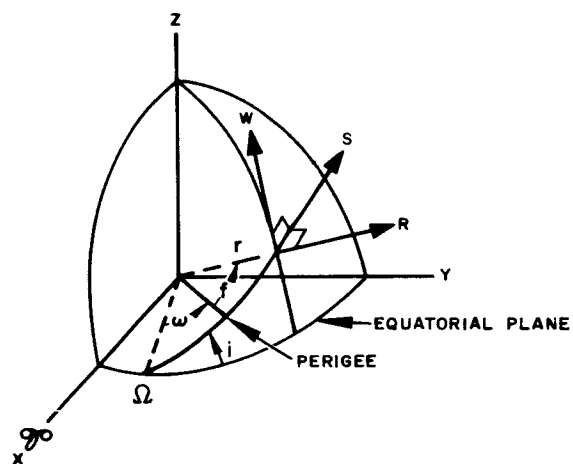


Figure 3-11. Orbital and Thrusting Geometry

$$\begin{aligned} \frac{d\omega}{dt} = & \frac{\sqrt{1-e^2}}{nae} \left[-\cos f \cdot R + \left(1 + \frac{r}{p}\right) \sin f \cdot S \right] \\ & - \frac{r \sin(\omega + f) \cot i}{na^2 \sqrt{1-e^2}} \cdot W \end{aligned} \quad (3-42)$$

$$\frac{d\sigma}{dt} = \frac{(1-e^2)}{nae} \left[\left(\cos f - \frac{2re}{p} \right) R - \left(1 + \frac{r}{p}\right) \sin f \cdot S \right] \quad (3-43)$$

where

r = geocentric radius to spacecraft

$$= \frac{a(1-e^2)}{1+e \cos f} = \frac{p}{1+e \cos f} = a(1-e \cos E)$$

a = semi-major axis of orbit

i = inclination

Ω = right ascension of ascending node

ω = argument of perigee

$$\sigma = -nT_o = -\frac{2\pi}{\tau} T_o$$

n = mean motion

τ = orbital period

T_o = time of perigee passage

E = eccentric anomaly

Small Eccentricity Change

Only Equation 3-39 will be considered although a similar approach may be used for other elements using the small eccentricity approximation.

To integrate Equation 3-39 the following relations will be used:

$$\frac{de}{df} = \frac{de}{dt} \frac{dt}{df} = \frac{de}{dt} \frac{r^2}{a^2 n \sqrt{1-e^2}}$$

The last expression in Equation 3-34 is based on the assumption of conservation of angular momentum per orbit for low thrust levels. Substituting Equation 3-34 into Equation 3-39 gives

$$\frac{de}{df} = \frac{r^2}{\mu} \left[\sin f \cdot R + (\cos f + \cos E)S \right] \quad (3-45)$$

Now, if terms of $O(e^2)$ are ignored, the result is

$$r = a(1 - e \cos E) = \frac{a(1 - e^2)}{1 + e \cos f} \approx a(1 - e \cos f) \quad (3-46)$$

so that $E \approx f$ and

$$r^2 \approx a^2 (1 - 2e \cos f) \quad (3-47)$$

With the approximations of Equations 3-46 and 3-47, Equation 3-45 becomes

$$\frac{de}{df} \approx \frac{a^2}{\mu} (1 - 2e \cos f) (\sin f \cdot R + 2 \cos f \cdot S) \quad (3-48)$$

For $R = 0$, the eccentricity change per orbit is ($e \approx$ constant for each orbit)

$$\left. \frac{\delta e}{\text{orbit}} \right|_{R=0} \approx \frac{a^2}{\mu} \left\{ 2S (\sin f_2 - \sin f_1) - eS (2f_2 - 2f_1 + \sin 2f_2 - \sin 2f_1) \right\} \quad (3-49)$$

where f_1, f_2 are the true anomaly values of thrust on and thrust off times respectively. When $f_2 = -f_1 = \pi/2$ Equation 3-49 becomes (for $e \leq 0.02$) the condition for minimum time to change e ,

$$\left. \frac{(\delta e)_{\max}}{\text{orbit}} \right| = \frac{a^2}{\mu} S (4 - 2\pi e) \geq \frac{4a^2}{\mu} \cdot S (1 - 0.0314)$$

so that the approximation to Equation 3-49 with

$$\frac{\delta e}{\text{orbit}} \approx \frac{2a^2}{\mu} S (\sin f_2 - \sin f_1) \quad (3-50)$$

is valid to about $(\frac{\pi}{2} e \cdot 100) \approx 3$ percent.

Similarly if $S = 0$, the integral of Equation 3-48 gives for $|f_2 - f_1| < 2\pi$

$$\left. \frac{\delta e}{\text{orbit}} \right|_{S=0} \approx \frac{a^2}{\mu} R \left[\cos f_1 - \cos f_2 - \frac{e}{2} (\cos 2f_1 - \cos 2f_2) \right] \quad (3-51)$$

$$\approx \frac{a^2}{\mu} R \left[(\cos f_1 - \cos f_2) \pm e \right] \quad (3-52)$$

If it takes N orbits to accrue a net eccentricity change $\Delta e \leq 0.02$ with either one radial (R) or one tangential (S) acceleration interval per orbit, each beginning at f_1 and ending at f_2 ($|f_2 - f_1| < 2\pi$), referenced to the perigee of the osculating orbit, then

$$\left. \Delta e \right|_{R=0} \approx \frac{2Na^2S}{\mu} (\sin f_1 - \sin f_1) \quad (3-53)$$

$$\left. \Delta e \right|_{S=0} \approx \frac{Na^2R}{\mu} (\cos f_1 - \cos f_2) \quad (3-54)$$

For the most efficient tangential acceleration case, the equivalent velocity increment required to generate Δe in Equation 3-53 is approximated by

$$\begin{aligned} \Delta V_c &= N \cdot \frac{\delta V_c}{\text{orbit}} \approx \frac{NS(f_2 - f_1)}{2\pi} \tau = \frac{NS}{n} (f_2 - f_1) \quad (3-55) \\ &= \frac{(\Delta e)}{2} na \left(\frac{f_2 - f_1}{\sin f_2 - \sin f_1} \right) \end{aligned}$$

The impulsive velocity increment ΔV_i needed to generate Δe is estimated as

$$\Delta V_i \approx \frac{\Delta e}{2} V_o = \frac{\Delta e}{2} na \quad (3-56)$$

so that a measure of the efficiency of ΔV_c for continuous thrust versus that of impulsive thrusting is given by

$$\frac{\Delta V_i}{\Delta V_c} \approx \frac{\sin f_2 - \sin f_1}{f_2 - f_1} \quad ; \quad R=0 \quad (3-57)$$

similarly for $S=0$,

$$\frac{\Delta V_i}{\Delta V_c} \approx \frac{\cos f_1 - \cos f_2}{2(f_2 - f_1)} \quad ; \quad S=0 \quad (3-58)$$

REFERENCES

- 3-1. "Launch and Orbital Analysis," Hughes Aircraft Company SSD 31078R, October 1963.
- 3-2. P. E. Norsell, "Payload Information from LMSC," Hughes Aircraft Company IDC 22-80-AS/76, 16 December 1963.
- 3-3. D. D. Williams, "Dynamic Analysis and Design of the Synchronous Communication Satellite," Hughes Aircraft Company TM 649, May 1960.
- 3-4. F. R. Moulton, An Introduction to Celestial Mechanics, Macmillan (1914), pp 404-405.
- 3-5. R. Deutsch, Orbital Dynamics of Space Vehicles, Prentice Hall (1963) pp 172-173, (Note: In Eq. 7-90 $\cos u$ should read $\cos E$).

4. GRAVITY-GRADIENT STABILIZATION SYSTEM

The following discussion presents a summary of the analyses, computations, and other engineering considerations associated with the feasibility assessment and performance evaluation of the gravity-gradient stabilized vehicles referred to as MAGGE and SAGGE. In general, the investigations are applicable to both vehicles. Considerations applicable to a particular vehicle are specifically delineated in the text.

The gravity-gradient stabilization system studies have merged into two major categories. First, there is the evaluation of the various factors affecting the attitude performance of the vehicle under the operational conditions imposed by the mission. Second, there is the engineering task of integrating a Government-furnished equipment, gravity-gradient stabilization system into a particular vehicle(s). Except for an introductory discussion of factors affecting the spacecraft configuration, this discussion deals primarily with the first category.

SUMMARY

Factors Affecting Choice of Vehicle Configuration

There are numerous configurations which can adequately satisfy the general requirements of passive gravity-gradient stabilization. From the stabilization standpoint, only three basic conditions need be met. First, depending upon the method of damping, various moment-of-inertia ratios must satisfy the stability criteria as established by the equations of motion. Second, the spring constant of the damper body coupling spring must be greater than some prescribed value. Third, the absolute values of the moments of inertia must be large enough to ensure sufficiently small attitude errors. A particular implementation of the above requirements and the constraints imposed by certain mission requirements greatly restrict the range and scope of feasible vehicle configurations. The basic feasibility of the configuration under consideration is established below in the light of mission requirements, and specific constraints and limitations are discussed.

The basic configuration under investigation differs only in certain design details from the one originally proposed by GSFC. The primary considerations leading to such a configuration and the attendant constraints and limitations for specific missions are summarized below.

Synchronous Orbit Launch

The attainment of a synchronous orbit with zero inclination requires the use of an apogee engine which dictates spin stabilization. Initial orbital adjustment for the purpose of removing eccentricity, adjusting inclination, and acquiring the desired longitude also calls for spin stabilization as demonstrated by Syncom 2. Thus, the "hat-box" configuration having maximum moment of inertia about the spin axis is a natural vehicle for the mission. However, the integration of boom deployment mechanisms around an apogee engine is accompanied by certain mechanical constraints including maintaining suitable moment of inertia ratios, ensuring minimum deletion of solar cell area where the booms emerge from the vehicle, and maintaining appropriate boom orientation relative to the vehicle-fixed axes. In the presence of the apogee engine, mechanical synchronization of boom deployment becomes particularly unattractive as does the capability for varying the x-angle between booms. Thus, active consideration is being given to the use of a fixed boom angle and an electrical synchronization system which stops all booms if one boom fails to deploy. The presence of the apogee engine causes a difference between SAGGE and MAGGE gravity-gradient system integration problems, the details of which are presented in subsequent discussions.

Operational Attitude of Vehicle Relative to Orbital Plane

As a result of gravity-gradient stabilization, the satellite makes one revolution per orbital period about an axis normal to the orbital plane. This axis of rotation should be the longitudinal or spin axis of the spacecraft, an axis which coincides with the thrust axis of the apogee engine. The principal reason for such an orientation is the optimization of solar cell power output. A second consideration is that of convenience in positioning control jets for thrusting parallel and normal to the orbital plane. Thus, the gravity-gradient stabilization and damping modes must be positioned relative to the vehicle-fixed axes with a prescribed geometry. Details of this geometry are presented in a subsequent section.

Single Axis Damper

The use of a single axis damper inertially coupled to all modes of vehicle attitude motion places a constraint on the location of the damper axis relative to the axis of maximum moment of inertia of the vehicle. This geometry has been optimized through computer studies carried out by the NASA at Ames Research Center and at Goddard Space Flight Center. The

orientation of the damper axis relative to the plane of the stabilizing booms and the orientation of the plane of the stabilizing booms relative to satellite-fixed axes are defined in a subsequent discussion.

Moment of Inertia Ratios and Magnitudes

The ratios and magnitudes of the satellite moments of inertia have been established by extensive computer studies. Implementation of the desired ratios is achieved by extensible boom relative geometry, that is, by specifying boom angles relative to the vehicle yaw axis. Inertia magnitudes are established by tip masses and boom lengths.

In general, boom length should be as short as possible consistent with feasible design of the damper coupling spring. Neglecting the central body inertia and central body solar radiation torque momentarily, in theory the gravity gradient stabilization system performance is not seriously affected by boom length. The reasoning supporting this statement is summarized as follows:

- 1) Excitation resulting from eccentricity is directly proportional to vehicle inertia as is the restoring moment.
- 2) Maximum solar radiation torque on the booms is proportional to the cube of the boom length.
- 3) Center-of-gravity displacement is proportional to the square of the boom length; thus ratio of reaction jet disturbance to restoring moment remains constant as boom length is varied.
- 4) Perturbations of vehicle inertias and inertia ratios is proportional to boom length squared.

Factors tending to veto an increase in boom length are:

- 1) Reduction of normal mode frequencies
- 2) Aggravation of inversion problem
- 3) Reduction in reliability of complete deployment
- 4) Increased bending while operating reaction control system

Based on the presently acceptable attitude performance shown in the Goddard Space Flight Center computer studies, and considering the fact that natural profile effects will increase attitude errors, it is recommended that the booms not be shortened. Specifically, there is no firm requirement for making any change in the nominal boom length (100 feet) or in the tip masses discussed later in this section. Additional quantitative details of the above considerations are in process.

The question of what is the optimum nominal boom length may be answered in the flight program with the capability of reducing boom length on command. Then the booms could be retracted during some part of the mission and the considerations listed above could be experimentally evaluated. However, it would appear advisable to establish boom length variation at the end of the mission (or late in the mission) to prevent some retraction malfunction from degrading the major portion of the experimental results.

Absence of Local Vertical Obscuration in Cone of Approximately 30 Degrees Total Angle

The desirability of leaving the local vertical free of any structural members essentially dictates the utilization of an X-configuration for the stabilizing booms to achieve, in a reasonably practical manner, the required moment of inertia ratios.

Gravity-Gradient Stabilization in Synchronous Orbit

A prerequisite to satisfying the above condition is projected area symmetry about the vehicle center of gravity. Thus, vehicle configurations like the TRAAC satellite (Reference 4-1) and the Bell System Technical Journal satellite design (Reference 4-2) would be unsatisfactory for synchronous altitude operation because of the relatively large displacement between center of pressure and center of mass. The X-configuration is optimum from the standpoint of maintaining projected area symmetry about the center of gravity.

The above considerations indicate a vehicle configuration which is essentially a modified Advanced Syncom spacecraft having X-shaped stabilization booms of almost 100 feet and tip masses as indicated in the succeeding section.

Moment-of-Inertia Configuration Summary

The angle between the plane containing the mass centroids of the four X-booms and the plane of the damper boom is $\beta = \gamma + \delta = 62.6$ degrees. This angle has been established by GSFC computer studies. (See Figure 4-1.)

Define

I_2 = maximum moment of inertia of X-booms (excluding central body)

I_1 = intermediate moment of inertia of X-booms

I_D = moment of inertia of damper boom

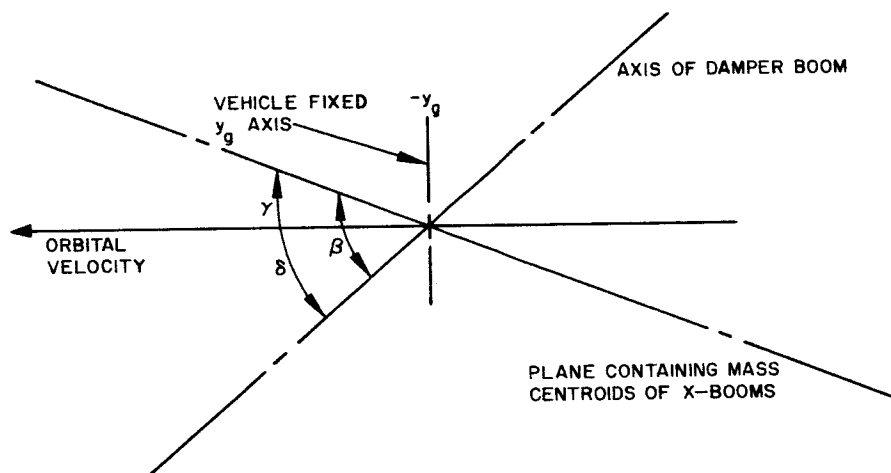


Figure 4-1. Boom Geometry

Then

$$I_D/I_1 = 0.08 \text{ (from GSFC computer studies)}$$

$$I_2/I_1 = 1.12 \text{ (from GSFC computer studies)}$$

The nominal half-angle of the X is fixed by

$$\frac{I_2}{I_1} = 1.12 = \frac{1}{\cos^2 \mu} \quad \mu = 19.1 \text{ degrees}$$

SAGGE Configuration:

Let X-boom tip mass = 10 pounds

σ = boom mass per foot

= 7.83×10^{-4} slugs per foot for 0.003-inch, 1/2-inch diameter beryllium copper with 180-degree overlap.

Then

$$I_2 = 4\left(\frac{10}{32.2}\right) \times 100^2 + \frac{4}{3} \times 7.83 \times 10^{-4} \times 100^3$$

$$= 12420 + 1040 = 13460 \text{ slug-ft}^2$$

$$I_1 = I_2 \cos^2 19.1 \text{ degrees} = 12020 \text{ slug-ft}^2$$

$$I_D = 0.08 (12020) = 960 \text{ slug-ft}^2$$

Damper tip mass:

$$960 = 2m_d(45)^2 + \frac{1}{12} \times 7.83 \times 10^{-4} \times 90^3$$

$$= 47.5 + 4050 m_d$$

$$m_d = \frac{960 - 47.5}{4050} = 0.225 \text{ slugs} = 7.25 \text{ pounds}$$

The angles γ and δ are obtained from

$$I_D \sin 2\delta = (I_2 - I_1) \sin 2\gamma$$

$$\gamma + \delta = 62.6 \text{ degrees}$$

giving

$$\tan 2\delta = \frac{\frac{I_2 - I_1}{I_D} \sin 2(62.6 \text{ degrees})}{1 + \frac{I_2 - I_1}{I_D} \cos 2(62.6 \text{ degrees})}$$

$$\frac{I_2 - I_1}{I_D} = \frac{13460 - 12020}{960} = 1.5$$

$$\sin 2(62.6) = 0.8175$$

$$\cos 2(62.6) = -0.577$$

$$\tan 2\delta = \frac{1.5(0.8175)}{1 - 1.5(0.577)} = 9.1$$

$$2\delta = 83.8$$

$$\delta = 41.9$$

$$\gamma = 20.7$$

MAGGE configuration:

Let X-boom tip mass = 2.5 pounds

Then

$$I_2 = 1040 + 4 \left(\frac{2.5}{32.2} \right) 100^2 = 4152$$

$$I_1 = 4152 \cos^2 19.1 = 3709 \text{ slug-ft}^2$$

$$I_D = 0.08 (3709) = 296 \text{ slug-ft}^2$$

$$m_d = \frac{296 - 47.5}{2 \times 45^2} = \frac{248.5}{4050} = 0.0613 \text{ slugs}$$

$$= 1.97 \text{ pounds}$$

Details of moment of inertia computations are contained in the section on mass properties data.

Shift in Center of Mass Due to Thermal Bending of Booms

The perturbation in center-of-mass location resulting from thermal bending of the booms has been evaluated. The shape of the center of gravity shift in the $X_g - Y_g$ plane does not vary significantly over the range of orbits considered in Table 4-1, the cases 1 and 4 being typical except for the Y_g component of center of gravity shift which does vary with orbital geometry between the limits of about ± 1.4 inches. Figure 4-2 shows the results for cases 1 and 4 respectively. The maximum center of gravity shift component is in the X-direction, being about 2 inches. A boom absorbtivity of 0.2 was used as the basis for determining thermal bending, resulting in a maximum deflection of about 2.8 feet for the tip masses. Figure 4-3 defines the center of gravity shift nomenclature, and Figure 4-4 illustrates the vehicle-sun-orbit geometry.

It is emphasized here that the center of gravity location perturbation because of thermal bending must be added to a statistically determined center of gravity shift bias arising from the natural profile of the booms. The above shift results from thermal bending only.

Natural Profile of Gravity-Gradient Stabilization Booms

A long, tubular element of the type being considered here has a natural, 3-dimensional profile resulting from residual stresses in the boom material which occur during manufacture, storage on the drum, and pay-out through the guide arrangement. This natural profile could be measured if it were possible to observe a suitably long section of the tube in a force-free condition. Such observation does not appear feasible, but certain approximations may be made by suspending the boom at intervals with a system of carefully designed floats which rest on quiet water in a still atmosphere.

Experimental determination of the natural profile of a 100-foot boom was undertaken at DeHavilland (Reference 4-3), but the results were not conclusive. The boom did exhibit various profiles as reported in Reference 4-3, but certain instrumentation difficulties existed which precluded final conclusions being attained. However, according to DeHavilland, the natural profile in bending is repeatable for a given boom, although the twist may exhibit some variation when cycling a given boom. The question to be resolved is: for a fixed deployment mechanism, what is the location of the tip mass at the conclusion of payout? Figure 4-5 illustrates the problem

TABLE 4-1. ORBITAL CONDITIONS FOR CENTER OF GRAVITY
SHIFT CURVES

Case	ψ	α	Ω	R		
1	0	0	0	22766		
2	30	0	0	22766		
3	60	0	0	22766		
4	90	0	0	22766		
5	120	0	0	22766		
6	150	0	0	22766		
7	180	0	0	22766	*	Case 1
8	210	0	0	22766	*	Case 2
9	240	0	0	22766	*	Case 3
10	270	0	0	22766	*	Case 4
11	300	0	0	22766	*	Case 5
12	330	0	0	22766	*	Case 6
13	0	33	0	9444		
14	30	33	0	9444		
15	60	33	0	9444		
16	90	33	0	9444		
17	120	33	0	9444		
18	150	33	0	9444		
19	180	33	0	9444	*	Case 13
20	210	33	0	9444	*	Case 14
21	240	33	0	9444	*	Case 15
22	270	33	0	9444	*	Case 16
23	300	33	0	9444	*	Case 17
24	330	33	0	9444	*	Case 18
25	0	33	90	9444		
26	30	33	90	9444		
27	60	33	90	9444		
28	90	33	90	9444		

*Replace (x_g, y_g, z_g) by ($-x_g, -y_g, -z_g$) in cases indicated in table.

TABLE 4-1. CONT'D

Case	ψ	α	Ω	R		
29	120	33	90	9444		
30	150	33	90	9444		
31	180	33	90	9444	*	Case 25
32	210	33	90	9444	*	Case 26
33	240	33	90	9444	*	Case 27
34	270	33	90	9444	*	Case 28
35	300	33	90	9444	*	Case 29
36	330	33	90	9444	*	Case 30
37	0	33	0	9444		
38	0	33	30	9444		
39	0	33	60	9444		
40	0	33	90	9444		
41	0	33	120	9444		
42	0	33	150	9444		
43	0	33	180	9444	*	Case 37
44	0	33	210	9444	*	Case 38
45	0	33	240	9444	*	Case 39
46	0	33	270	9444	*	Case 40
47	0	33	300	9444	*	Case 41
48	0	33	330	9444	*	Case 42

* Replace (x_g, y_g, z_g) by $(-x_g, -y_g, -z_g)$ in cases indicated in table.

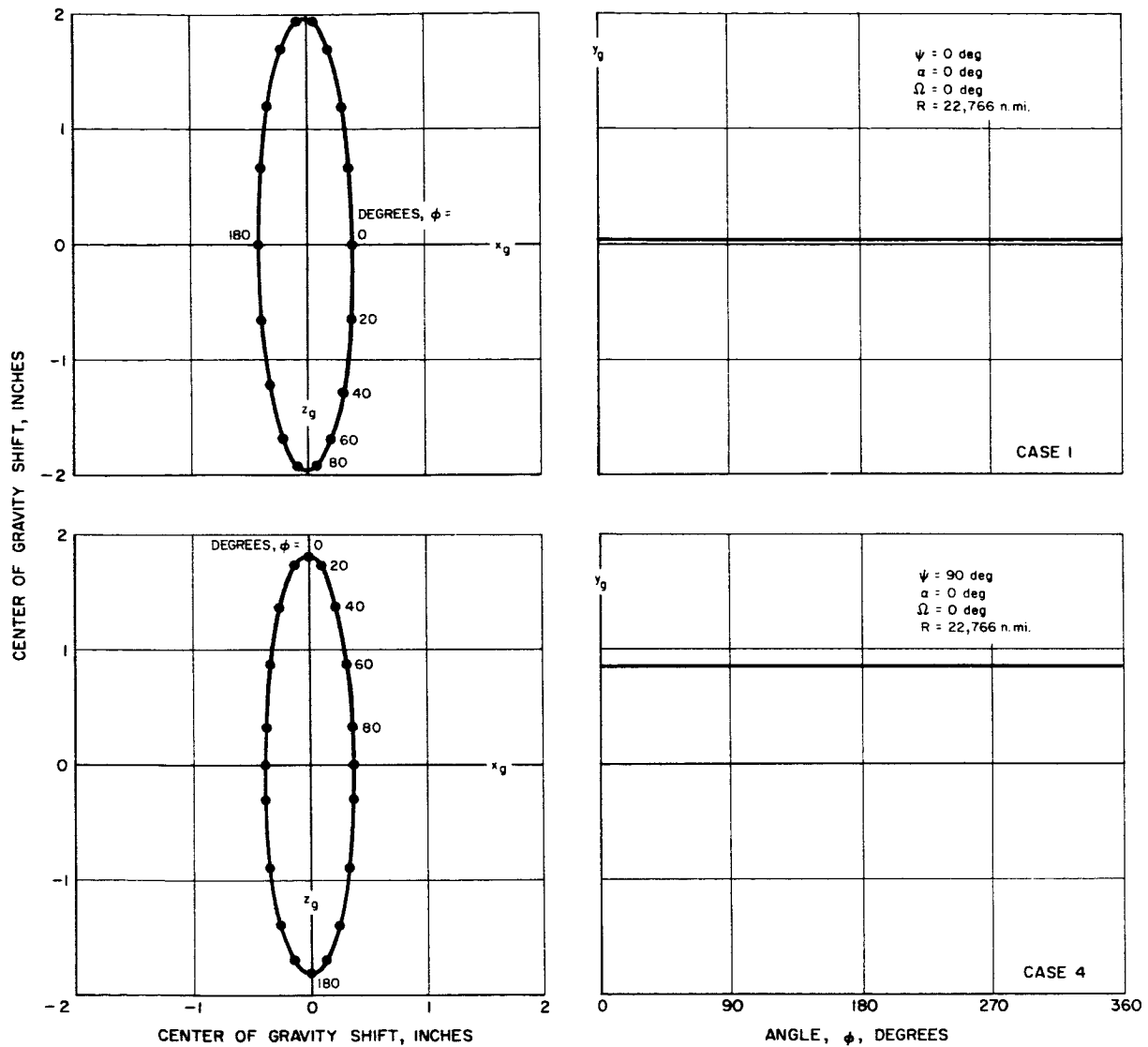


Figure 4-2. Center of Gravity Displacement Due to Thermal Bending

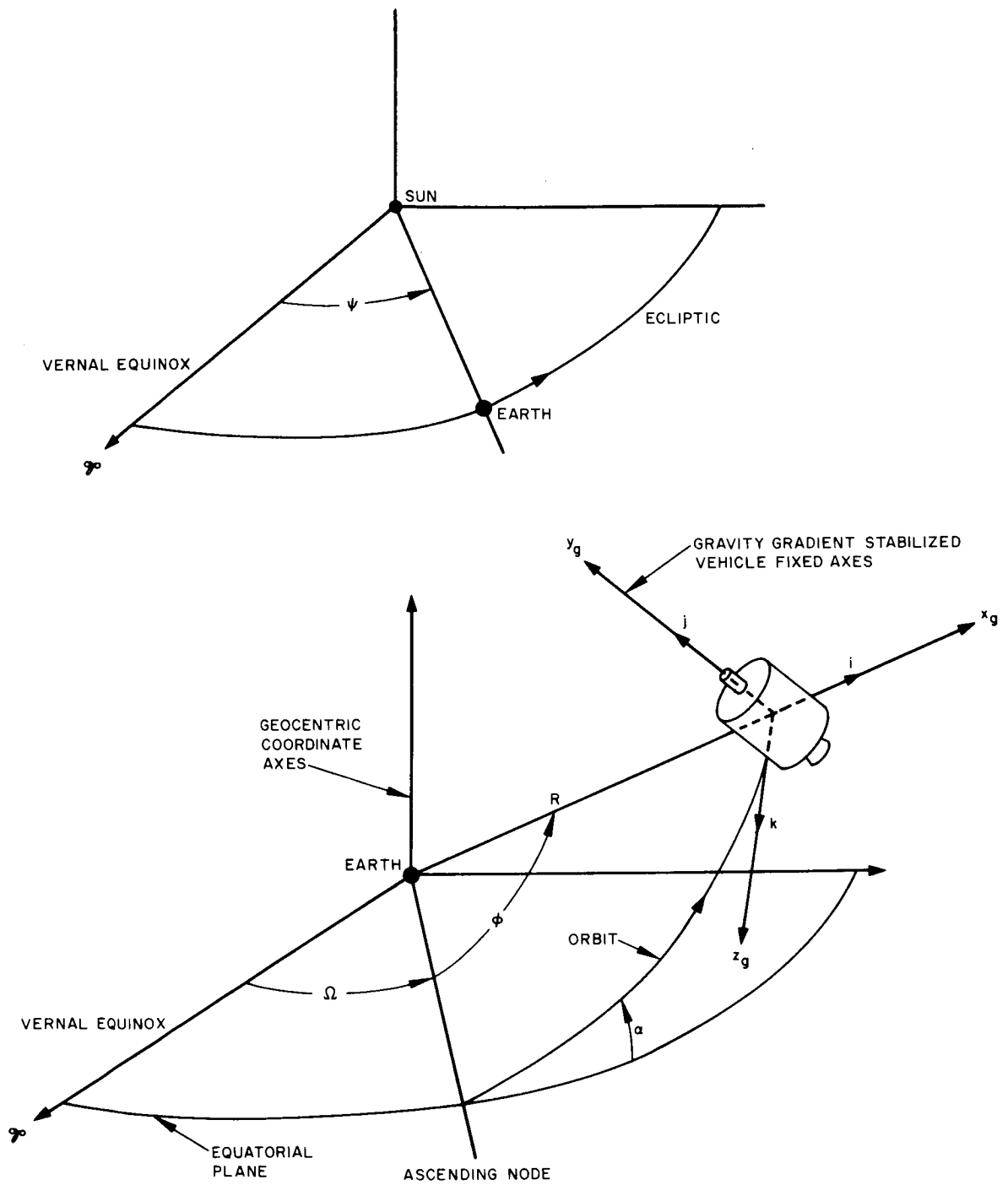
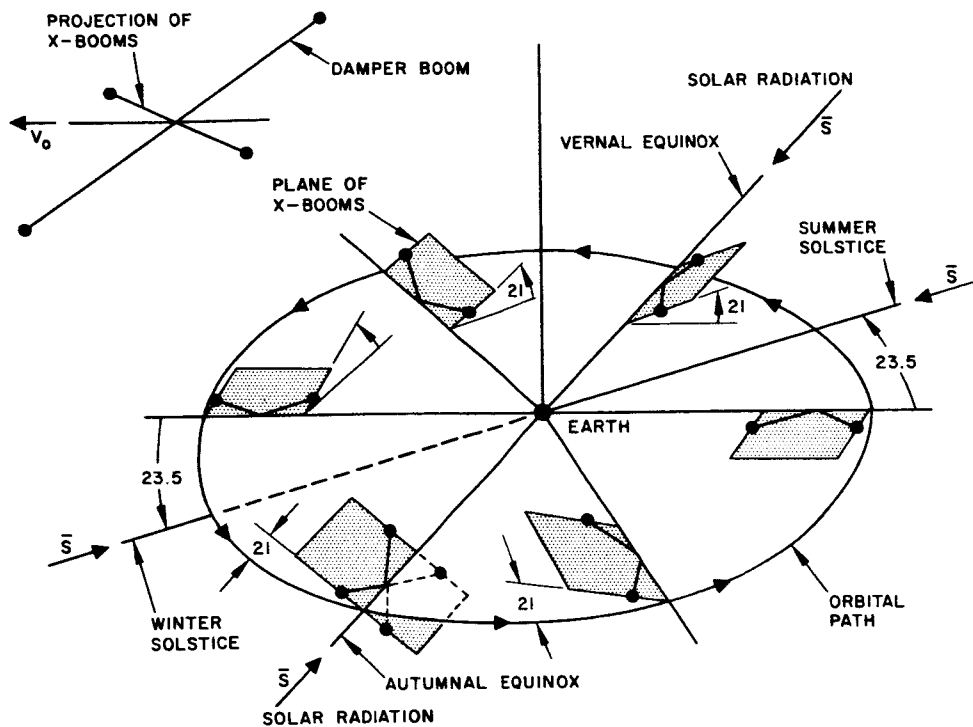


Figure 4-3. Nomenclature Applicable to Center of Gravity Shift Curves



ANGLES IN DEGREES

Figure 4-4. Geometry for Center of Gravity Shift Due to Thermal Bending

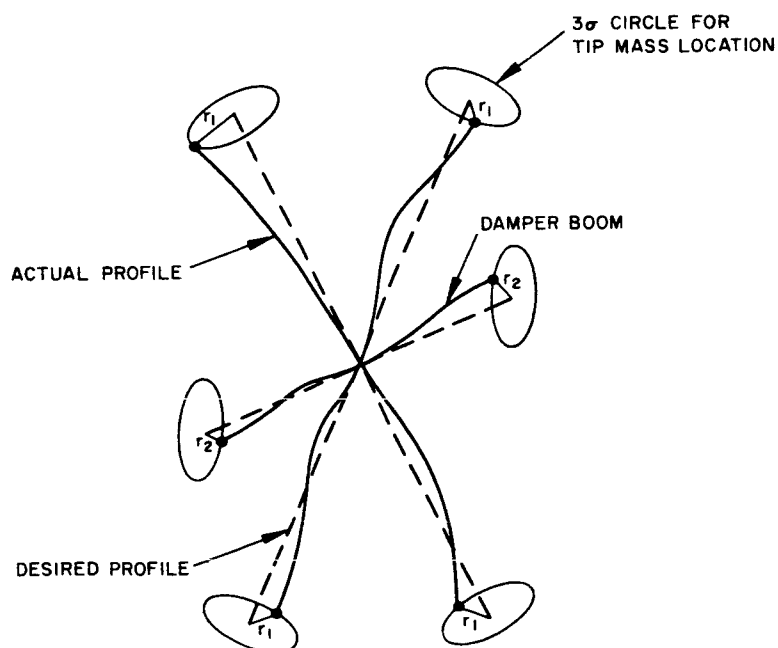


Figure 4-5. Schematic Representation of Tip Mass Displacement Due to Natural Profiles of Booms

(not to scale). The exit direction of the boom is given by the dotted lines. Because the individual natural profiles deviate from a straight line, the tip masses will lie on 3σ displacement circles of some radius. The statistical description of center of gravity displacement resulting from the natural profile is in process. If the 3σ radius of tip mass displacement is large (more than 3 feet), some provision would have to be made for controlling the exit direction or rotating the tube about its axis so that all tip masses could be placed in the proper plane. If r_m is predictable and repeatable but has a random direction, exit direction control (or possibly boom rotation about boom axis) would still be required unless r were significantly smaller than the maximum deflection because of thermal bending. Thermal bending maximum deflection may be in the range 3 to 7 feet.

The effect of the natural profile, if the direction of bending is uncertain, may be approximated by the geometry of Figure 4-6. The boom is tangent to the pay-out direction at the exit point (point of emergence from the central body). Then,

$$h = r \left(1 - \cos \frac{\theta}{2} \right)$$

$$r = \frac{s_1^2}{8h}$$

The displacement d_1 is

$$d_1 = r (1 - \cos \theta)$$

$$\approx \frac{s_1^2}{8h} \left[1 - \left(1 - \frac{s_2^2}{2r^2} \right) \right]$$

$$\approx 4h$$

and the tip mass displacement is

$$d_o \approx \frac{s_o}{s_1} (4h)$$

Typical numbers might be $s_1 = 10$ feet, $h = 2$ inches, $s_o = 100$ feet.

Then

$$d_o \approx \frac{100}{10} (4 \times 2) = 80 \text{ inches}$$

$$= 6.67 \text{ feet}$$

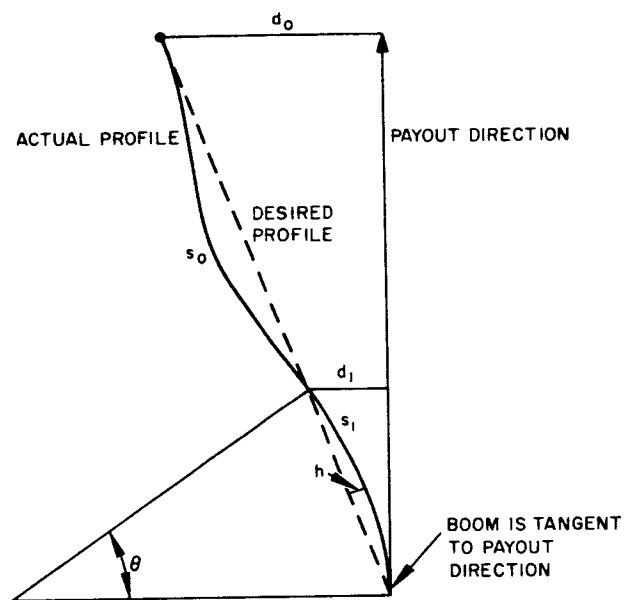


Figure 4-6. Tip-Mass Displacement Geometry Due to Natural Profile

Subsequent discussions with DeHavilland are planned for the purpose of quantitatively defining the natural profile of the booms.

Solar Radiation Torque Compensation

Because of present uncertainties in the angular orientations of the boom tips caused by the natural profile, solar radiation torque compensation is not recommended. Such compensation, if used, would take the form of tip surface areas designed so that the torque normally caused by a pair of opposed booms would be compensated by the changing projected area of the tip surfaces. A simple disk on each tip, with the disk surface positioned normal to the boom axis, would have the desired effect. Since the angular misorientation of the boom tip could be as great as the angular deflection due to thermal bending, the compensation could not be attained. In fact, the disks would produce a radiation pressure disturbing moment when the boom alone would not normally produce a torque.

SYSTEM PARAMETER OPTIMIZATION

The following summary of system parameters, although subject to minor modification as a result of current investigation, represents the present findings regarding "optimum" values.

Moment-of-Inertia Ratios

The moment-of-inertia ratios remain as indicated in the beginning of this section and are the result of computer studies carried out at GSFC.

Moments of Inertia

The moments of inertia remain as indicated in the beginning of this section and are the result of the considerations discussed and the response curves generated by GSFC computer studies (Stabilization and Controls Branch).

Since the capability of varying (decreasing) moment of inertia exists in the MAGGE vehicle, the basic entity here is the maximum moment of inertia (booms fully deployed). This maximum value could be increased by adding tip mass or increasing length. However, there is no justification for increasing the moment of inertia because the vehicle response to solar radiation is less than 1 degree (usually) in pitch and roll and less than 3 degrees in yaw. These values are for a maximum tip deflection of 10 feet, a conservative value if boom reflectivity can be maintained.

However, it does not appear reasonable to decrease the maximum moment of inertia, since the 100-foot length of boom is readily obtainable. The yaw attitude error already exceeds 3 degrees (under certain conditions)

and the advisability of increasing this error is subject to question. The equations may be applied using the curves of Figure 4-7 to arrive at k_1 values and the minimum length then determined in this manner. For example, if twice the attitude error of Figure 4-7 is acceptable, $k_1 = 2$, and $L = 100/\sqrt{3} = 57.7$ feet. This assumes that the solar radiation torque on the central body is equal to the torque on the booms.

Boom Parameters

The important boom parameters are diameter, thickness, coating (plating), and overlap. It is shown in Reference 4-3 that thermal bending is proportional to the profile number

$$N = \frac{1}{4} \frac{e}{k} \frac{d}{t} J_s \alpha_s$$

where

d = diameter

t = thickness

e = coefficient of expansion

k = conductivity

J_s = solar radiation constant

d_s = absorbtivity

The diameter-to-thickness ratio is constrained to some minimum value because of stress requirements in the flattening and curling process. Thus, boom bending can be controlled only by e , k , and α , the latter being subject to some minimum value of about 0.1. e and k do not provide for any significant improvement, leaving N at the value minimized corresponding to minimum α .

It does appear that d should not be increased, with a corresponding increase in t , because the solar radiation torque varies directly as d . The diameter should be a minimum consistent with the requirements for stiffness in the presence of reaction control system operation.

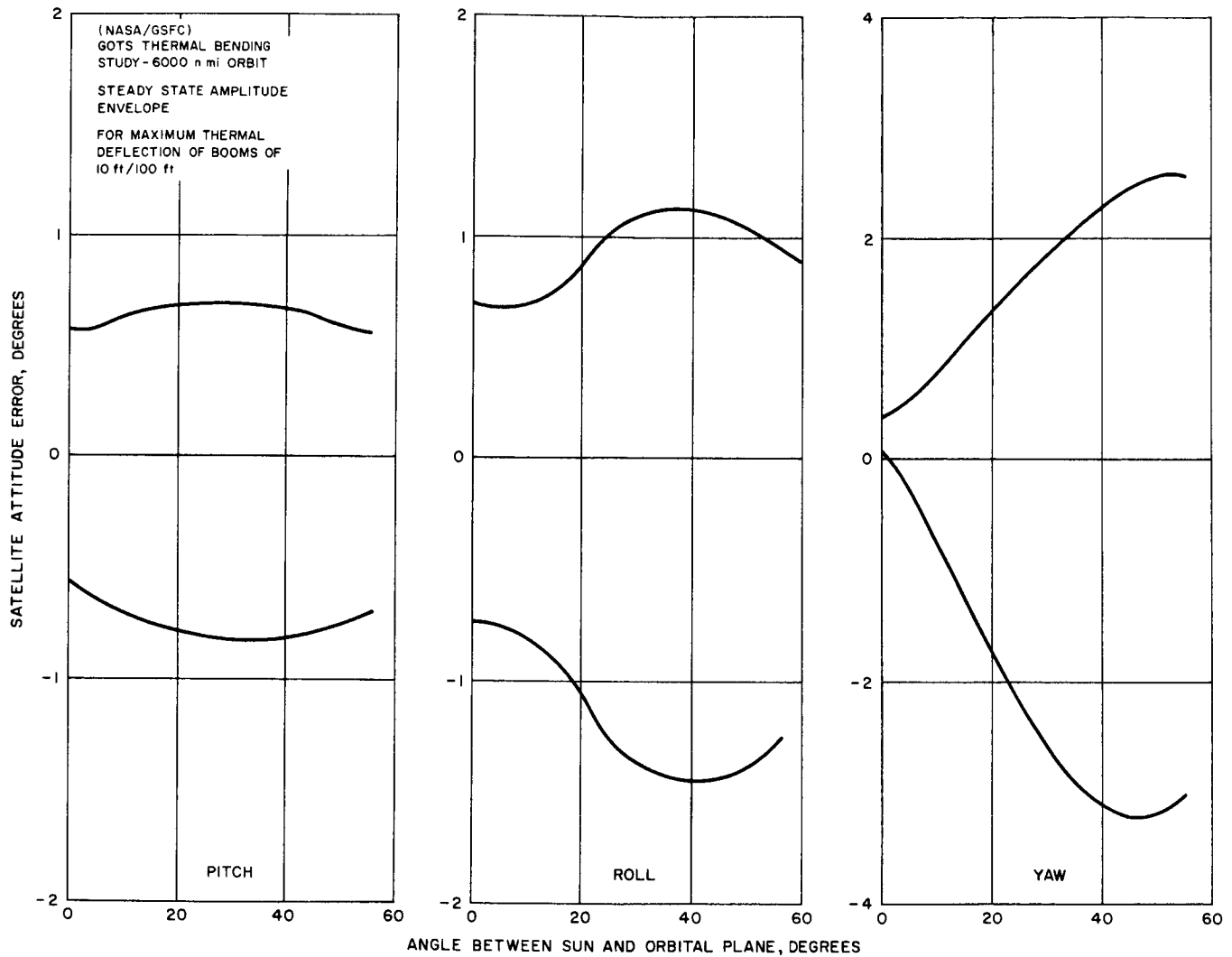


Figure 4-7. Attitude Error Envelopes

BOOM DYNAMICS

Solar Plasma Considerations

The potential problem of mechanical forces on the gravity-gradient booms due to solar plasma streams has been given preliminary consideration. Since it is predicted by many investigators that beyond a region of approximately 8000 miles from the earth's surface a solar plasma pressure on the order of 10^{-5} dynes/cm² exists, the potential perturbing effects on both the spacecraft main body and gravity-gradient booms for the normal plasma and abnormal plasma (i. e. , during active solar "storms") is under investigation. The normal solar plasma forces are approximately 1 order of magnitude less than ordinary light pressure forces on a perfectly reflecting surface, which are on the order of 10^{-4} dynes/cm². However, during a severe solar storm it is expected that the plasma may exert in gusts, pressures of possibly 2 orders of magnitude greater than ordinary light pressure. This would result in pressures of approximately 0.01 dyne/cm² on highly reflecting surfaces. Depending on the length of time of the high solar wind or plasma occurrence, these forces may or may not be a significant perturbation.

Thermal Analysis

The thermal analysis of the gravity-gradient booms has continued. Since the thermal analytical model of the booms does not require that the booms are comprised of closed tubes, this assumption is not necessary to solve for the tube maximum Δt . Therefore, a realistic evaluation can be made of the effect of nonuniform solar insolation on the overlapped tube.

The cross sectional model of the overlapped tube has been analyzed for various solar angles from 0 to 360 degrees to evaluate the radial temperature excursions during the complete cycle of 1 day. The results of this investigation are shown in Figure 4-8. In this investigation, a boom of 0.45-inch diameter, 0.002-inch wall thickness, 0.35 solar absorptance, and a conductivity of 65 Btu/hr ft °F was assumed. The results are indicative of the expected general shape of the temperature profiles for all booms considered. It is seen that the solar angles of 90 and 270 degrees in reference to Figure 4-8 appear to be the most severe from the standpoint of temperature gradient across the boom.

Because of the extremely unpredictable nature of the thermal coupling in the region of the overlapped section of the tube, the conservative assumption was made that conduction in this region was negligible and that only mutual radiation between outer tube and overlapped tube occurred. It is felt that only in the event of high surface pressure and good mutual contact in the overlapped region would overlapping have a beneficial effect in reducing the temperature differential across the tube. If this is not the case, then the overlapping only inhibits cross heat transfer by radiation.

The effects of varying tube wall thickness, diameter, and solar absorptance are shown in Figure 4-9. For the sake of comparison, all cases assume a solar incidence at 0 degrees according to the model shown in Figure 4-8. Therefore, in order to maintain a maximum gradient across the tube in the 2 to 3° F range, a low solar absorptance (0.10) and a low diameter-to-thickness ratio (on the order of 200 to 250) must be utilized.

The complete steady state results to date of the thermal analysis of the gravity-gradient booms are shown in Table 4-2. Various ΔT results are indicated for diameter ranging from 0.45 to 0.75 inch, wall thickness from 0.002 to 0.004 inch, solar absorptance from 0.10 to 0.85, and solar angle from 0 to 450 degrees including overlap. The potentially best boom analyzed was the 0.45-inch diameter, 0.002-inch wall thickness, and 0.10 solar absorptance on outside surface resulting in a temperature differential varying from 1.7 to 3.6° F depending on the boom angle of solar insolation. The mean boom temperature for this configuration is -55° F.

The gravity-gradient booms have been analyzed to determine the transient behavior of the booms during and following a 60-minute eclipse. For the high solar absorptance tube analyzed, the maximum temperature differential in departing from the eclipse apparently did not significantly rise above the normal steady state differential (see Figure 4-10).

STRUCTURAL ANALYSIS

Gravity-Gradient Boom Deflection Studies

Deflections Due to Gravity-Gradient Forces

Boom tip deflections due to gravity-gradient forces have been computed and may be neglected when compared to deflections caused by temperature gradients on the boom natural profile. The deflection analysis assumes the booms are straight after being deployed. Using the notations in Figure 4-11 the gravity-gradient forces and deflections are determined.

The net gravity-gradient force on the boom can be reduced to $3 m_i g R_E^2$ as shown in Figure 4-12. Resolving this force normal and parallel to the boom axis, the deflection for a beam with a simultaneous axial tension load and transverse load is

$$\delta_{\max} = \frac{W}{P} (\ell - j \tanh U)$$

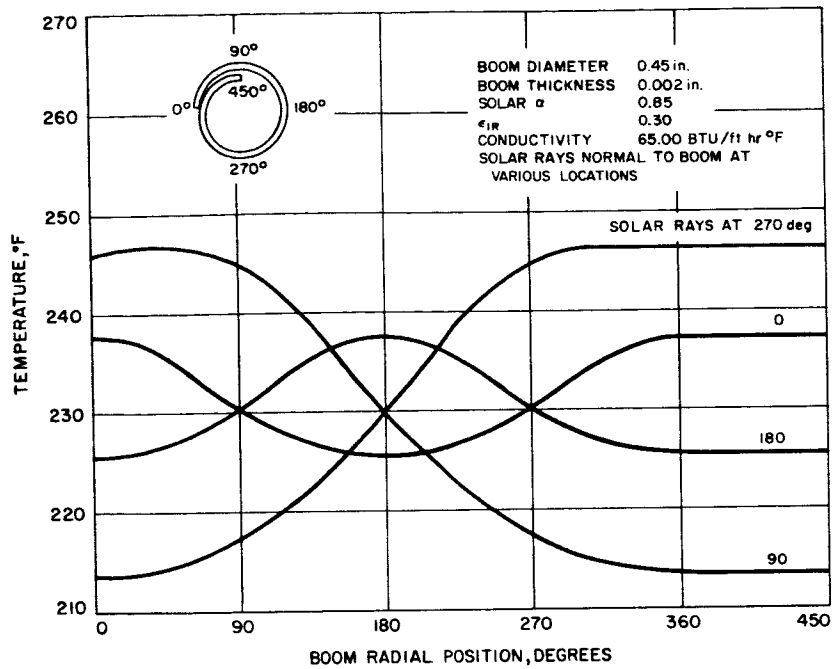


Figure 4-8. Gravity Gradient Boom Thermal Analysis
 Steady state

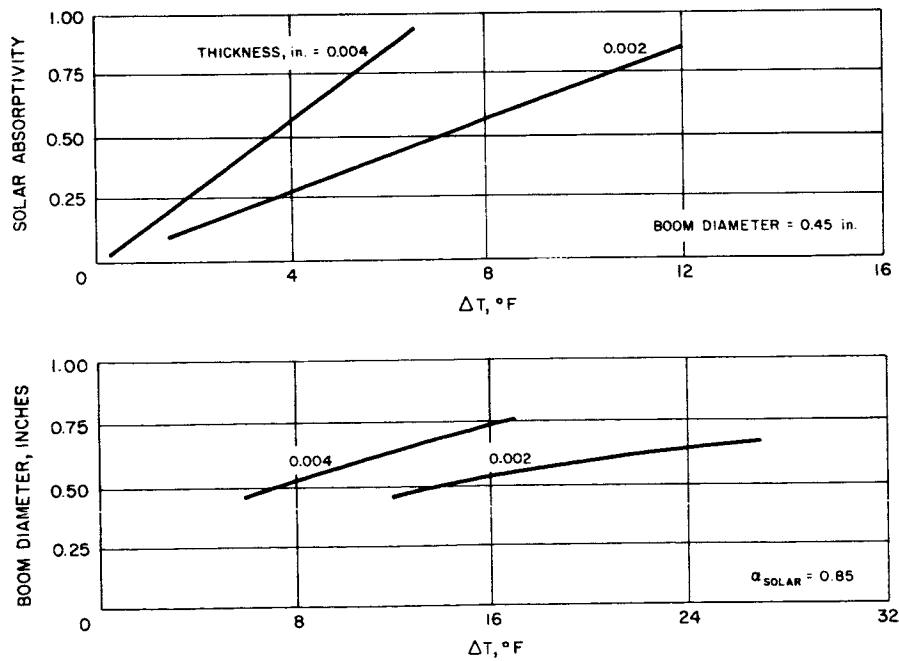


Figure 4-9. Gravity Gradient Boom Parametric Thermal Study
 Sun rays normal to position 0

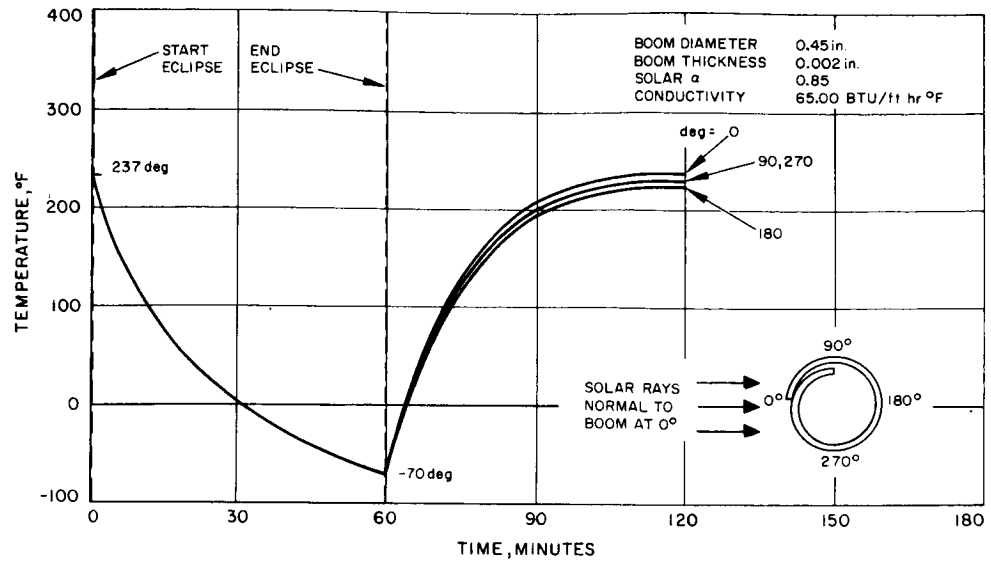


Figure 4-10. Gravity Gradient Boom Thermal Analysis Eclipse Transient Response

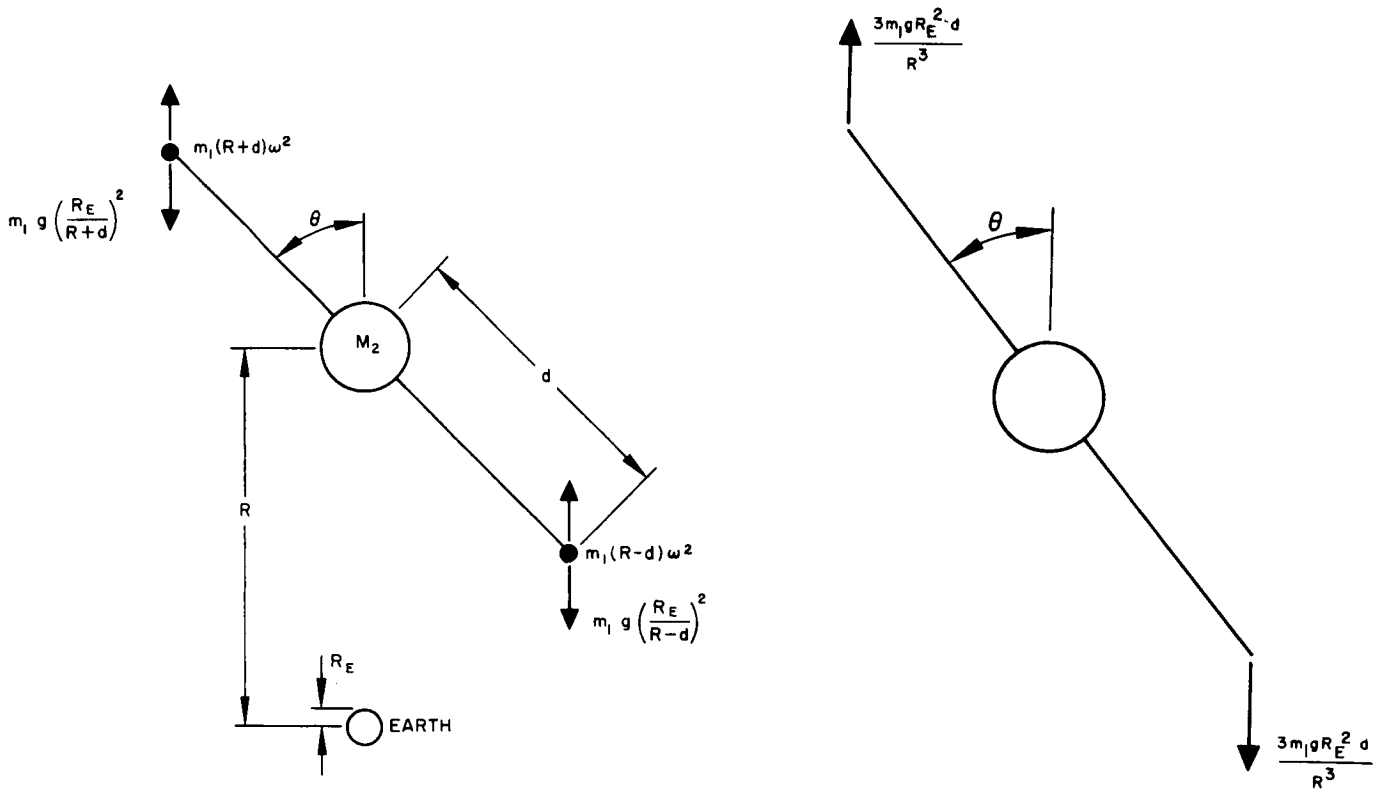


Figure 4-11. Gravity Gradient Forces on Boom Tip Mass

Figure 4-12. Net Gravity Gradient Forces on Boom Tip Mass

TABLE 4-2. GRAVITY-GRADIENT BOOM THERMAL ANALYSIS
STEADY-STATE RESULTS

Boom Diameter, inches	Boom Shell Thickness, inches	α	ϵ	κ	Sun Ray Normal To	Temperatures at Location, °F						ΔT , °F	Remarks
						0	90	180	270	360	450		
0.45	0.002	0.85	0.30	65	0	237	230	225	230	225	237	12	
0.45	0.002	0.85	0.30	65	90	246	245	230	217	213	214	33	
0.45	0.002	0.85	0.30	65	180	225	230	237	230	237	237	12	
0.45	0.002	0.85	0.30	65	270	213	217	230	245	246	246	33	
0.45	0.002	0.50	0.30	65	0	149	144	142	144	149	149	7	
0.45	0.002	0.10	0.30	65	0	-54	-55	-55	-55	-54	-54	1.7	Lower α
0.45	0.002	0.10	0.30	65	90	-54	-54	-56	-57	-58	-57	3.6	Worst Case
0.45	0.002	0.85	0.30	100	0	235	230	227	230	235	235	5	Effect of κ
0.45	0.002	0.85	0.30	30	0	245	229	219	228	245	245	26	Effect of κ
0.45	0.004	0.85	0.30	65	0	234	230	228	230	234	234	6	
0.60	0.002	0.85	0.30	65	0	243	230	222	230	243	243	21	
0.60	0.004	0.85	0.30	65	0	237	230	226	230	237	237	11	
0.75	0.002	0.85	0.30	65	0	249	229	216	229	249	249	33	
0.75	0.004	0.85	0.30	65	0	240	230	223	230	240	240	17	

Legend

α = Solar Absorptivity

ϵ = Emissivity

κ = Thermal Conductivity

where

W = transverse load

P = axial load

l = beam length

$$j = \sqrt{\frac{EI}{P}}$$

$$U = l/j$$

For a beryllium copper boom 100 feet long, 0.50 inch in diameter and 0.003-inch thick, a tip weight of 10 pounds, and R equal to 10,000 miles, the maximum tip deflection is 0.654 inch for $\theta = 19$ degrees.

Moments at center of gravity = $I\ddot{\theta}$ (Refer to Figure 4-12.)

$$-6 m_i g \frac{R_E^2}{R^3} d^2 \theta = 2 m_i d^2 \ddot{\theta}$$

$$\ddot{\theta} + 3 g \frac{R_E^2}{R^3} \theta = 0$$

$$\omega_{cg}^2 = 3 g R_E^2 / R^3$$

Also by equating the centrifugal force on the spacecraft to the gravity force,

$$\omega_{earth}^2 = g \frac{R_E^2}{R^3}$$

or

$$\omega_{earth}^2 = \frac{1}{3} \omega_{cg}^2$$

Deflections Due to Temperature Gradients

Using the equation

$$x = -\frac{d}{\Delta T_e} \ln \cos y \frac{\Delta T_e}{d} \quad (\text{Reference 4-1})$$

to solve for boom deflections, curves of boom tip deflection versus temperature gradient for two configurations are presented in Figure 4-13. Figure 4-14 is a plot of the boom profile for various temperature gradients.

Gravity-Gradient Boom Structural Studies

Considerable time has been spent attempting to derive the boom allowable bending moment and torque equations presented in Reference 4-4.

Allowable Bending Moment Equation

Assumptions:

- 1) The boom can be treated as a long cylinder and its allowable strength can be expressed in the form $F_{\text{allow.}} = CEt/r$ where C is dependent on the cylinder r/t ratio (Reference 4-5).
- 2) The boom overlap factor has no effect on the allowable bending moment.

$$\frac{F_{\text{allow.}}}{f_{\text{actual}}} = F_B$$

$$F_{\text{allow.}} = f F_B$$

$$\frac{2 CEt}{d} = \frac{8 M_d F_B}{2 \pi d^3 t}$$

$$M \text{ (FT-LB)} = \frac{0.131 CE d t^2}{F_B} \quad (4-1)$$

Agreement between Equation 4-1 and the allowable presented in Reference 4-1 is possible if $C = 0.321/1 - \nu^2$.

Allowable Torque Equation

Assumptions:

- 1) $F_{\text{allow.}}$ is derived in Reference 4-5, page 504, for the buckling of a closed cylindrical shell subjected to torsion.
- 2) A 50 percent overlap factor has been used to determine f_{actual} .

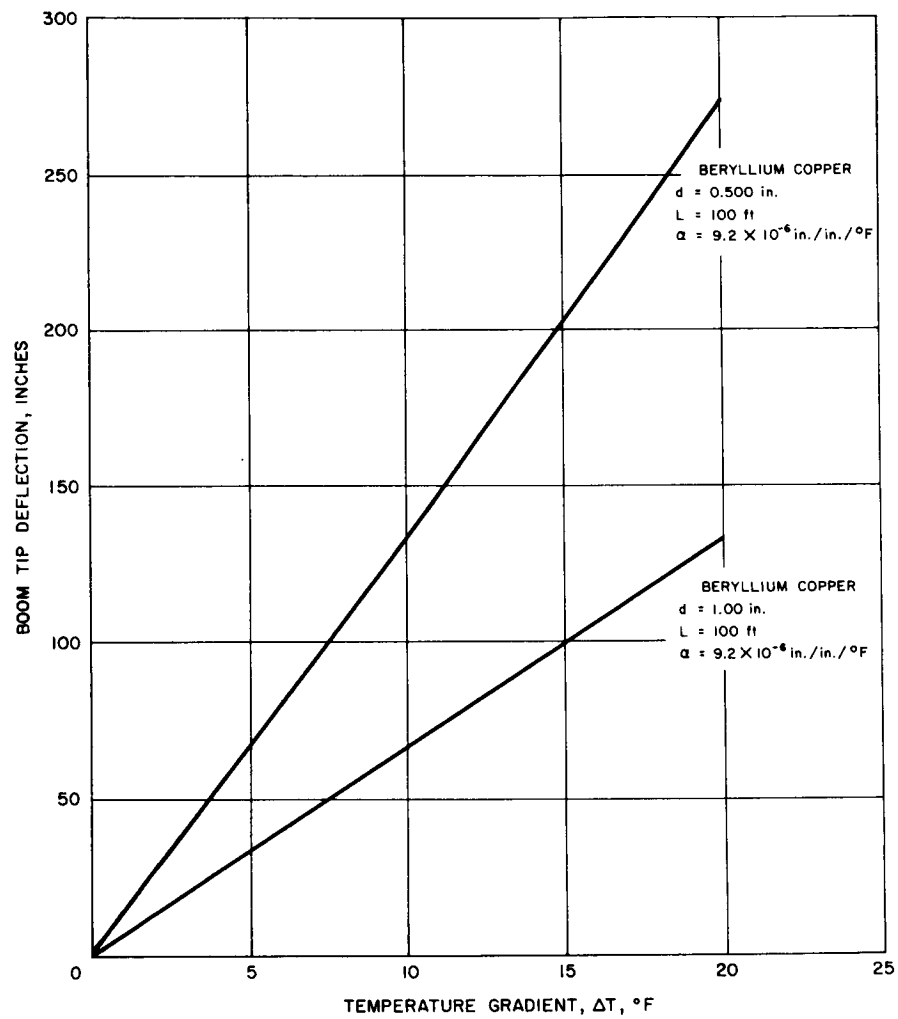


Figure 4-13. Boom Tip Deflection versus Temperature Gradient

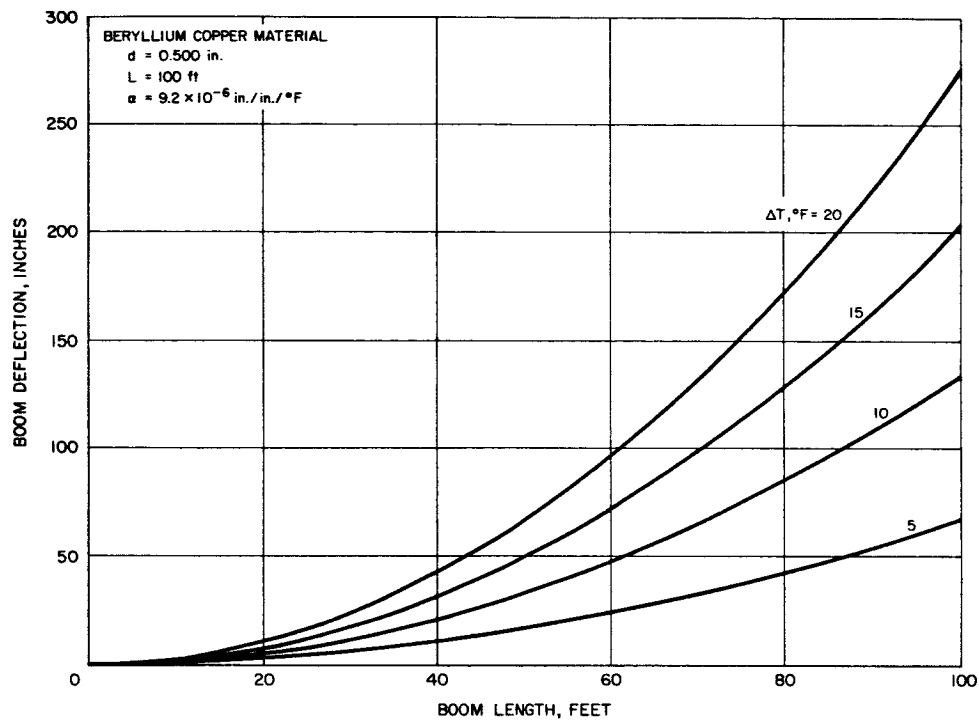


Figure 4-14. Boom Deflection versus Length

$$\frac{F_{\text{allow.}}}{f_{\text{actual}}} = F_B$$

$$F_{\text{allow.}} = f F_B$$

$$\frac{E}{3 \sqrt{2} (1 - 2^2)^{3/4}} \left(\frac{2t}{d} \right)^{3/2} = \frac{3 M F_B}{1.5 \pi d t^2}$$

$$M \text{ (FT-LB)} = \frac{0.087 E t^3}{F_B (1 - 2^2)^{3/4}} \sqrt{\frac{t}{d}} \quad (4-2)$$

Equation 4-2 is in agreement with Reference 4-4; however, it is not apparent that assumption 1) is valid for the analysis of an open tube.

STRUCTURAL DYNAMICS

The primary structural dynamics effort during this reporting period has been in the evaluation of boom tip displacements during orbital maneuvers. The most significant maneuver from this standpoint is change of eccentricity. Control system force amplitudes of 1 to 5 pounds are being considered.

The equations of motion which describe the boom displacement during an indefinitely long pulse train having an arbitrary pulse amplitude, pulse width, and pulse separation time have been solved. The derivation is based on the following approximations:

- 1) The spacecraft was represented by a single boom 200 feet long, having 10-pound tip masses and a 760-pound central mass.
- 2) Boom bending deflections resulting from axial loads were not included.
- 3) Boom bending deflections resulting from torsional loads were not included.

Bending modes were obtained for this spacecraft model by the Myklestad method and provided generalized coordinate data for the response

analysis. The pulse train was represented by a Fourier series. The boom tip displacement is given by:

$$\begin{aligned}
 q_i(t) = & \frac{F\phi_i \lambda}{M_i \omega_i^2} (1 - \cos \omega_i t) \\
 & + \frac{F\phi_i}{M_i \omega_i^2} \sum_{n=1}^{\infty} \left[\frac{1}{n\pi} \left(\frac{\sin 2\pi n \lambda}{1 - n^2 \psi^2} \right) (\cos n \psi \omega t - \cos \omega t) \right. \\
 & \left. + \frac{1}{n\pi} \left(\frac{1 - \cos 2\pi n \lambda}{1 - n^2 \psi^2} \right) (\sin n \psi \omega t - n \psi \sin \omega t) \right] \quad (4-3)
 \end{aligned}$$

where

$q_i(t)$ = boom tip displacement in the i th mode, inches

F = force amplitude, pounds

ϕ_i = modal displacement at the point of application of F in the i th mode

M_i = generalized mass in the i th mode, lb-sec²/in

ω_i = natural frequency in the i th mode, rad/sec

λ = ratio of pulse width to pulse separation time,

ψ = ratio of pulse frequency to first natural frequency

The magnitude of the mode participation factor $\frac{\phi_i}{M_i \omega_i^2}$ is small for all modes

above the first (the second natural frequency is ten times greater than the first). The total response is therefore approximated as that which occurs in the first mode.

It is believed that the minimum tip deflection for a pulse fixed amplitude and width is obtained by pulsing at the half period of the fundamental mode.* This conclusion is based on a parameter study and is not readily demonstrated by differentiating Equation 4-3 with respect to the pulse period. The tip displacement waveform for this type of input is a train of half-sine waves separated by half periods in which the boom is at rest. Thus the response amplitude is identical to that obtained for a single pulse of the same shape. The tip displacement for a single pulse is given by:

$$q(t) = q_0 \cos \omega_i t + \frac{\dot{q}_0}{\omega_i} \sin \omega_i t \quad (4-4)$$

For the range of pulse widths treated here the initial displacement is approximately zero, so

$$q(t) = \frac{F \phi_i \tau}{M_i \omega_i} \sin \omega_i t \quad (4-4')$$

where τ = pulse width, seconds.

Equation 4-4' is the basis for the graph of Figure 4-15, which shows tip displacement amplitude versus the time required to complete the eccentricity maneuver.

The tip displacement associated with a continuously applied force of interest in the selection of control systems. From Equation 4-3 with $\lambda = 1$ the response to the continuously applied pulse is

$$q_c(t) = \frac{F_c \phi_i}{M_i \omega_i^2} (1 - \cos \omega_i t) \quad (4-5)$$

For the given impulse I and total maneuver time T the relationship between a periodically applied force F_p and a continuously applied force F_c is

$$F_c T = F_p \tau N \quad (4-6)$$

where

N = number of pulses

* A related analysis of the response of a single degree of freedom system to uniformly spaced pulses indicates that both half-period pulsing and third-period pulsing will result in the same response for equal impulse per pulse. The total maneuver time is, of course, reduced by pulsing at third-period intervals.

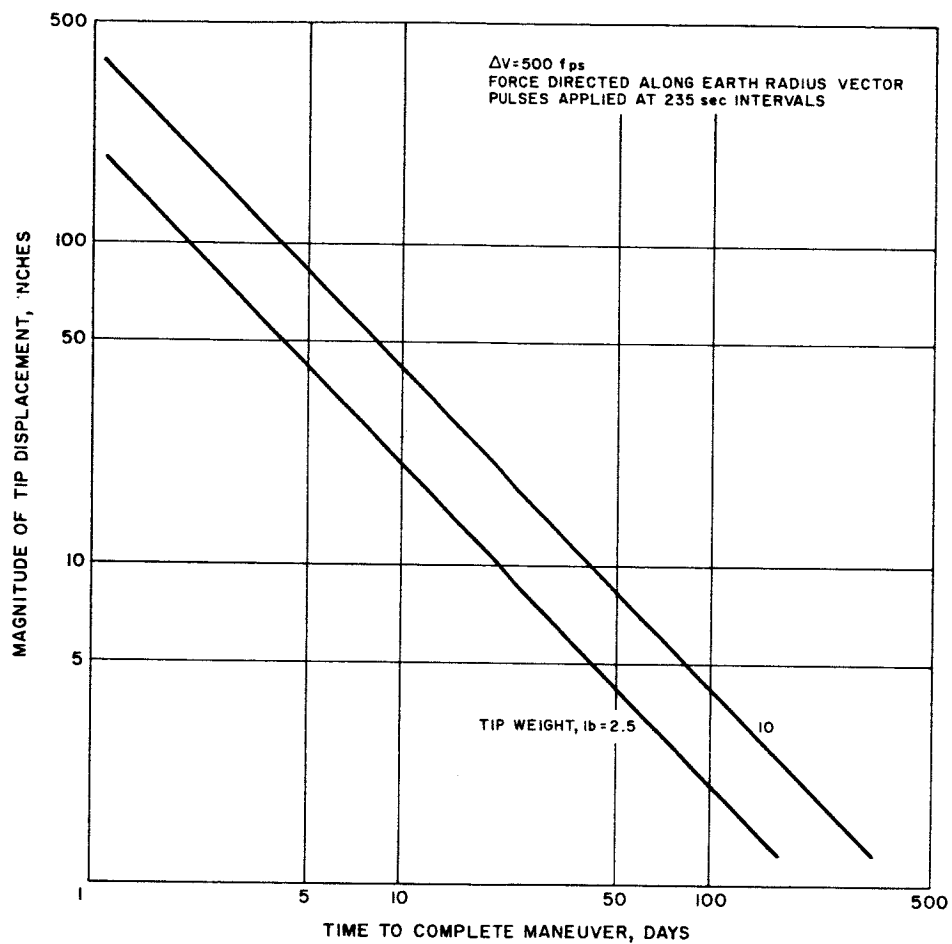


Figure 4-15. Boom Tip Response During Eccentricity Change

Applying the periodic force at the half-period of the fundamental mode
 $(T_i/2 = 235 \text{ seconds})$

$$q_p = \frac{F_c \phi_i T}{NM_i \omega_i} \sin \omega_i t \quad (4-7)$$

The ratio of tip amplitudes is then

$$\frac{q_c}{q_p} = \frac{2N}{\omega_i T} = \frac{2}{\pi} \quad (4-8)$$

Bending moments at the root of the boom have been calculated for the spacecraft model described previously. The results indicate that this will not be an important design consideration. A tip amplitude of 40 inches, for example, results in a maximum root bending moment of 0.23 in -lb.

VELOCITY CONTROL SYSTEM STUDY

A digital computer simulation of the gravity-gradient vehicle was obtained from GSFC. The computer program was modified to be compatible with Hughes equipment. Comparison solutions were run, were checked against similar cases run at GSFC, and optimum agreement was obtained.

The simulation is being used to determine the vehicle response to velocity control induced disturbance torques. Constant and time-varying torques are being studied. The purpose of the study is to establish limitations on velocity control systems that do not require active stabilization. In particular, several schemes for making orbital eccentricity changes at medium altitude are under investigation. The first of these is changing eccentricity by tangential thrusting, both continuously and pulsed. The second scheme is radial thrusting. A significant portion of this study will be completed and reported in later reports.

The simulation is also being used to determine allowable initial capture rates. Preliminary results indicate no capture problem at medium altitude. At synchronous altitude, it is now obvious that a simple yo-yo device is not sufficient to ensure capture. Two alternate methods are being investigated and results of this study will also be reported in the Summary Report.

MECHANISMS

Boom Deployment

The DeHavilland Aircraft Company of Canada gravity-gradient boom deployment mechanism continued to receive primary consideration. Major problems were defined as the result of a conference on 9 December 1963 with members of the Special Products and Applied Research Division. The following are considered the major problems:

- 1) The repeatable deviation of the booms from a straight line and the resultant tip mass displacement. To the degree this error is repeatable and therefore predictable; it can be compensated for in preflight adjustments.
- 2) The nonrepeatable deviations of the booms from a straight line and the resultant uncompensated position error of the tip mass is a major determinant in the selection of the particular model to be used because this characteristic has been determined for only a few models. Only one type of unit was recommended for the required position predictability.
- 3) Development lead time for the DeHavilland boom deployment mechanism is such that any substantial change to existing designs will not be practical for this project. This development lead time must include a sufficiently extensive investigation of prototype units to establish the required extended tip position predictability.
- 4) Development lead time precludes entirely new approaches to the boom deployment mechanism for the same reasons indicated in the preceding paragraph.
- 5) The design of the DeHavilland boom deployment units does not appear to provide sufficiently for mechanical friction problems of all rubbing surfaces in high vacuum. The units exhibited are reliable only for a single operation in high vacuum for a limited time if there were no substantial temperature reduction of the unit while in the vacuum prior to operation. These units would be considered unsuitable for any repeated operation such as adjustment of boom length to change satellite stability parameters.

A weight evaluation of several methods for changing the boom angle has been made of three designs shown in Figure 4-16. The cable design weighed 3-1/4 pounds; the straight linkage system weighed 3 pounds; and the screw and linkage system suggested by Goddard Space Flight Center was the lightest at less than 2 pounds. This low weight was achieved by using a special anodized aluminum screw and glass filled teflon nut developed for the

Surveyor spacecraft project. Figure 4-17 illustrates this design. The screw is hollow with a 0.037-inch wall and is made of 7075-T6 anodized aluminum. The root thickness of the acme shaped thread was reduced so that the shear strength of the aluminum matched the bearing strength of the 25 percent glass-filled teflon nut. Thus, the screw weight was reduced 30 percent while the load carrying capacity of the screw and nut combination remained the same. This nut and screw has been extensively high vacuum tested by Hughes.

Boom Design

The comparison standard for boom design has been the extendible tube formed from preformed metal strip. A better boom must be as stiff, light, and as thermally stable as this standard, and improve on its major problem, straightness. Booms which are "made on board," that is extruded, zipped, or welded together booms, have been excluded since they are not likely to improve on the standard's straightness.

A clear plastic, thin-walled tube was considered. Wall transparency would reduce thermal effects. The tube could be checked for straightness on earth, then stowed, rolled up, and expanded into space with a gas. Ultra-violet light or the gas itself would then harden the plastic into a permanent tube. Unfortunately, plastic material to meet the requirements has not been located to date.

The one other way gravity-gradient stabilization can take place is by attaching the mass to the satellite with a thin wire. An 0.004-inch wire 3000 feet long only weighs 0.1 pound. The unbalanced accelerations experienced by a mass this far out of stable orbit create forces many times those experienced by a weight only 100 feet from the satellite. This force is able to create a restoring torque considerably larger than the 100 foot boom concept, even though the moment arm is only the satellite radius (29 inches). Although this system would damp out oscillations in all three axes, it would have no preferred orientation on the yaw axis. A short boom could be used to provide fixed east-west orientation. A deeper study of this concept will be made, particularly for use at synchronous altitude.

Gravity-Gradient and Libration Damper Booms

Although several companies are working in the area of extendible structures for space vehicles, a review of the literature shows that most of the fundamental development work has been done by the DeHavilland Aircraft Company, in conjunction with the National Research Council of Canada.

The acronym, STEM (Storable Tubular Extendible Member), is used by the DeHavilland Company to identify their family of extendible devices. It is from these basic units that such mechanisms as General Dynamics Verti-stat and Bell Telephone Laboratories PGAC appear to have been derived.

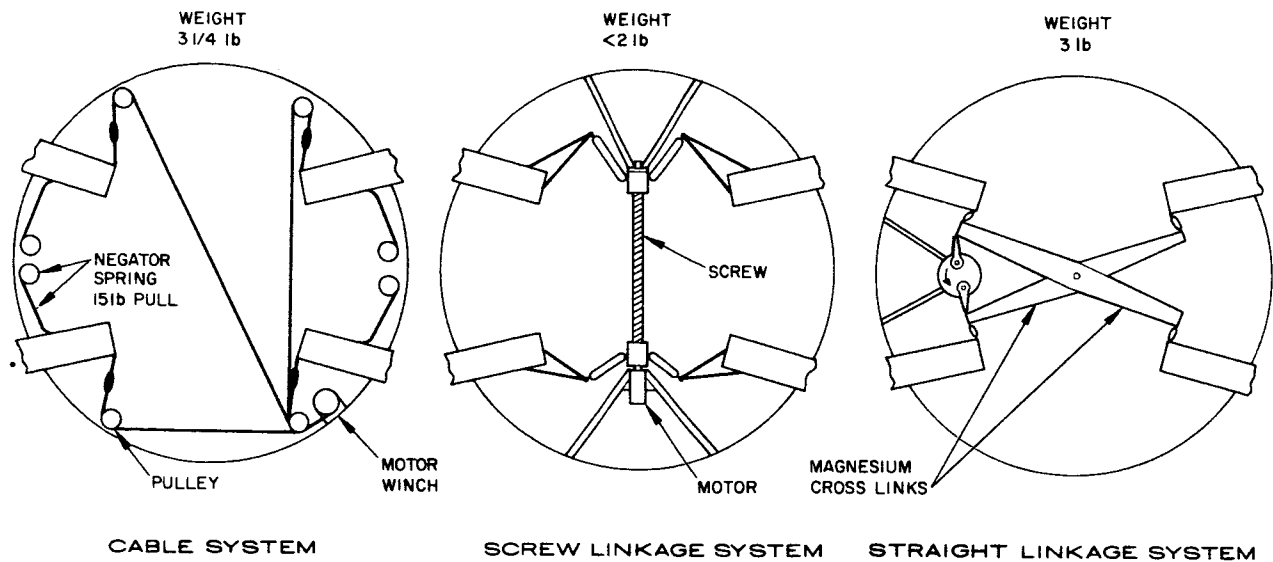


Figure 4-16. Typical Boom Deployment Mechanism

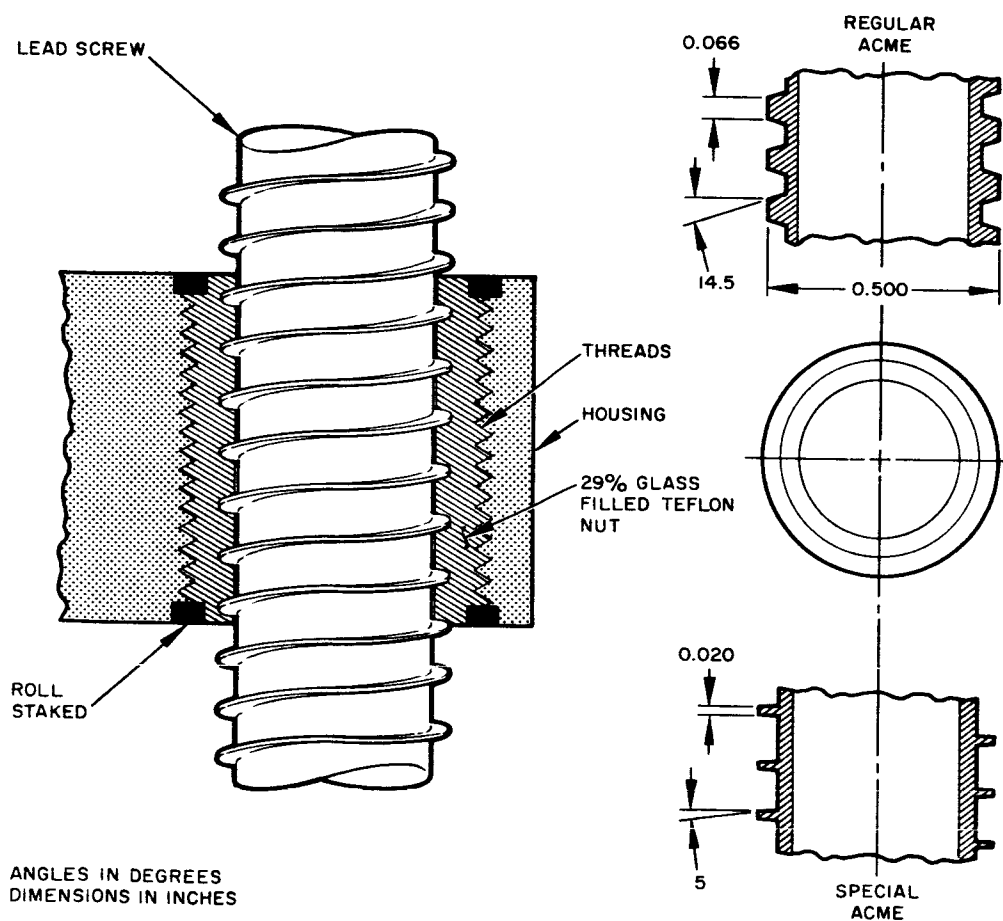


Figure 4-17. Boom Deployment Screw and Nut Mechanism

There are three basic STEM concepts. All employ metal tape pre-formed into a tubular section, but the method of stowage and release depends on the specific application.

The simplest type releases one end of the axially-compressed tape to seek its helically-coiled free form. This so-called "jack-in-the-box" arrangement may be used for relatively short antennas, but it is not suitable for long booms.

The two STEM variants that are capable of controlled extension with both tip weights employ tape stowage spools.

For applications requiring extension and subsequent retraction of tip weights the tape spool may be motor driven and retained on the parent vehicle. The DeHavilland A-16 unit used on the Traac Satellite is a typical example of this type. An alternative arrangement with the motor attached to the extending end of the boom to form the tip weight appears feasible, but no units of this type are known to be in development. Formidable difficulties might be anticipated in supplying power to the motor from the vehicle, and tip-mounted batteries would be subject to undesirable temperature extremes.

For applications requiring only the controlled extension of boom and tip weight the self-driving free-spool version offers minimum weight, volume, and complexity. Rate of boom extension can be readily controlled by means of a governor housed in the spool. The governor may be driven conveniently by a trailing arm and follower arranged to track on the extending boom. The General Dynamics Vertistat employs this principle and it is understood that excellent reliability has been achieved.

In the absence of a requirement to retract the booms a free-spool design appears to be the logical choice for both the SAGGE and MAGGE designs.

On the basis of the foregoing, a first cut free-spool device was sized for the SAGGE X-booms. Since the tip weights for the SAGGE libration damper booms are within 10 percent of the X-boom weights similar boom and spool assemblies were considered suitable for the damper.

Preliminary design layouts were prepared to investigate the merits of various boom attachment locations. This work led to a tentative arrangement with the libration damper and two X-boom assemblies installed aft, with the booms positioned so as to extend clear of the edge of the solar cell panels. The damper and X-boom assemblies were positioned to obtain dynamic balance about the spin axis. Two X-boom assemblies were located near the center of gravity station, with provision for the booms to extend through open areas of the solar cell panels.

Since the preceding arrangement results in a rather marginal ratio of roll-to-pitch inertias, further design work was directed toward possible methods of improving this condition.

A satisfactory ratio of inertias can be obtained by extending three or more masses radially from the spin axis on or near the center of gravity station after shroud separation. Inasmuch as it is undesirable to add ballast weights for this purpose a design layout was prepared to illustrate the feasibility of extending the four X-boom spool assemblies. Such a configuration provides an adequate ratio of inertias with the X-boom spools relocated on the 57-inch radius. The X-booms are subsequently deployed from the relocated attachment locations.

An intensive investigation is under way to relocate components on the spacecraft to achieve an acceptable roll-to-pitch ratio without the complexity of extendible stabilizer booms.

INSTRUMENTATION PACKAGE

Television Subsystem

The camera field of view is 50 degrees in the plane of the spacecraft longitudinal axis and 64 degrees in the lateral plane. Based on this view angle and a camera resolution of 450 lines at the edge of the picture, the gravity-gradient boom targets must be approximately 3 inches in diameter to occupy one resolution element at 100 feet. Since the background light level can be bright when the boom targets are in front of the earth or black when space is the background, it is necessary to provide a black and white target with black and white elements each providing a 3-inch diameter area for the camera; therefore, the targets will be 6 inches in diameter with alternating black and white quadrants. Another consideration in determining target size is that the 1/2-inch booms may hide the target, e. g., if the camera field intersects the booms 10 feet out from the spacecraft, the 1/2-inch diameter boom would hide a target 5 inches in diameter at the end of the 100-foot booms when boom bending occurs in the plane of the boom and camera lens.

Center picture resolution of 500 lines will provide definition of earth land masses of 22 n. mi. at the subsatellite point and 32 n. mi. at 60 geocentric degrees from the subsatellite point for the 6000 n. mi. orbit. Spacecraft attitude in pitch and roll can be resolved to ± 0.2 degree relative to the camera axis. Yaw attitude information can be determined to within ± 1 degree for identifiable land mass separation of 1800 n. mi. and to ± 0.3 degree for land mass separation of 6000 miles.

Gravity-gradient boom surveillance during the inversion maneuver is desirable for determining boom behavior during thrusting. Since the

television video is wideband, information transmitted to the ground stations over the communications (4 kmc) frequencies and the TV data is not recorded on-board. Boom surveillance is limited to real-time antenna coverage of the earth or 40 degrees and 18 degrees maximum at the beginning and end of the inversion maneuver for the 6000 n.mi. and synchronous orbits. Further study will relate the ground station locations to the orbits to determine the best time and longitude for the inversion.

Infrared Earth Sensor

Figure 4-18 is an exploded view of the earth sensor presently being developed by STL under contract to NASA. The infrared lens diameter is 3 inches and the sun sensor aperture is about 1/2 inch.

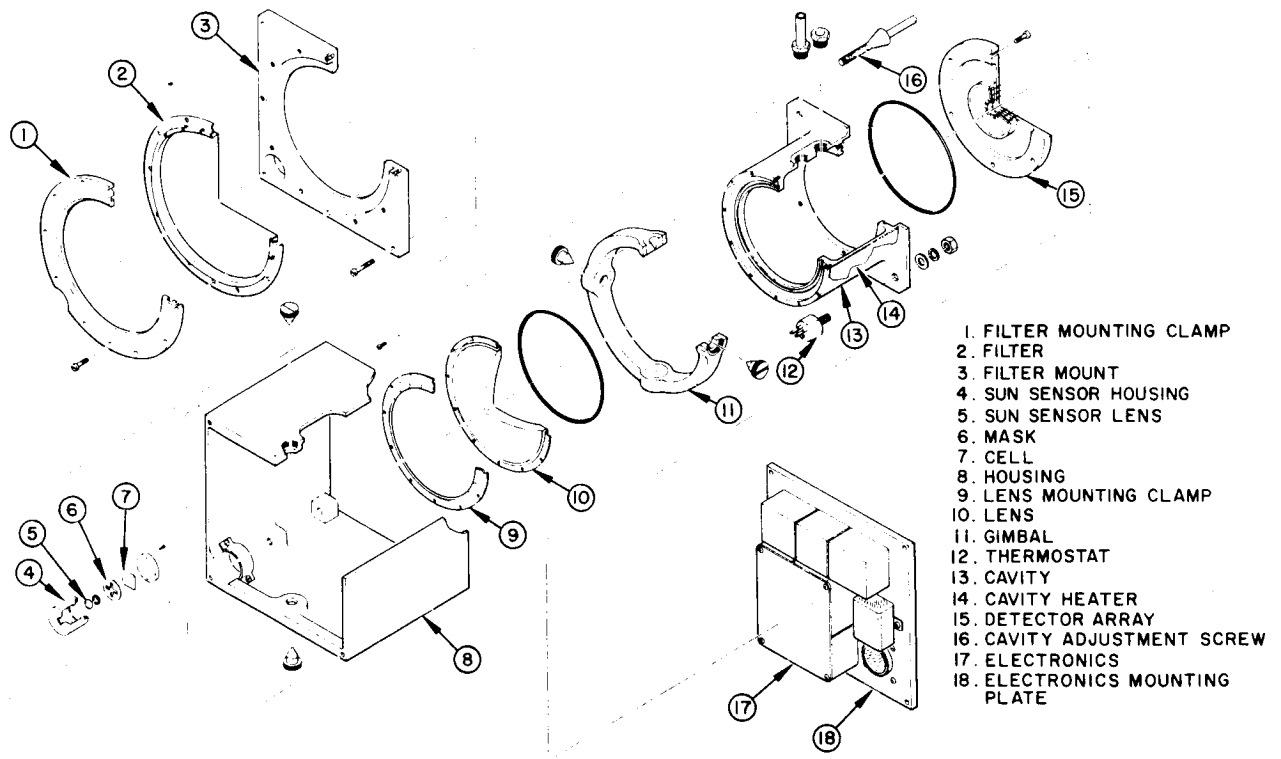


Figure 4-18. Reliable Earth Sensor

REFERENCES

- 4-1. Richard B. Kershner, "Gravity-Gradient Stabilization of Satellites," *Astronautics and Aerospace Engineering*, September 1963, p. 18-22.
- 4-2. B. Paul, J. W. West, and E. Y. Yu, "A Passive Gravitational Attitude Control System for Satellites," *Bell System Technical Journal*, September 1963.
- 4-3. "Studies Carried Out for Naval Research Laboratories under Contract No.: NONR 3592(00)(X). DHC-SP-TN 164, Temperature Gradients and Profile Changes in Long Tubular Elements Due to Incident Radiation; DHC-SP-TN 166, Methods for Joining Tubular Overlapped Elements; DHC-SP-TN 167, "Investigation of the Natural Profile of Long Tubular Elements," DeHavilland Aircraft Company Report, December 1962.
- 4-4. J. D. MacNaughton, "Unfurlable Metal Structures for Space Exploration," Ninth Annual American Astronautical Society Interplanetary Missions Conference, Los Angeles, California, 1963.
- 4-5. G. Gerard and H. Becker, "Handbook of Structural Stability, Part III—Buckling of Curved Plates and Shells," NACA TN3783, August 1957.
- 4-6. Timoshenko and Gere, "Theory of Elastic Stability," Second Edition, 1961.

5. SPACECRAFT SYSTEMS DESIGN

GENERAL STATUS REPORT

During this reporting period most of the decisions have been made which define the make-up of each satellite for a five satellite program. Table 5-1 lists the payloads for each vehicle launched. The Reaction Control System parametric study has been completed and has resulted in the following GSFC approved systems for each vehicle.

Synchronous Altitude Spin Stabilized Vehicles

- 1) Two independent 5-pound thrust (pulsed) hydrogen peroxide lateral jets.
- 2) Two independent 5-pound thrust (pulsed and continuous) hydrogen peroxide gimbaled axial jets.

Synchronous Altitude Gravity-Gradient Stabilized Vehicles

- 1) Three 10^{-5} -pound thrust (continuous) valveless subliming solid jets for inversion and east-west stationkeeping.
- 2) One 5-pound thrust (pulsed) hydrogen peroxide lateral jet.
- 3) One 5-pound thrust (pulsed and continuous) hydrogen peroxide axial jet.

Medium Altitude Gravity-Gradient Stabilized Vehicle

- 1) Two independent 10^{-5} -pound thrust valveless subliming solid jets for spacecraft inversion.
- 2) Two independent hydrogen peroxide fixed jets (between 5 and 1 pound thrust) for effecting an eccentricity change of 0.02. The system must be capable of providing disturbance pulses at various eccentricities.

TABLE 5-1. PAYLOAD COMBINATIONS FOR FIVE LAUNCHES

Satellite Payloads	Satellite Vehicles				
	Spin Stabilized		Gravity-Gradient Stabilized		
	Synchronous	Altitude	Medium Altitude	Synchronous	Altitude
Hughes transponder	1	1	1	1	1
Department of Defense transponder		1	1		
COMSAT transponder		1			1
RF propagation		1			
Phased array antenna	1				
Mechanically despun antenna		1	*	*	*
Meteorological	1		1	1	
Nuclear arms control			1		1
Engineering experiment	1		1		
Radiation	1		1	1	
Gravity-gradient instrumentation			1	1	1

*A nonspinning antenna will be used on all gravity-gradient stabilized vehicles.

Detailed spacecraft subsystem design has continued. The power profiles accompanying the various spacecraft configurations have provided a better definition of the power requirements and therefore the solar cell area required for each vehicle. Thermal studies have resulted in proposal of a well insulated spacecraft to avoid extreme temperature swings of the payloads. Structure detailing is moving forward based on the payloads to be carried and the reaction control system choices made. Mass properties of the various combinations are being defined and package placement predicted upon retaining desirable roll-to-pitch ratios.

Transponder Status Discussion

Effort during this period has been directed towards measuring the intermodulation distortion of the transponder and to design improvements to certain minor control items considered to contribute significantly to intermodulation distortion.

Test Performance Summary and Test Data

Intermodulation distortion tests were performed on the frequency translation transponder and the results compared to the figures obtained when a 6112 mc to 4120 mc mixer was inserted in place of the transponder. The results are listed in Table 5-2.

TABLE 5-2. INTERMODULATION DISTORTION TEST RESULTS

Notch Center Frequency, kc	Noise Power Ratio, db	
	With Transponder	Without Transponder
105	35	34.5
534	37	38
1002	36	40
2438	32	37
3886	28	31

The effect of the transponder beacon on intermodulation distortion was measured and the results are as follows.

Notch center frequency	1002 kc
NPR with internally generated beacon	24 db
NPR with beacon disabled at limiter ampere	37.5 db
NPR with externally generated beacon of 0.75 milliwatt	37.5 db

The degradation was found to originate at the master oscillator chassis. This unit has been shown previously to have internal feedback from beacon output to the 64 mc output driving the X32. The problem has been previously resolved to faulty internal finger stock contact.

The effect of the transponder TWT (4120 mc) on intermodulation was measured. The results listed in Table 5-3 indicate that the TWT has little effect at this noise power ratio.

TABLE 5-3. EFFECT OF TRANSPONDER TWT
ON INTERMODULATION

Notch Center Frequency, kc	Noise Power Ratio, db	
	TWT In	TWT Out
105	34	34
534	36	36
1002	35	35
2438	30	30
3886	27	27

Circuit and Product Design Discussions for Items Under Revision

T Junction. The T-Junction design has been completed. The prototype has been finished and RF tested. Parts for three breadboard assemblies are 85 percent complete.

Input Mixer. Tooling has been completed for the stamped sheet metal ground plane mixers. Parts fabrication and plating is about 50 percent complete.

6 K MC Isolator. The first isolator has been delivered. Its characteristics are shown in Table 5-4.

Multiple Access Master Oscillator Amplifier. One unit has been found to generate spurious sidebands near the carrier. An investigation is currently being made to determine the cause.

Multiple Access Doubler Amplifier. The class A operated unit has been completed and will be used in system tests in the near future.

TABLE 5-4. ISOLATOR 475119 CHARACTERISTICS

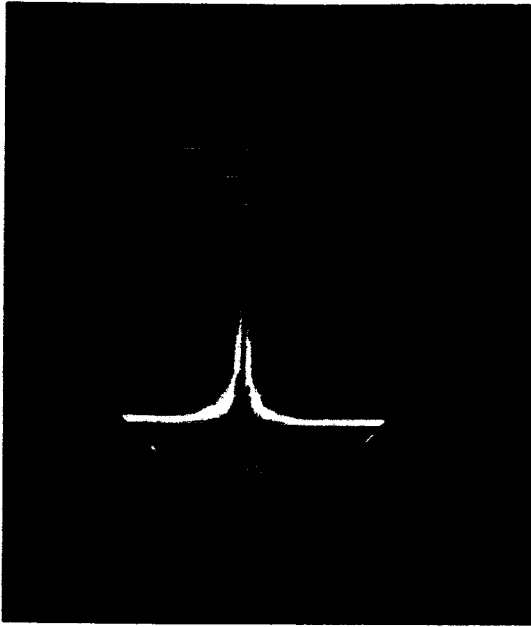
Weight 0.6 ounces

Frequency, mc	Voltage Standing Wave Ratio		Insertion Loss, db	Isolation, db
	In	Out		
5.9	1.20	1.34	0.25	18
6.0	1.15	1.08	0.20	23
6.1	1.14	1.06	0.20	23
6.2	1.13	1.06	0.20	25
6.3	1.13	1.10	0.20	22
6.4	1.17	1.18	0.20	16
6.5	1.25	1.28	0.25	13

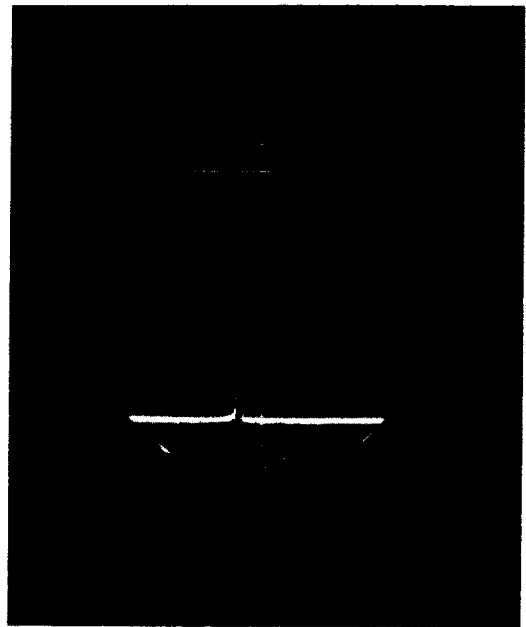
Multiple Access Master Oscillator. The circuit of the multiple access master oscillator has been changed to reduce the amount of noise which appears in the output. The original circuit (Figure 5-1) had the transistor in a common emitter configuration. Figure 5-2 shows the noise present on the output of the X3 multiplier, which is a frequency multiplication of 192 times the master oscillator. The amplitude of the noise falls off approximately inversely with frequency. The peak noise amplitude is about 36 db below the signal level. This circuit was changed to a common base type (Figure 5-1b). Figure 5-2b shows the same X3 output with the new master oscillator. The gain setting of the spectrum analyzer is the same as in Figure 5-2a. The peak noise is now about 56 db below the signal. Figure 5-2c shows this same noise with more amplification in the spectrum analyzer.

X32 Multiplier. Three new units have been completed and are being tested to evaluate the effort to increase bandwidth and stability. Source impedance for the first doubler has been tentatively changed to 50 ohms so that the unit may be initially tuned and tested over the required range of input frequency, power, and temperature, using a variable frequency source instead of the doubler amplifier that normally drives it. Second and third doubler required only small changes in the strip lines.

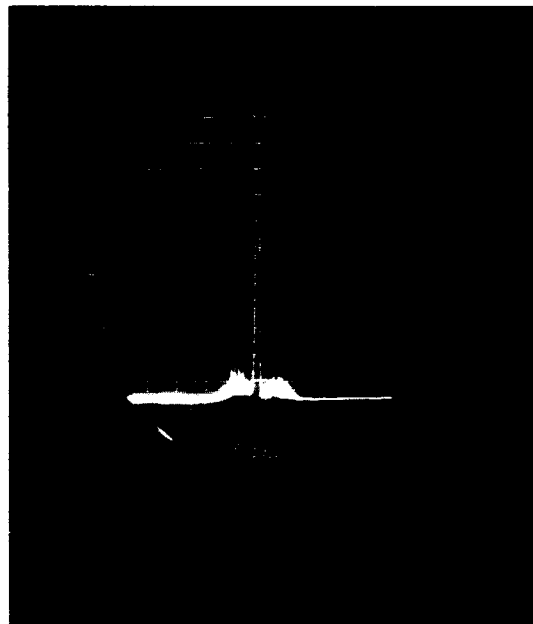
Variable capacitors have been removed from fourth doubler as instability and difficulty of tuning seemed to be associated with these components. Tuning of fourth and fifth doublers is now accomplished by proper selection of input loops and bias voltage. A series variable capacitor has been incorporated in the output coupling circuit of the fifth doubler.



a) Old master oscillator



b) New master oscillator



c) Spectrum analyzer amplified

Figure 5-2. X3 Multiplier Output

Results of tests to date indicate an improvement in bandwidth, stability and ease of tuning.

Frequency Translation Master Oscillator. A breadboard unit has been modified to include a new oscillator circuit. Frequency tolerance on the crystal has been found to be a problem.

Frequency Translation High Level Mixer. The shortened mechanically improved mixers are 99 percent complete.

Receiver Multiplexer. The unit has passed the preliminary specifications tests. In addition tests were performed on adjacent channel cross-talk (Table 5-5), adjacent channel local oscillator coupling test (Table 5-6), and 4 kmc response test. A 4 kmc signal was fed to the receiver multiplier and no output was detected at the four channel outputs.

TABLE 5-5. MUTUAL CROSSTALK BETWEEN ADJACENT CHANNELS

Channel Number	Frequency	Frequency into Proper Channel Through Antenna Terminal	Output at Lower Adjacent Channel, db	Output at Upper Adjacent Channel, db
1	$f_o - 12.5$	6006.8	—	-45.5
	f_o	6019.3	—	-42
	$f_o + 12.5$	6031.8	—	-38
2	$f_o - 12.5$	6095.8	-40	< -50
	f_o	6108.3	< -50	< -50
	$f_o + 12.5$	6120.8	< -50	< -50
3	$f_o - 12.5$	6199.6	38	< -50
	f_o	6212.1	41	< -50
	$f_o + 12.5$	6224.6	44	< -50
4	$f_o - 12.5$	6288.5	35	—
	f_o	6301.0	39	—
	$f_o + 12.5$	6313.5	42	—

TABLE 5-6. ADJACENT CHANNEL LOCAL OSCILLATOR COUPLING

Channel Number	Frequency Translation Local Oscillator	Multiple Access Local Oscillator	Output at Channel 1, db	Output at Channel 2, db	Output at Channel 3, db	Output at Channel 4, db	Output at Antenna, db
1	6081.7		—	(-62)	<-90	<-90	-29
		5989.1	—	(-87)	<-95		-17
2	6171.6		(-95)	—	(-76)	<-95	-31
		6076.6	(-64)	—	<-90	<-90	-16.5
3	6276.5		<-95	(-95)	—	(-62)	-30.5
		6179.9	(-90)	(-73)	—	-90	-18
4	6366.3		<-95	<-95	(-95)	—	-26.5
		6268.4	<-95	(-86)	(-66)	—	14

The output levels enclosed in the rectangle are of primary concern to the system.

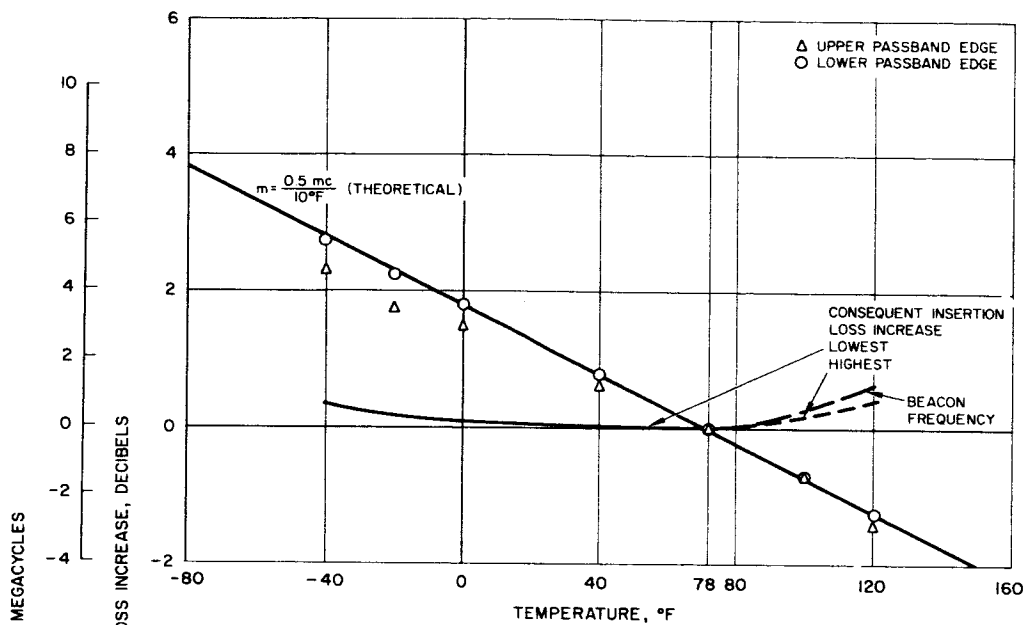
Those encircled all represent tighter coupling than the most tightly coupled values enclosed in the rectangle.

Transmitter Multiplexer. The unit has passed the preliminary specifications tests. In addition tests were performed on adjacent channel crosstalk (Table 5-7) and 6 kmc response as seen in Table 5-8. The unit was also subjected to high power (2.25 watts) operation in a high vacuum (2×10^{-6} mmHg). No change was observed in insertion loss with changing pressure.

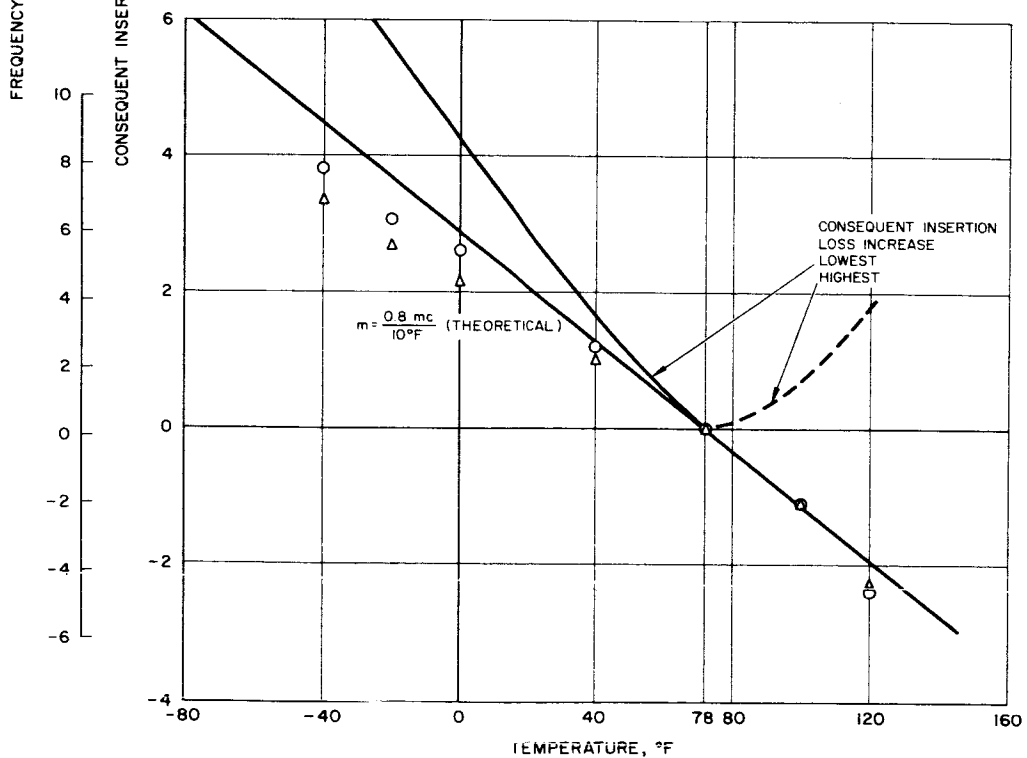
TABLE 5-7. MUTUAL CROSSTALK BETWEEN ADJACENT CHANNELS

Channel Number	Frequency into Proper Channel	Output at Lower Adjacent Channel Input, db	Output at Upper Adjacent Channel Input, db	Beacon Output From Lower Adjacent Channel, db
1	$f_o - 12.5$ (3979.5)	—	< -40	
	f_o (3992.0)	—	< -40	
	$f_o + 12.5$ (4004.5)	—	< -40	
2	$f_o - 12.5$ (4038.5)	< -40	< -40	(4006.9)
	f_o (4051.0)	< -40	< -40	< -40
	$f_o + 12.5$ (4063.5)	< -40	< -40	
3	$f_o - 12.5$ (4107.5)	< -40	< -40	(4066.2)
	f_o (4120.0)	< -40	< -40	< -40
	$f_o + 12.5$ (4132.5)	< -40	< -40	
4	$f_o - 12.5$ (4166.5)	< -40	—	(4135.3)
	f_o (4179.0)	< -40	—	< -40
	$f_o + 12.5$ (4191.5)	< -40	—	

Transmitter-Receiver Multiplexer Temperature Tests. Insertion loss measurements versus temperature at the highest and lowest channel frequencies including the beacon transmit frequency were made on the multiplexers. Figure 5-3 shows the results for transmit and receive channel one.



a) Transmitter multiplexer



b) Receiver multiplexer

Figure 5-3. Temperature Environment Data, Channel 1

TABLE 5-8. TRANSMITTER MULTIPLEXER, 6 KMC RESPONSE
CHANNEL 4*

Frequency of Relative Maximum, mc	Magnitude of Relative Maximum Output Referenced to Input, db
6512	-42
6481	-42
6469	-29
6462	-38
6442	-28
6427	-30
6412	-14
6402	-15
6395	-8
6374	-20
6364	-9
6350	-14
6346	-12
6332	-19
6328	-33
6311	-32
6308	-40
6306	-38
6271	-40
6258	-33
6192	-40
No detectable response below this frequency.	

* Measured from channel 4 input terminal to antenna output terminal, all relative maximum responses were recorded.

Multiple Access Regulator. Satisfactory performance has been obtained on one breadboard regulator at 75°F and -26 volts input. The -24 volt output changed 0.125 percent from no load to full load (150 milliamperes). At 75°F and full load, the -24 volt output changed 0.029 percent from high line input to low line (-30 ± 4 volts). The output changed 0.20 percent from 0°F to 150°F, at full load and low line. The total deviation in -24 volt output was 0.41 percent for $0 \leq I_O \leq 150$ milliamperes, $-34 \leq V_{in} \leq -26$ volts, and $0^\circ \leq T \leq 150^\circ\text{F}$. The above results represent the static load, line, and temperature regulation. Rated load was applied and removed as a step function, and the transient response was observed. Excursions of 250 millivolts in output voltage were observed, returning to steady-state with a well damped response. From no load to full load, the damping time was on the order of 150 μsec for $0^\circ < T < 150^\circ\text{F}$. From full load to no load, the damping time was approximately 1.4 msec. The load transient response was relatively independent of input voltage for $V_{in} = -30 \pm 4$ volts. The maximum PARD measurement was 14 millivolts peak-to-peak, over the entire line, load, and temperature ranges considered. The overcurrent trip level was somewhat sensitive to input voltage. A change in input from -28 to -34 volts increased the overcurrent limit by 40 percent of rated current. Figures 5-4 through 5-6 show the results of the tests.

APQ Regulator. Satisfactory performance has been obtained on one breadboard regulator at 75°F and -26 volts input. The -24 volt output changed 0.68 percent from no load to full load (1.25 amperes). At 75°F and full load, the -24 volt output changed 0.16 percent from high line input to low line (-30 ± 4 volts). The output changed 0.54 percent from 0°F to 150°F, at full load and low line. The total deviation in -24 volt output was 1.24 percent for $0 \leq I_O \leq 1.25$ amperes, $-34 \leq V_{in} \leq -26$ volts, and $0^\circ \leq T \leq 150^\circ\text{F}$. The above results represent the static load, line, and temperature regulation. Rated load was applied and removed as a step function, and the transient response was observed. One volt excursions in output voltage were observed, returning to steady-state with a well damped response. From no load to full load, the damping time was on the order of 300 μsec for $75^\circ\text{F} < T < 150^\circ\text{F}$, increasing to 500 μsec at 0°F. From full load to no load, the damping time was approximately 6 μsec . The load transient response was relatively independent of input voltage for $V_{in} = -30 \pm 4$ volts. The maximum PARD measurement was 13 millivolts peak-to-peak, over the entire line, load, and temperature ranges considered. The overcurrent trip level was somewhat sensitive to input voltage. A change in input from -26 to -34 volts increased the overcurrent limit by 40 percent of rated current. Figures 5-7 and 5-8 show the results of these tests.

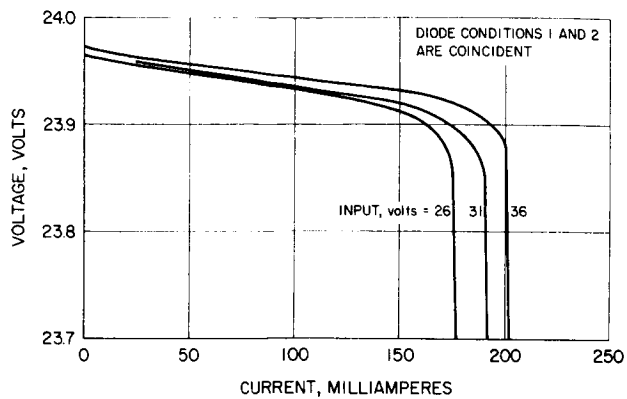


Figure 5-4. Voltage versus Current at 0°F

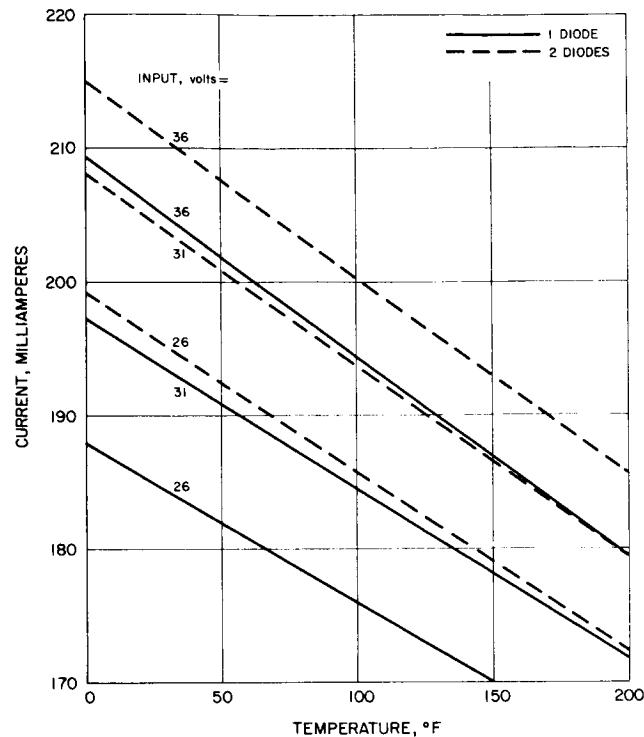


Figure 5-5. Current versus Temperature at -22 Volts

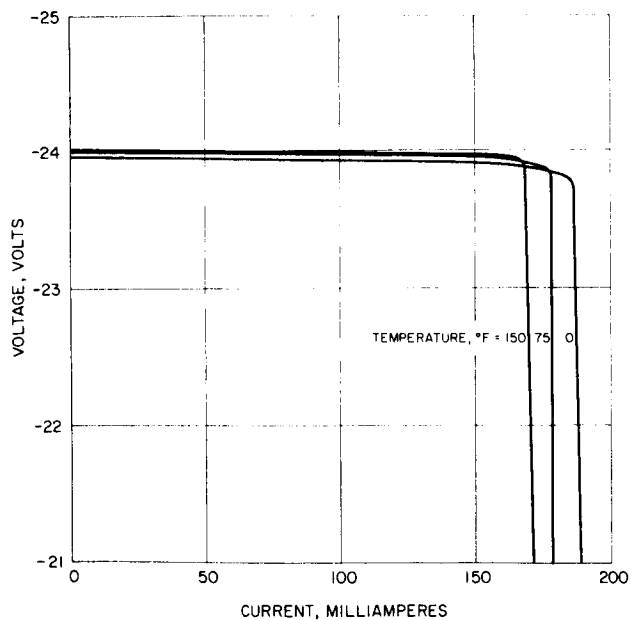


Figure 5-6. Temperature Regulation at $V_{iN} = 26$, Output Voltage versus Load Current

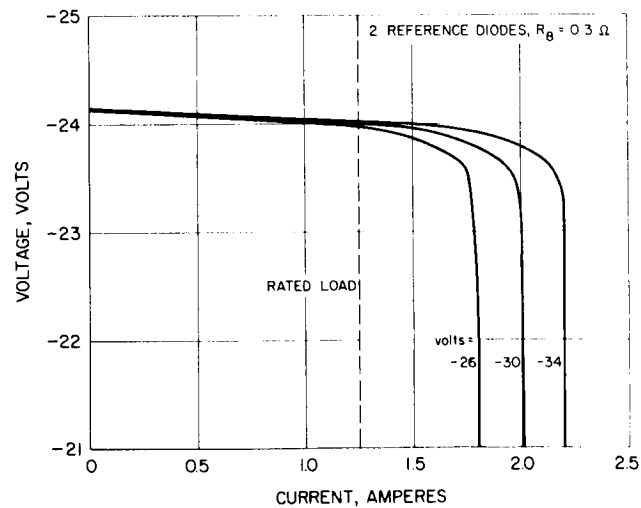
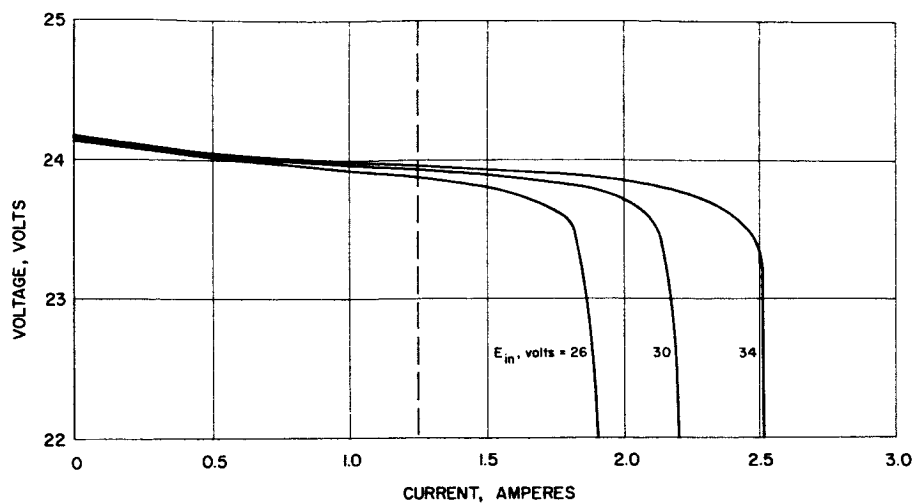
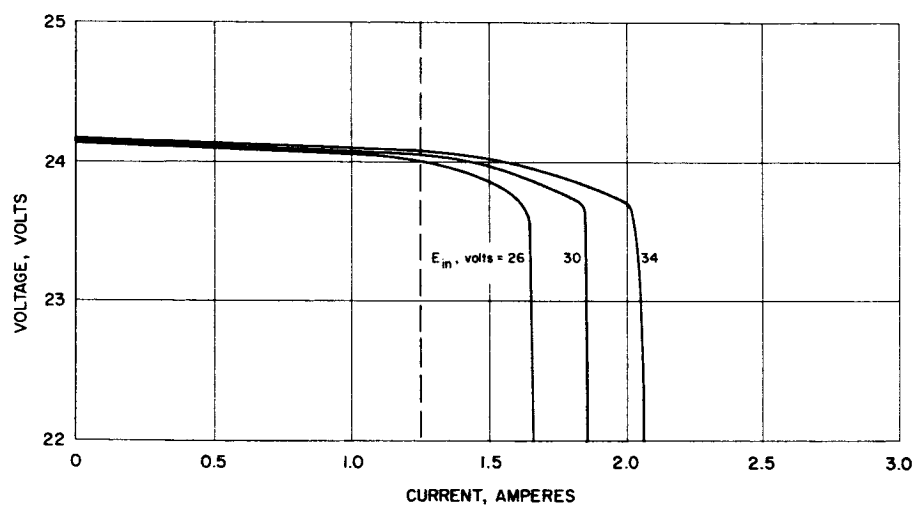


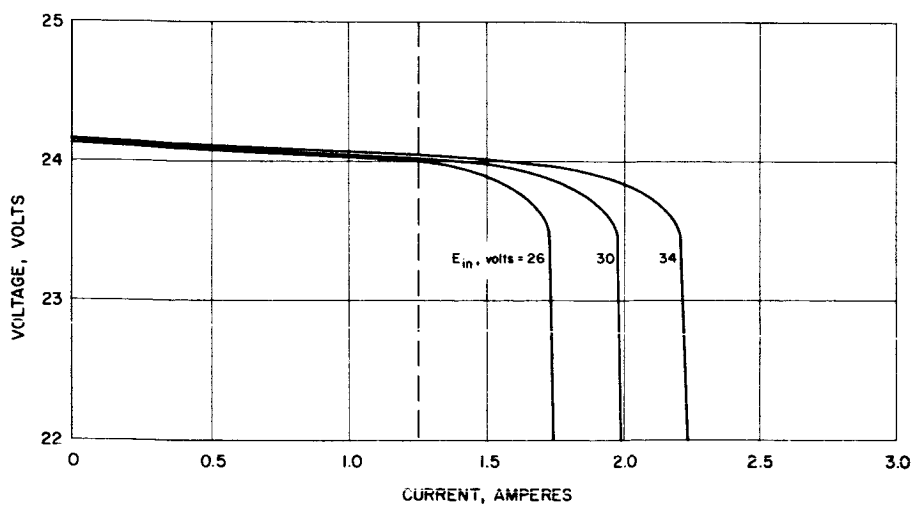
Figure 5-7. Voltage versus Current at 75°F



a) 0°F



b) 100°F



c) 150°F

Figure 5-8. Current versus Temperature
2 reference diodes, $R_g = 0.3 \Omega$

Traveling-Wave Tube Power Amplifier

General Status Discussion

During this period, the major effort was directed toward the design and construction of experimental vehicles for the proposed study plan, but the regular monitoring of the twelve life test tubes continued. The irregularities observed last period in the performance of tube No. 384H-40 when it was operated with the dc to dc converter was completely investigated.

To initiate the experimental phase of the proposed study plan, several experimental devices were constructed and others have been planned. Many of the vehicles are currently in test and some of the results are being evaluated. In relation to the study plan, these test vehicles will be used as indicated in Table 5-9.

TABLE 5-9. STATUS OF CURRENT TRAVELING-WAVE
TUBE EXPERIMENTS

General Area of Investigation	Specific Study	Test Vehicle	Status of Vehicle
Reduction of beam voltage sensitivity	Reduction of cold circuit loss	384H with copper- plated helix	In test
	Reduction of dielectric loading	384H with special support rods	Will be con- structed next month
	Horn match	Cold test fixture	In test
	Reduce barrel to helix ratio	Special tube	Designed
Periodic variations in helix current	Charging of ceramic helix support rods	Special 384H	In test
Performance deg- radation after packaging	Window radiation	Different output window	Design is being studied

Last period the company held a partial discussion of the irregularity in traveling-wave tube performance while operating with the dc to dc converter. This irregularity is shown in Figure 5-9. The curve labeled normal operation is the characteristic obtained when the traveling-wave tube is operated with a laboratory power supply. The other curve illustrates

the discontinuity obtained when using the converter. However, as shown for drive levels from 0.2 to 0.8 milliwatt, no apparent difference was observed. This irregularity was caused by a change in converter helix cathode voltage (Figure 5-10), as the input drive to the traveling-wave tube was varied. Figure 5-10 illustrates this characteristic of the converter. Figures 5-11 and 5-12 show the variation of anode and collector voltage as the drive is changed. These variations in converter output voltages are probably caused by the variation in helix and collector current with drive. This is shown in Figure 5-13 which was obtained with the laboratory power supply. Several other 384H tubes have been examined to obtain a helix current versus drive characteristic and it appears that the general shape of Figure 5-13 is typical. Since the helix to cathode potential is the most critical of the traveling-wave tube voltages, the converter variation of this voltage is the major cause of the irregularity shown in Figure 5-9 and the other voltage variation probably adds a secondary effect.

Life Improvement Program

The life test tubes are performing normally and no degradation of performance has been observed. Life test data of these tubes in accordance with the test plan is being continually submitted to GSFC.

Telemetry and Command

Telemetry Format

A preliminary investigation of the number of telemetry channels required for various configurations of the Advanced Syncom spacecraft has been completed. This study does not include the requirements of the radiation package. The following preliminary parameters were used in determining telemetry channel requirements:

- 1) A long telemetry channel consists of eight consecutive channels.
- 2) Binary data is encoded at 4 bits per channel.

<u>Package</u>	<u>Telemetry Channels Required</u>	<u>Sub- total</u>	<u>Totals</u>
Configuration I - Spin Stabilized Spacecraft:			
Power supply (6 plus 2 long)	22		
Spacecraft identification	1		
Temperature	7		
Command subsystem	8		
Transponder 1	1		
Telemetry	6	45	

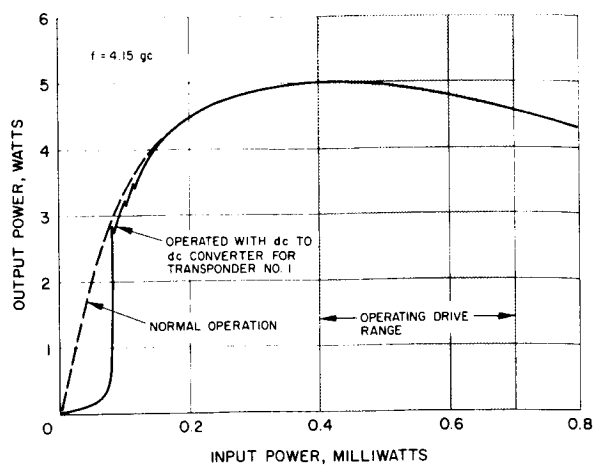


Figure 5-9. Output Power versus Traveling-Wave Tube Drive

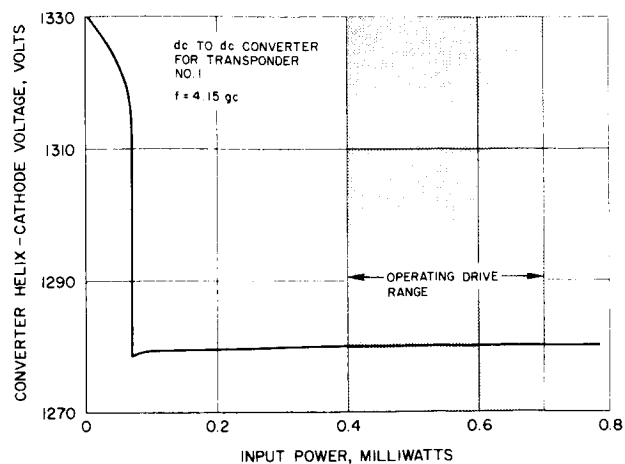


Figure 5-10. Converter Helix-Cathode Voltage versus Traveling-Wave Tube Drive

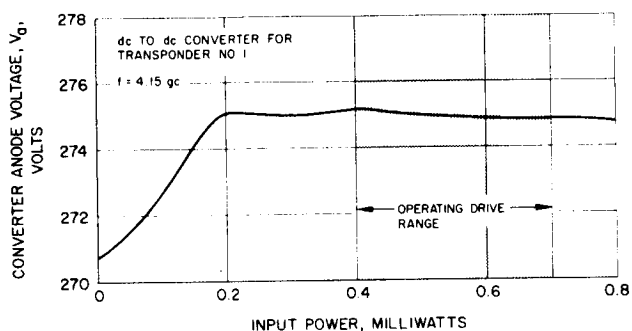


Figure 5-11. Converter Anode Voltage versus Traveling-Wave Tube Drive

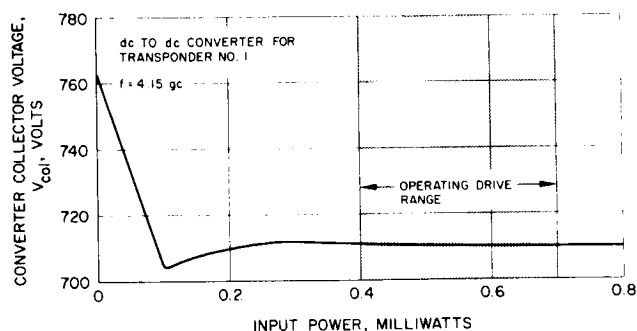


Figure 5-12. Converter Collector Voltage versus Traveling-Wave Tube Drive

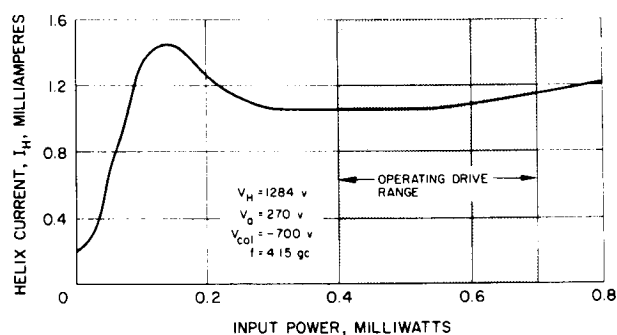


Figure 5-13. Helix Current versus Traveling-Wave Tube Drive

<u>Package</u>	<u>Telemetry Channels Required</u>	<u>Sub- total</u>	<u>Totals</u>
PACE	3		
Transponder (long channel)	8		
ψ_2	3		
H ₂ O ₂	4		
		18	
Meteorological		28	
Engineering experiment		<u>20</u>	
			111
Configuration 2 - 6000 Gravity-Gradient			
Spacecraft:			
Power supply	6		
Spacecraft identification	1		
Temperature	7		
Command	8		
Transponder	2		
Telemetry	6		
		30	
RCS			
H ₂ O ₂	4		
Subliming solid	4		
		8	
Meteorological		28	
Nuclear arms (estimated)		10	
Engineering experiment		20	
Gravity-gradient		<u>25</u>	
			121
Configuration 3 - Spin Stabilized (Mechanical Antenna)			
Spacecraft:			
Power supply (6 plus 2 long)	22		
Spacecraft identification	1		
Temperature	7		
Command	8		
Transponder	1		
Telemetry	6		
		45	
Transponder (1 long)	6		
ψ_2	3		
H ₂ O ₂	4		
		13	

<u>Package</u>	<u>Telemetry Channels Required</u>	<u>Sub- total</u>	<u>Totals</u>
Mechanical antenna		3	
Department of Defense		10	
Communications Satellite Corporation		<u>10</u>	
			81
Configuration 4 - SAGGE			
Spacecraft:			
Power supply	6		
Spacecraft identification	1		
Temperature	7		
Command subsystem	8		
Transponder	2		
Telemetry	6		
		30	
RCS:			
H ₂ O ₂	4		
Subliming solid	4		
		8	
Meteorological		28	
Gravity-gradient		<u>25</u>	
			71
Configuration 5 - SAGGE			
Spacecraft:			
Power supply	6		
Spacecraft identification	1		
Temperature	7		
Command subsystem	8		
Transponder	2		
Telemetry	6		
		30	
RCS:			
H ₂ O ₂	4		
Subliming solid	4		
		8	
RF propagation		10 (estimate)	
Nuclear arms control		10 (estimate)	
Gravity-gradient		<u>25</u>	
			83

Telemetry Encoder Status

Telemetry Encoder Circuit Design. During December the final design review for the telemetry encoder was held with NASA-GSFC personnel participating. The design review minutes are included as an appendix to this section.

Fabrication and checkout of the breadboard encoder was completed during December. Figure 5-14 shows the breadboard being tested, and Figure 5-15 is a closeup of the encoder breadboard. Since metal film resistors were not available for breadboard fabrication, carbon film resistors were used instead. Therefore, it will not be possible to evaluate encoder accuracy over the operating temperature range; however, the encoder will be tested for qualitative operation over a temperature range. The flip-flop circuits will be subjected to valid noise tests since these circuits use no precision components and have been fabricated with the components specified. Encoder accuracy over temperature will be evaluated for the welded engineering model.

Two changes have been made to the encoder circuits since the design review. In the data level limiter circuit, the zero-clamp reference level is now obtained from a resistor divider between ground and +7 volts, instead of ground as before. This was necessary to provide for initial mismatch between diode and base-emitter forward voltages. The coupling between the first and second stages of the execute tone modulator has been changed to ac coupling. This was necessary to improve the symmetry of the square-wave signal applied to the filter, thereby improving the amplitude stability of the transponded execute tone. Neither of these changes will appear in the engineering model. However, the encoder breadboard will be updated and the changes fully evaluated.

Telemetry Encoder Circuit Design Review. The telemetry encoder subsystem and circuit design was reviewed on 29 December with NASA-GSFC representatives participating.

Product Design of Telemetry Encoder Engineering Model (Welded Modules). During this period, 15 of the 16 welded module types were pre-released. It now appears that the encoder will require two etched circuit boards rather than 1 3/4 as earlier estimated. Design has been initiated on the two etched boards.

Fabrication of Welded Module Encoder. All purchase requisitions have been written, and fabrication of the encoder has begun. Of the 28 total modules required, 24 component holders were fabricated and 5 modules welded and delivered to checkout during December. Three modules of one type have been tested (Flip-Flop and Interstage Gates). No errors were found in any of the three.

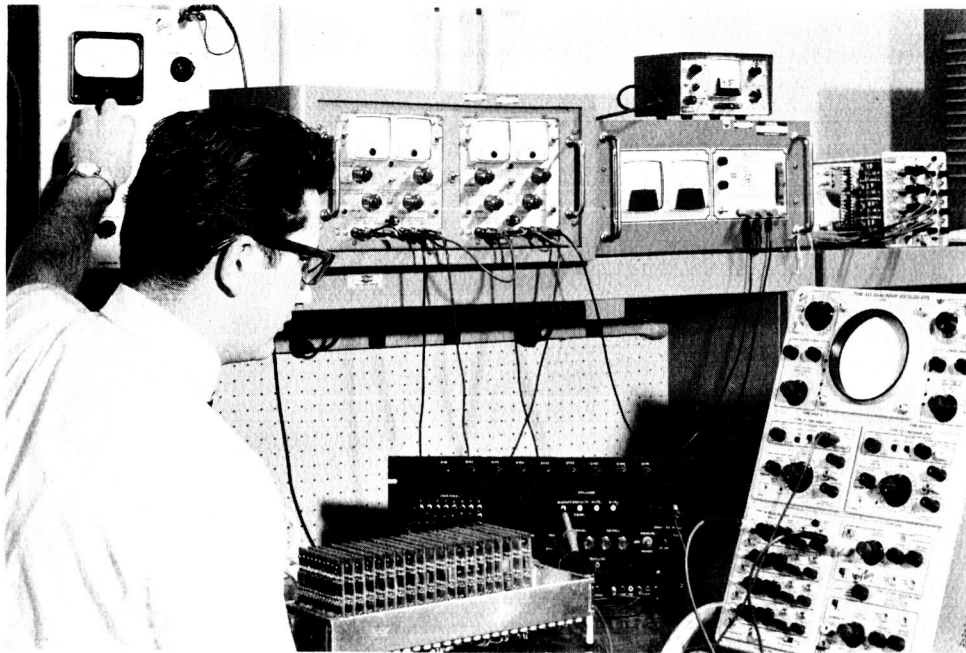


Figure 5-14. Telemetry Encoder Breadboard Under Test

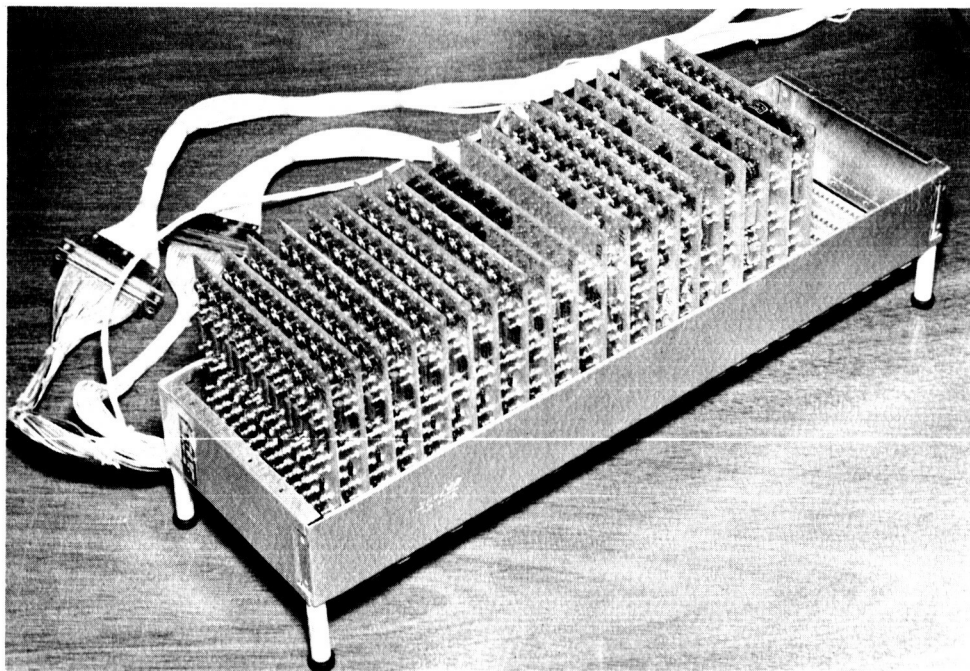
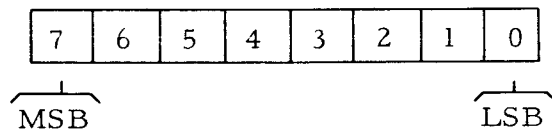


Figure 5-15. Telemetry Encoder Breadboard

Command Format

The command system for Advanced Syncom will be an NRZ FSK system similar to the OGO command system. The system will operate on an RF frequency of 148.260 mc and will use modulation frequencies of 7400 and 8600 cps for tones of zeros and ones, respectively, and 3620 cps for the execute tone. Real time execute will be incorporated in the system. The system will be implemented so if a zeros tone is received continuously the execute channel will be held inoperative. The command register will be implemented so that any accumulation of bits will be cleared every 315 minutes by the local quadrant central timer. In addition, if a correct command is received during the zeros tone transmission normally applied, the decoder will ignore it, that is, not turn off. The decoder will turn off if the zeros tone transmission is interrupted for at least 10 milliseconds then followed by a 150 millisecond zeros or ones tone transmission. The format for the Advanced Syncom commands consists of three major subdivisions: 1) Word Sync, 2) Address, and 3) Command. An 8-bit system will be used in both the address and the command. The message format is described in the following paragraphs:

- 1) Word Sync. The Word Sync is used to define the start time for command which follows. Word Sync will be a series of zeros followed by a one and a zero.
- 2) Address. The second 8 bits of the command message will address a spacecraft and the command system in a particular quadrant. The format is defined as follows:



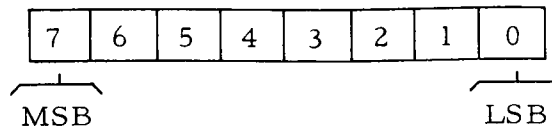
where

- a) Bit Nos 2, 3, 4, and 5, 6, 7 define two octal numbers which are the spacecraft numbers.
- b) Bit Nos 0 and 1 are the quadrant numbers.

Using this format allows the capability of addressing a maximum of 256 quadrants.

- 3) Command. The second group of eight bits defines the command to be performed. The command word is as follows:
 - a) Bits 0, 1, 2, and 3, 4, 5 define two octal numbers which represent the command.

- b) Bits 6 and 7 address one of the four matrices within a decoder.



- 4) Format. A sample command/address in modified octal form would be

022-640

In digital form this would be

00001010-11010000

The command would be interpreted to mean:

- a) It is addressed to spacecraft 2, quadrant 3.
- b) It is command 64 and will use matrix one in the command decoder located in quadrant 3.

Command Decoder Status

Breadboard Status. The command decoder breadboard has been brought up to date. The final circuits have been evaluated as integral parts of the breadboard and they work in a satisfactory manner. The equipment which will be used to complete the evaluation of the decoder is in the process of being completed.

Command Decoder Output Interface. A minor change in the output configuration of the diode matrix is being considered which should eliminate parts and increase the efficiency of the matrix with regard to output current available.

Structure

Structure Engineering Design and Arrangement of Basic Equipment Complement

The T-2 model structure has been investigated to determine its capability to serve as a general purpose vehicle. It has more than adequate space and flexibility to accommodate the required payload complement.

Structural Modifications

Integration of payloads to the vehicle has required few noteworthy structural changes. Revised reaction control system tanks allowed the ribs to be relocated symmetrically. The thrust tube may be reworked to move the apogee motor aft to improve the roll-to-pitch ratio. Improved quadrant package mounts are being designed to accommodate the experimental payloads. Cutouts will be provided in the thrust tube for boom mechanisms where required.

Basic Equipment Reaction Control Subsystem

Three similar tankage arrangements are used for the reaction control subsystem depending on the mission. Several tank configurations were studied and spherical tanks were chosen for the following reasons:

- 1) The variety and quantities of propellant do not lend themselves to packaging in efficiently shaped toroidal tanks.
- 2) The tank walls are sized by manufacturing limitations rather than pressure and the additional surface area of the torus configuration constitutes a weight penalty.
- 3) The vehicle is not as space limited as anticipated and the tank requirements are smaller than T-2; therefore the increased volume afforded by toroidal tanks is not required.
- 4) Repackaging of some units such as the Hughes Transponder would be necessary if toroidal tanks were employed.
- 5) Installation of the gravity-gradient boom mechanisms with toroidal tanks is difficult.

Electronics

Some of the rib-mounted units have been rearranged to provide clearance for the cold gas spinup tanks and the gravity-gradient cameras. The quadrant electronics package has remained unchanged.

Antenna

The phased array antenna package from T-2 has remained unchanged except that multiplexers have been removed as no longer needed. This space under the cruciform has been reserved for the apogee motor if it is moved aft to improve the roll-to-pitch ratio. Alternate antenna packages have not been studied as little information is available at the present time.

Solar Panels

T-2 model solar panels and mountings are adequate for the spin-stabilized version. The high temperatures, additional cutouts, and boom shadowing effects on the gravity-gradient configurations have necessitated investigation of increased solar panel area for these vehicles. Two extendible solar panel configurations under investigation are shown in Figure 5-16. They both offer approximately a 50 percent increase in solar panel area. The concave panels have the same power as the conventional panels and some thermal control may be utilized on the back side of both configurations to reduce operating temperature and improve efficiency.

Power requirements have not been finalized and these configurations are offered only to indicate possible solutions if additional power is required.

Agena Adapter

The main effort of the report period was the refinement of the non-spinning Advanced Syncom-to-Agena adapter. The configuration is shown in Figure 5-17, and was described in the November report.

Agena Adapter - Structural Analysis and Dynamics

The lateral deflection of the elastic axis is defined as χ (Figure 5-18), and the rotation of the cross section plane at the free end is defined as θ . The forces on the cone may be related to the deflections of the cone by the following equations:

$$\begin{aligned} \chi &= a_{11} P + a_{12} M \\ \theta &= a_{21} P + a_{22} M \end{aligned} \quad \text{or, in matrix form} \quad \begin{bmatrix} \chi \\ \theta \end{bmatrix} = \begin{bmatrix} a_{11} & a_{12} \\ a_{21} & a_{22} \end{bmatrix} \begin{bmatrix} P \\ M \end{bmatrix} \quad (5-1)$$

where the a_{ij} are influence coefficients.

Assuming only membrane forces in the conical shell, a free body diagram of an element is shown in Figure 5-19. The stresses are as follows:

$$N_{\phi} = 0 \quad (5-2)$$

$$N_y = \frac{P \cos \phi}{\pi \sin^2 \alpha} \left(\frac{y_o}{y^2} - \frac{1}{y} \right) - \frac{M \cos \phi}{\pi y^2 \sin^2 \alpha \cos \alpha} \quad (5-3)$$

$$N_{y\phi} = \frac{(Pl - M) \sin \phi}{\pi y^2 \sin \alpha \cos \alpha} \quad (5-4)$$

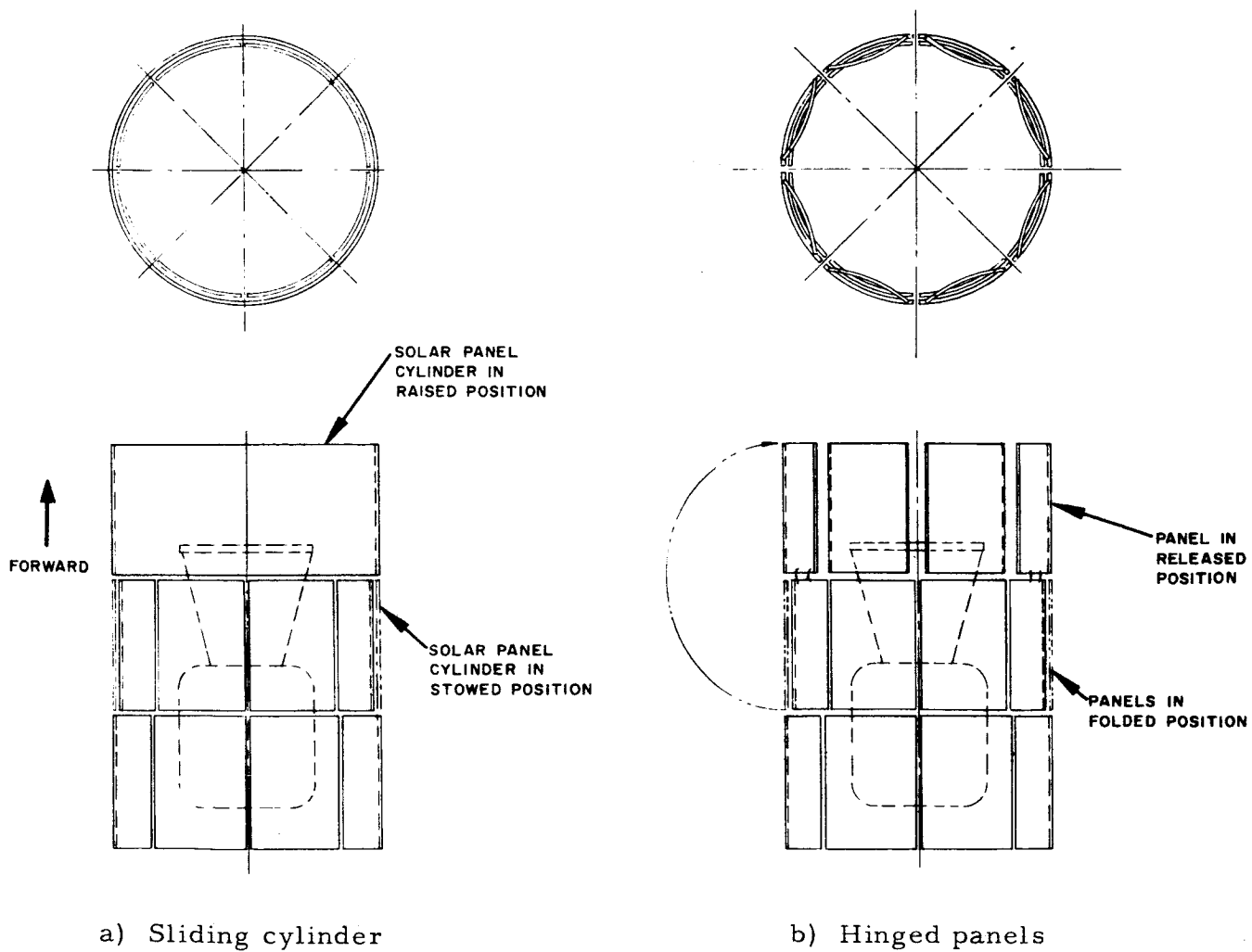


Figure 5-16. Proposed Method of Increasing Solar Panel Area

The influence coefficients may be expressed in terms of strain energy U, by Castigliano's theorem, as follows:

$$\begin{aligned} P a_{11} &= \left. \frac{\partial U}{\partial P} \right]_{\substack{M=0 \\ P=0}} & P a_{21} &= \left. \frac{\partial U}{\partial M} \right]_{\substack{M=0 \\ P=0}} \\ M a_{12} &= \left. \frac{\partial U}{\partial R} \right]_{\substack{M=0 \\ P=0}} & M a_{22} &= \left. \frac{\partial U}{\partial M} \right]_{\substack{M=0 \\ P=0}} \end{aligned} \quad (5-5)$$

The strain energy in terms of stress, as follows:

$$U = \int_0^{2\pi} \int_{y_0}^{y_1} \frac{1}{Et} \left[N_y^2 + \frac{E}{G} N_{y\phi} \right] y \sin \alpha \, d\phi \, dy \quad (5-6)$$

Performing the indicated operations by Equations 5-5 and 5-6, the influence coefficients may be written as functions of R and L. Letting

$$Z = \frac{y_0}{y} = \left(1 - \frac{\tan \alpha}{\frac{R}{L}} \right),$$

the influence coefficients become:

$$a_{11} = \frac{1}{Et \pi \sin^3 \alpha} \left[-1.5 - \frac{Z^2}{2} + 2Z + \ln \frac{1}{Z} \right] + \frac{1}{Gt \pi \sin \alpha} [1 - Z^2] \quad (5-7)$$

$$\begin{aligned} a_{12} = a_{21} &= \frac{1}{Et R \pi \sin^3 \alpha \cot \alpha} \left[\frac{1}{2Z} + \frac{Z}{2} - 1 \right] \\ &\quad - \frac{\sin \alpha}{Gt \pi R \cos^2 \alpha} \left[\frac{1}{Z} - Z \right] \end{aligned} \quad (5-8)$$

$$a_{22} = \frac{1}{2Et R^2 \pi \sin^3 \alpha \cot^2 \alpha} \left[\frac{1}{Z^2} - 1 \right] + \frac{\sin \alpha}{Gt \pi R^3 \cos^2 \alpha} \left[\frac{1}{Z^2} - 1 \right] \quad (5-9)$$

E = modulus of elasticity
G = modulus of rigidity

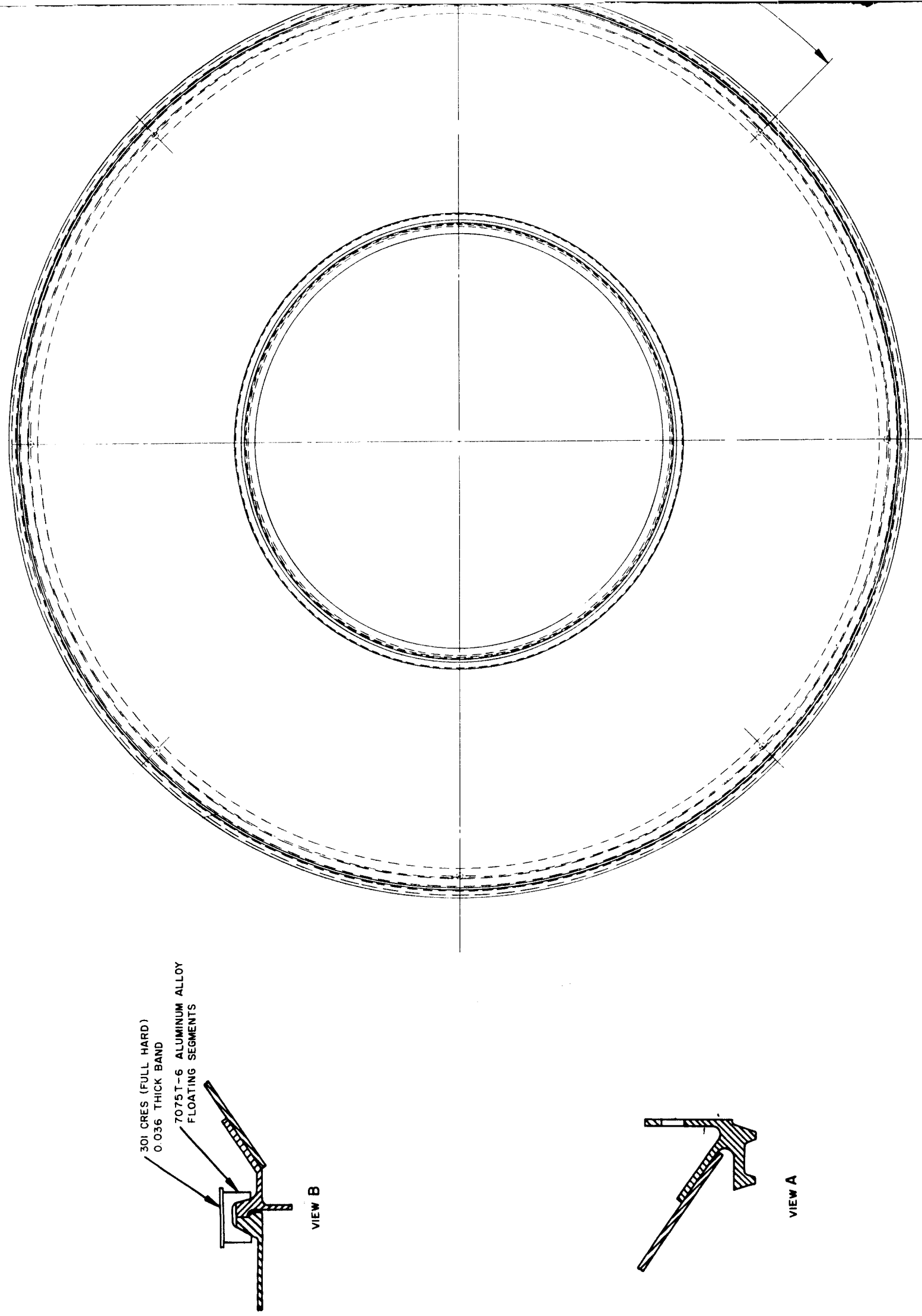
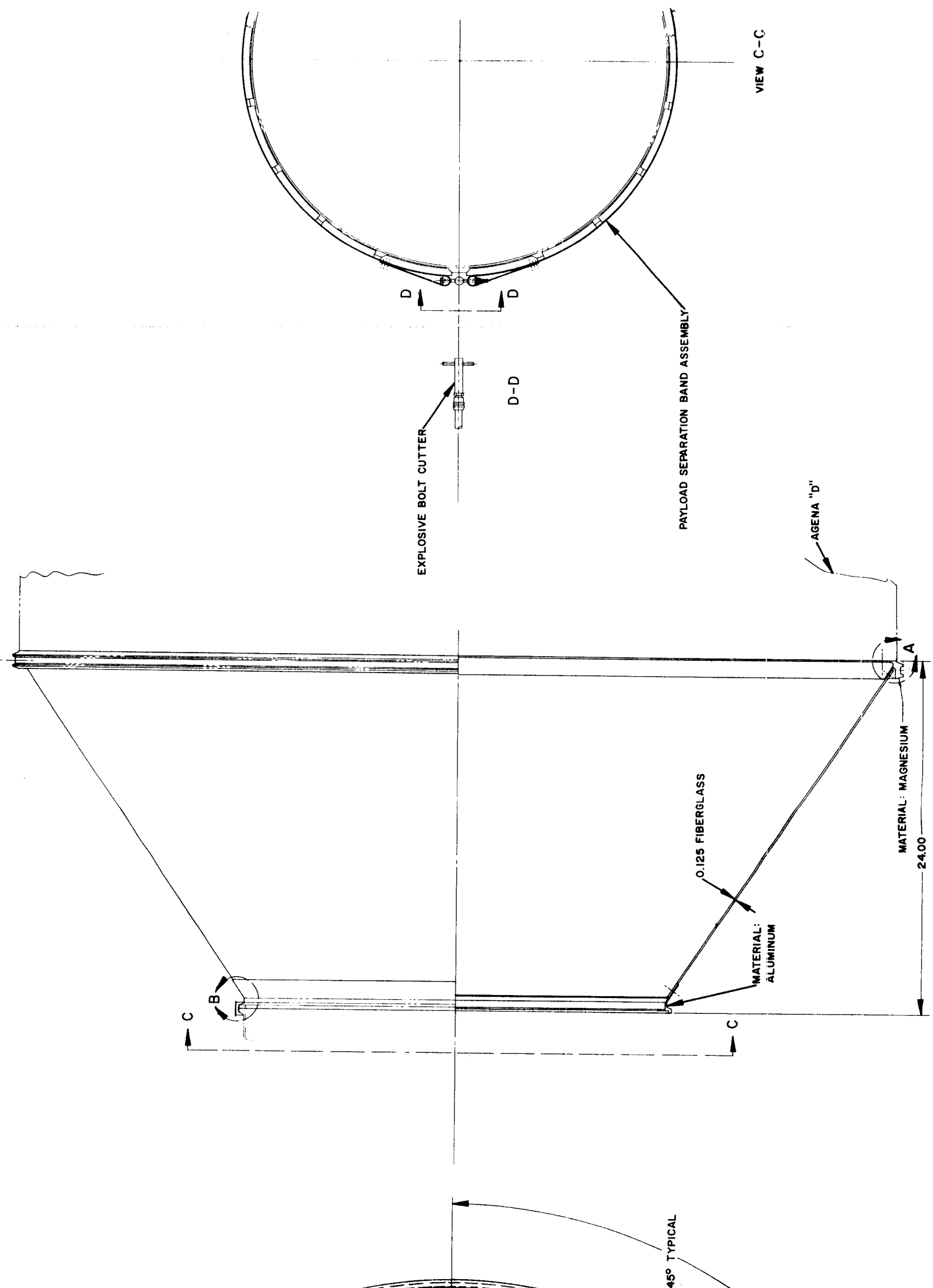


Figure 5-17. Proposed Interstage for Free-Body Spinup



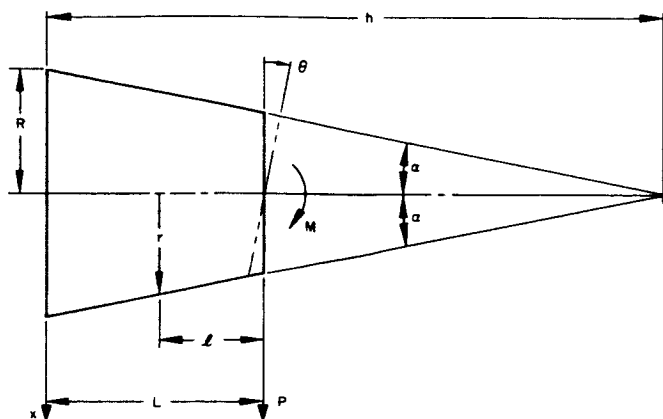


Figure 5-18. Shell Truncated Cone

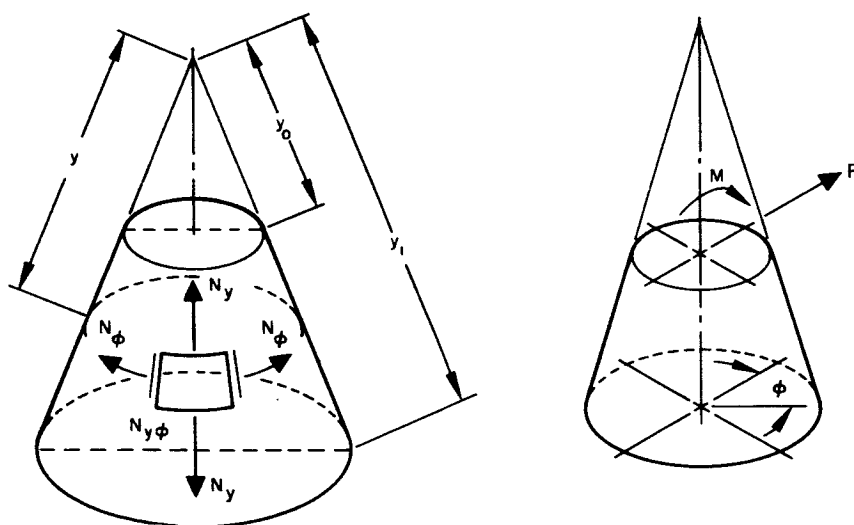


Figure 5-19. Unit Stresses and Applied Loads

Using the geometric parameters shown on Drawing No. X209694 and assuming $E = 2.5 \times 10^6$ psi, $G = 0.550 \times 10^6$ psi, and a thickness of 0.125 inch

$$a_{11} = 6.79 \times 10^{-6}$$

$$a_{12} = -1.704 \times 10^{-7}$$

$$a_{21} = -1.704 \times 10^{-7}$$

$$a_{22} = 1.965 \times 10^{-8}$$

Phased Array Antenna

Antenna Matching

Study of the problem of matching the elements in the antenna array was continued, using the basic three quarter-wave sections. Results were borderline regarding bandwidth, center frequency, and voltage standing wave ratio (VSWR). Figure 5-20 shows a plot of VSWR versus frequency for one antenna. The VSWR could not be maintained less than 1.5 over the desired 220 mc band. The alignment procedure was touchy and could not always be repeated.

Since the first satellites will probably not use the full 4-channel bandwidth, it was decided to match the antennas over a 100 mc band from 4100 to 4200 mc to cover the two higher channels. This was easily done using only two quarter wave sections. The resulting VSWR versus frequency for all 16 antennas measured in the array is shown in Figure 5-21. As with the three sections, the higher frequency end caused the most trouble.

Using these sixteen antennas, the gain of the array relative to a standard horn was measured in the laboratory. The results of these measurements is shown in Figure 5-22. The spin modulation was less than 1 db and the gain was above 14 db from 4080 to 4190 mc.

A single phase shifter using stripline circuits identical to parts of the array was assembled and tested. Some of the results are plotted in Figures 5-23 through 5-26. The insertion loss was less than 1 db, and the VSWR was less than 1.3 at all terminals with a small variation in frequency. Parts of this unit will now be used to check the operation of the phased array stripline.

The new phase shifters using the low voltage field winding are undergoing final shop assembly and should be ready for installation in the array in early January.

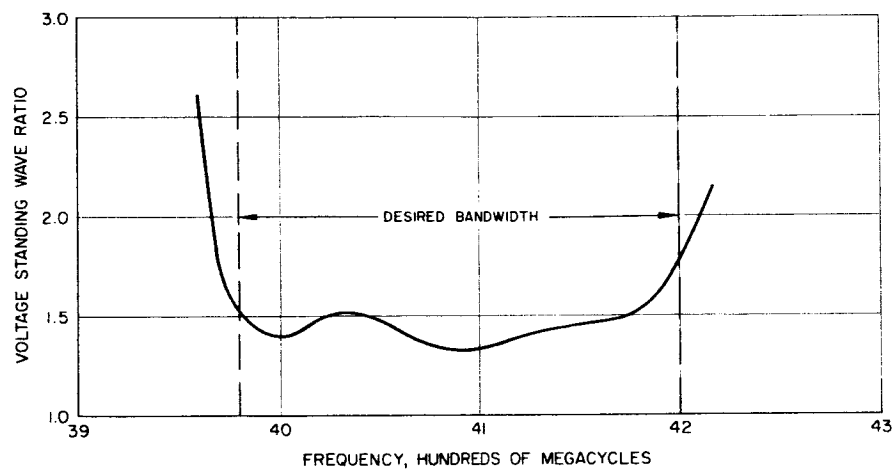


Figure 5-20. Antenna Input Measured in Array
3 section matching

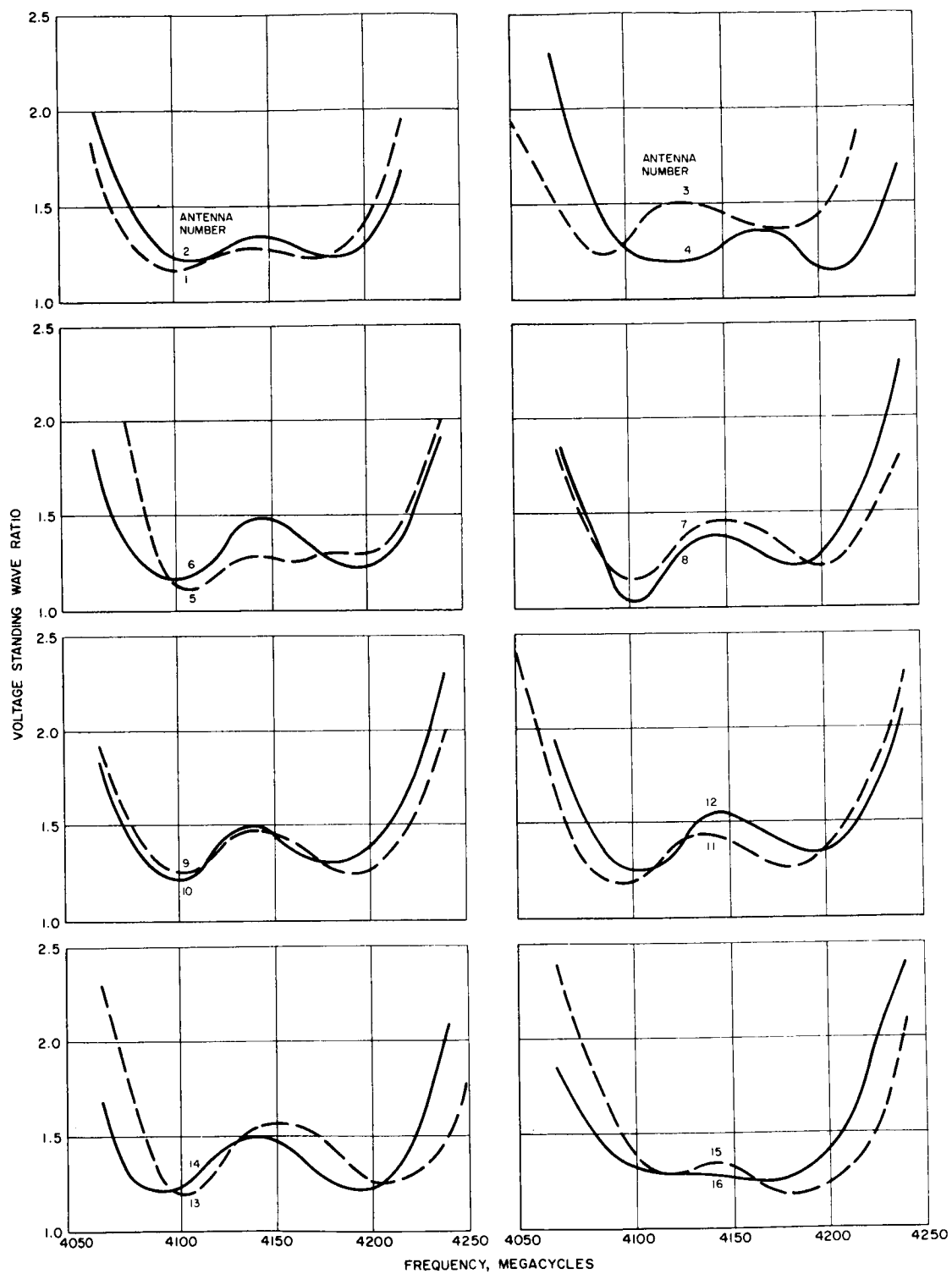


Figure 5-21. Antenna Input VSWR Measured in 16-Element Array

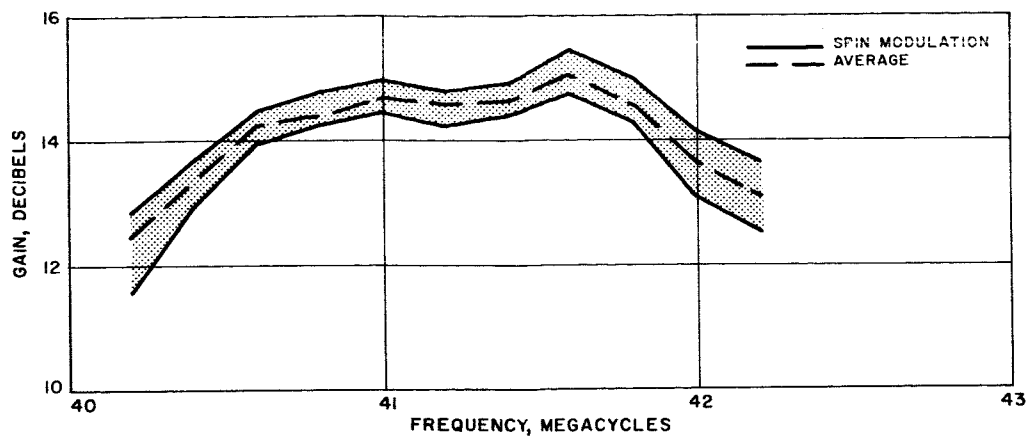


Figure 5-22. Phased Array Gain versus Frequency

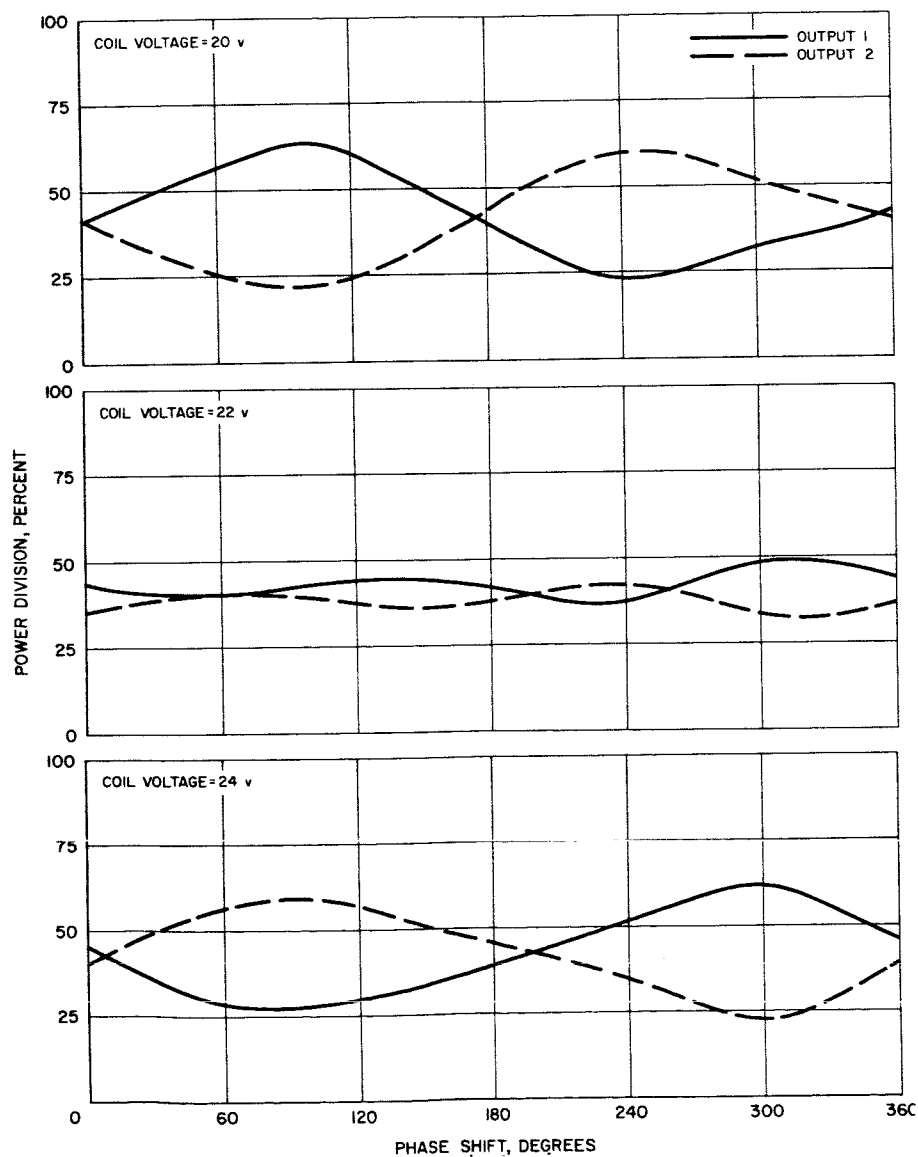


Figure 5-23. Power Division versus Phase Shift

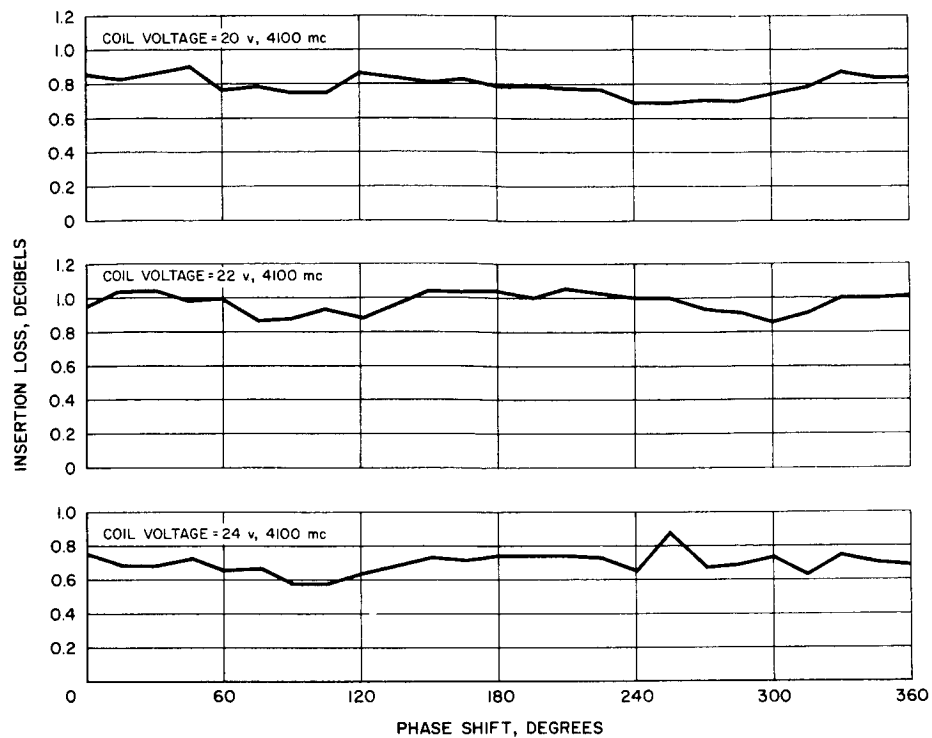


Figure 5-24. Insertion Loss versus Phase Shift

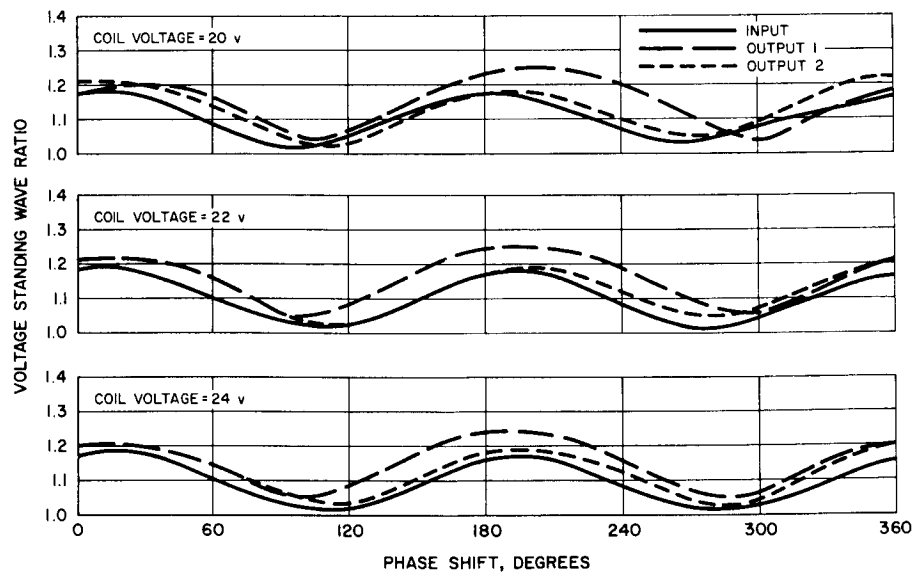


Figure 5-25. VSWR versus Phase Shift

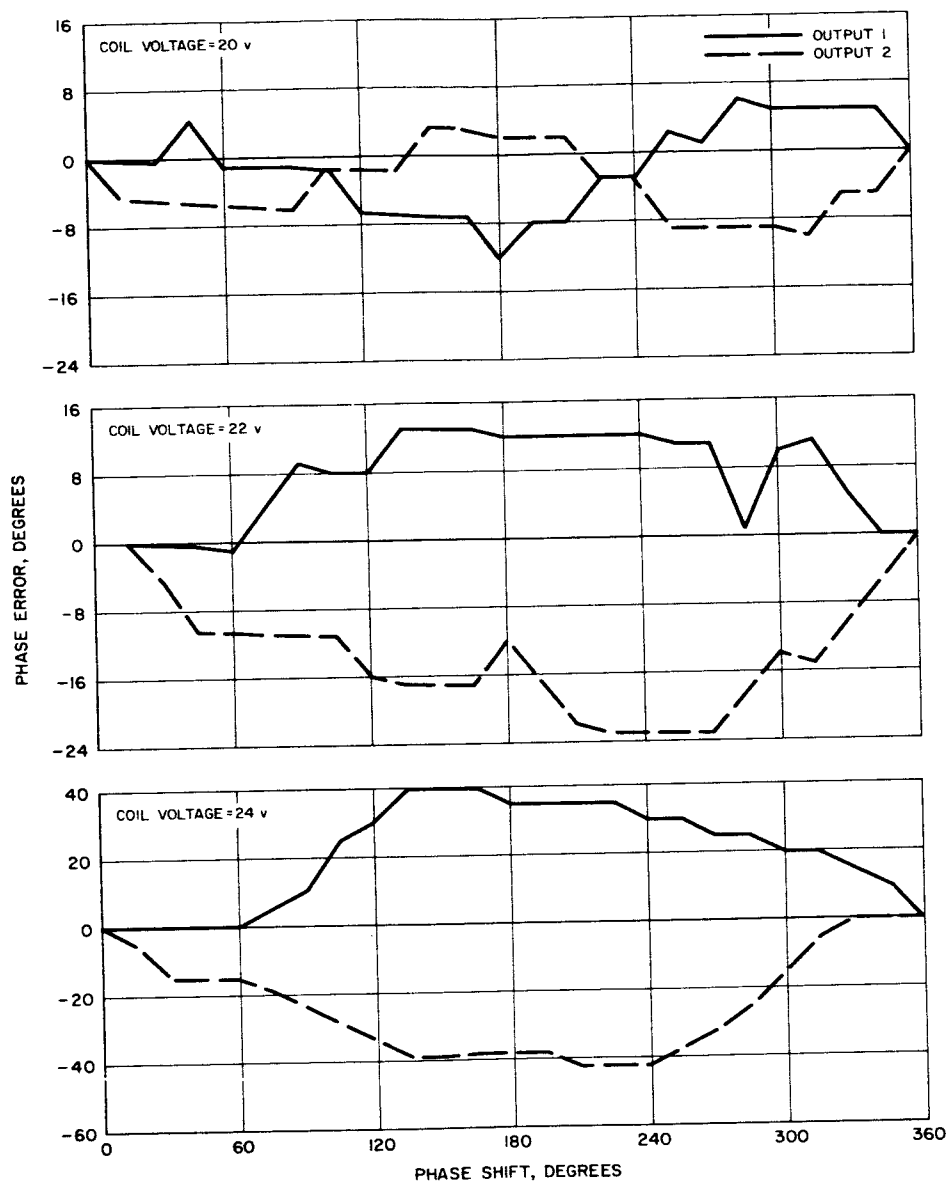


Figure 5-26. Phase Error versus Phase Shift

A set of vertical antenna patterns for a single element of the array were taken at different frequencies and the results plotted in Figure 5-27. Beamwidth was satisfactory and beam tilt with frequency was negligible. The optimum frequency seemed to be about 4080 mc. The pattern gain at 4080 mc was found to be 8.0 db.

Phased Array Control Electronics

PACE Status

The life test of the Advanced Engineering Model (AEM) has been continued through the entire report period. The Advanced Development Model (ADM) was life tested in the early part of the month, but the test was interrupted to make some minor modifications to the unit tester and to rework the waveform generator function board.

The purpose of the rework was to incorporate design changes into the waveform generator which would bring it up to the latest configuration. This required modifying eight of the existing modules (generators 1 and 11) and replacing one module with a newly fabricated one (the generator auxiliary supply).

The reworked modules were retested and then replaced on the function board. The board was then integrated with the other portions of the PACE. Although the ADM has not been tested with the antenna, the waveforms now appear to be satisfactory and no problems are anticipated. The function boards are now ready to be encapsulated.

AEM and ADM Test Data

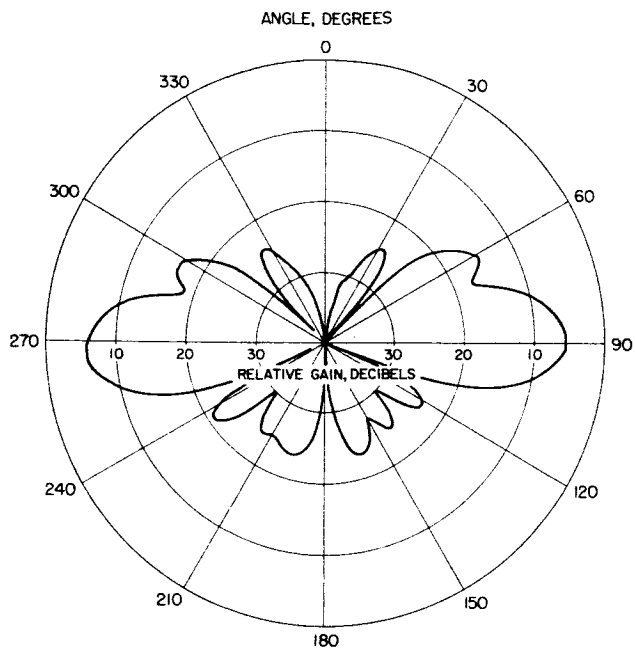
Life test data for the AEM and ADM are given in Tables 5-10 and 5-11.

The life test plan follows:

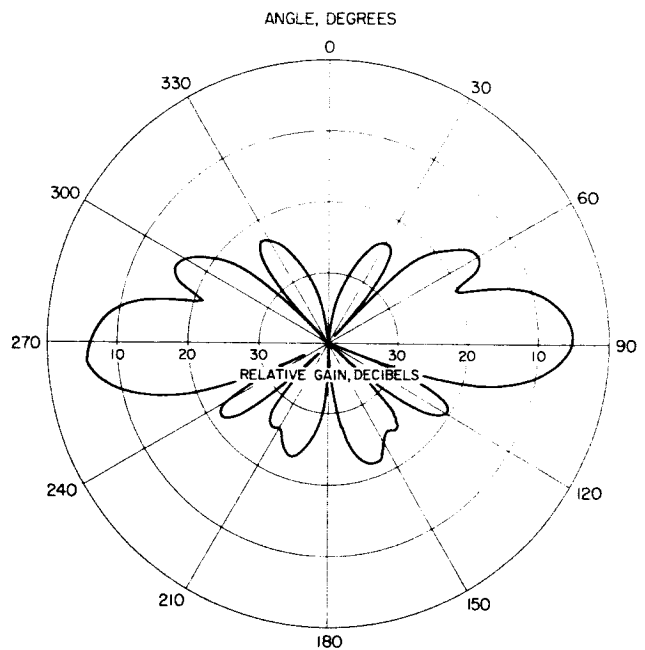
This test plan covers the life testing of the PACE portion of both the Advanced Engineering Model (AEM) and the Advanced Development Model (ADM). The PACE will be tested as follows:

The listed equipment will be used for making the measurements.

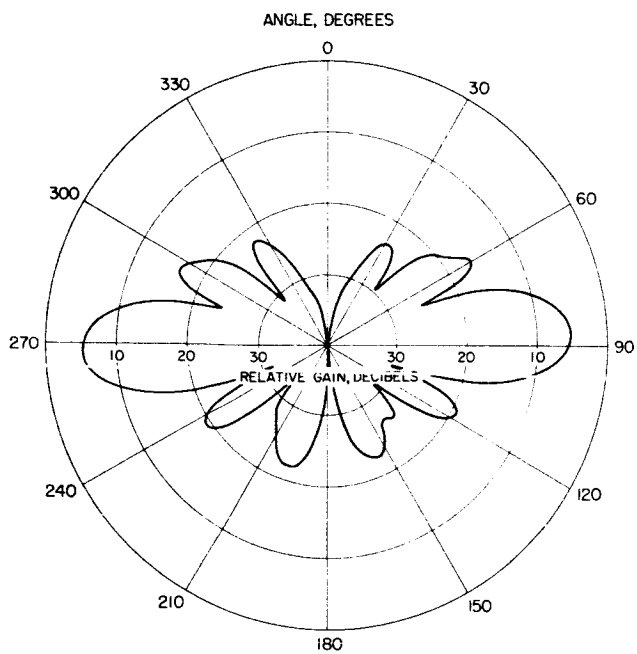
- 1) Oscilloscope, Tektronix, type 535A or equivalent
- 2) Preamplifier, Tektronix, type CA or type M
- 3) $\psi - \psi_2$ simulator, Hughes manufacture
- 4) PACE unit tester, Hughes manufacture
- 5) Electronic counter, Beckman 8360 or equivalent



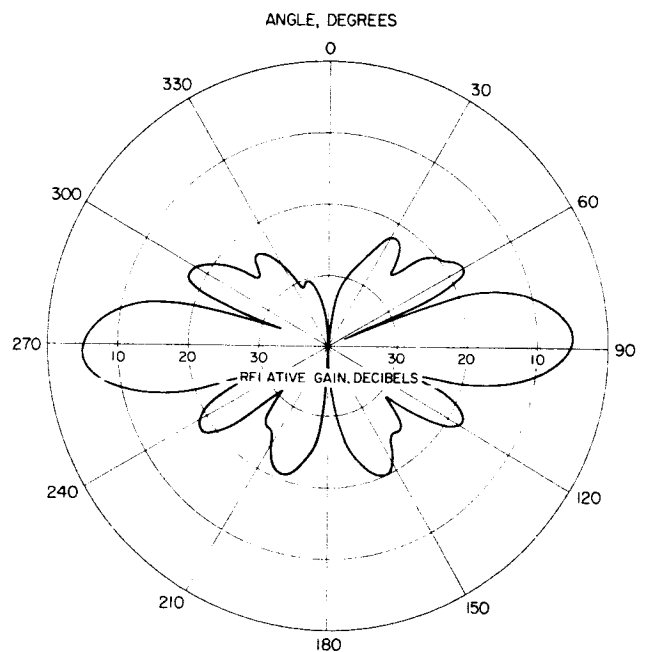
a) $f = 3950 \text{ mc}$



b) $f = 3980 \text{ mc}$

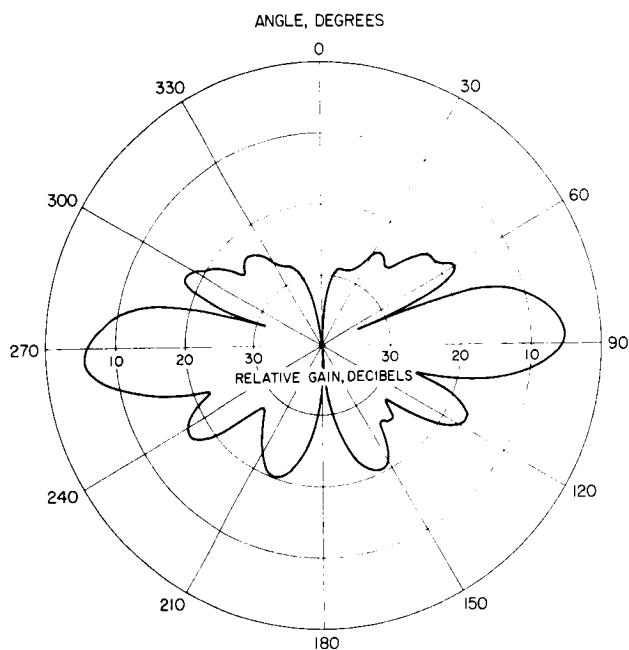


c) $f = 4030 \text{ mc}$

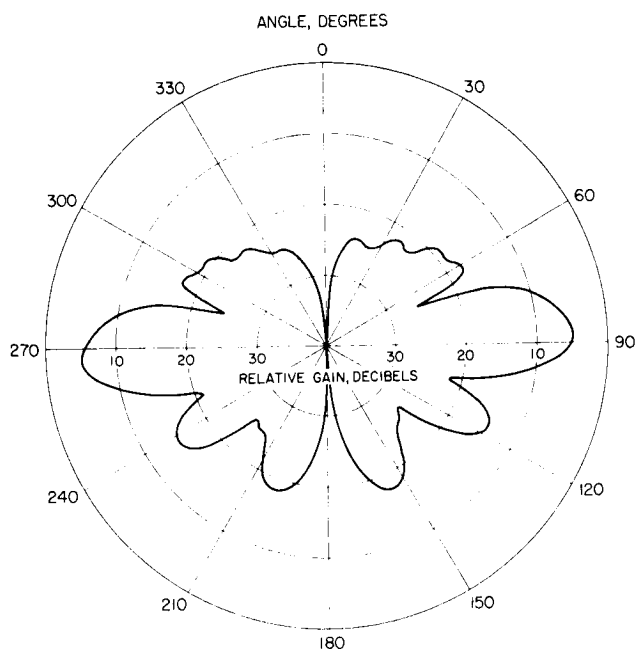


d) $f = 4080 \text{ mc}$

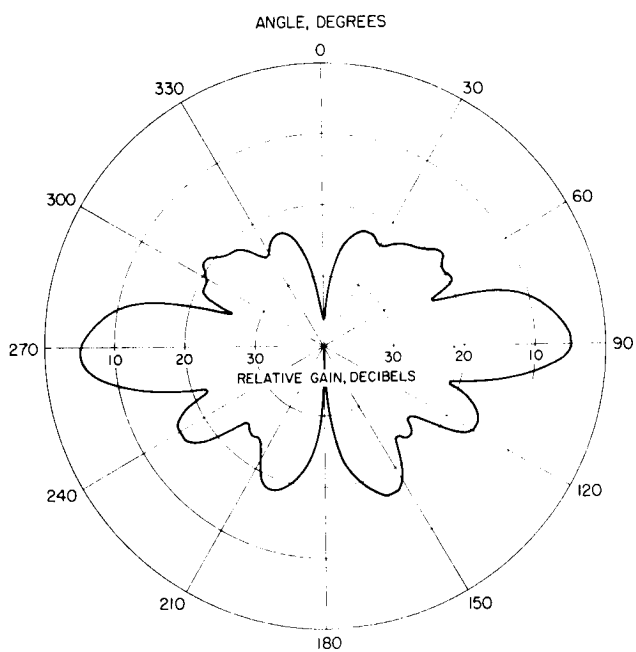
Figure 5-27. Vertical Antenna Pattern
4 dipole vertical antenna



e) $f = 4130 \text{ mc}$



f) $f = 4180 \text{ mc}$



g) $f = 4230 \text{ mc}$

Figure 5-27 (continued). Vertical Antenna Pattern
4 dipole vertical antenna

TABLE 5-10. TEST PERFORMANCE RESULTS AND TEST DATA
FOR AEM AND ADM

PACE AEM Life Test Data

Date	Time	Temperature, °C	Spin Speed, milliseconds	Steady State Error, milliseconds
12/2			400	+25 ±1
			500	-3 ±2
			600	-24 ±1
			800	-76 ±4
			1200	-190 ±5
12/3	8:30		400	+31 ±1
	9:40		500	+5 ±1
	11:00		600	-2 ±1
	12:00		800	-18 ±7
	1:15		1200	-80 ±12
12/4	8:20		400	+30 ±1
	9:30		500	+5 ±2
	10:40		600	-1 ±2
	12:00		800	-21 ±7
	1:00		1200	-74 ±20
12/5	8:30		400	+30 ±1
	9:30		500	+5 ±1
	11:00	35	600	-2 ±4
	12:00	35	800	-27 ±3
	1:30	34	1200	-76 ±14
12/6	8:15	37	400	+29 ±1
	10:00	36	500	+5 ±1
	11:30	35	600	-1 ±2
	2:10	33	800	-12 ±6
	4:30	33	1200	-58 ±13
12/9	8:30	37	400	+23 ±1
	11:00	36	500	+1 ±4
	12:00	35	600	-5 ±3
	2:20	33	800	-17 ±3
	3:20	33	1200	-75 ±9
12/10	8:15	38	400	+31 ±5
	12:00	39	500	+4 ±1
	2:45	32	600	+1 ±3
	4:00	32	800	-30 ±11
	5:00	32	1200	-76 ±10
12/11	8:15	36	400	+22 ±1
	9:45	35	500	4 ±2
	11:15	35	600	-2 ±2
	12:15	34	800	-25 ±3
	1:15	33	1200	-82 ±6

TABLE 5-10. (continued)

Date	Time	Temperature, °C	Spin Speed, milliseconds	Steady State Error, milliseconds
12/12	8:15	38	400	+26 ± 2
	9:30	37	500	-14 ± 2
	10:30	36	600	-3 ± 4
	11:30	35	800	-31 ± 4
	2:00	35	1200	-86 ± 12
	8:30	38	400	-135 ± 1
12/13	9:30	37	500	-13 ± 3
	10:30	37	600	-5 ± 4
	11:45	36	800	-32 ± 6
	1:45	36	1200	-96 ± 4
	8:45	35	400	+18 ± 2
	10:30	35	500	-13 ± 2
12/16	12:00	36	600	-4 ± 3
	2:15	36	800	-25 ± 6
	3:15	37	1200	-115 ± 7
	8:15	36	400	+19 ± 3
	9:30	37	500	+2 ± 2
	11:15	37	600	-3 ± 4
12/17	12:15	37	800	-34 ± 4
	4:30	33	1200	-82 ± 6
	12:00	33	400	+22 ± 2
	1:45	33	500	-15 ± 1
	3:10	33	600	+4 ± 4
	4:15	30	800	-13 ± 2
12/18	5:15	30	1200	-58 ± 6
	9:15	34	400	+42 ± 2
	10:30	32	500	+18 ± 4
	11:30	30	600	+4 ± 3
	1:20	29	800	-1 ± 5
	2:30	30	1200	-37 ± 13
12/19	8:40	29	400	+47 ± 4
	9:40	29	500	+10 ± 5
	10:40	29	600	-3 ± 5
	3:15	31	800	-10 ± 20
	4:30	31	1200	-90 ± 42
	9:05	34	400	+36 ± 4
12/20	11:30	33	500	-12 ± 3
	1:15	34	600	-4 ± 7
	2:15	34	800	-60 ± 8
	4:15	34	1200	-150 ± 7
	8:00	36	400	+22 ± 2
	10:45	36	500	3 ± 3

TABLE 5-10. (continued)

Date	Time	Temperature, °C	Spin Speed, milliseconds	Steady State Error, milliseconds
12/27	12:00	36	600	-3 ± 3
	1:30	36	800	-29 ± 6
	2:30	35	1200	-105 ± 35
	8:00	35	400	+21 ± 2
	9:00	35	500	+3 ± 3
12/28	10:00	34	600	-5 ± 4
	11:15	33	800	-20 ± 5
	12:15	32	1200	-69 ± 19

The missing times and temperatures at the beginning of the month reflect a change in the method of taking data. Prior to that time neither of these two quantities were measured, but it was discovered that inconsistent results were being obtained. This was caused by not allowing enough time between measurements so that the loop had not yet reached a stable condition. The temperature is that of the air directly over the chassis of the AEM. Since the temperature in the laboratory does not vary greatly, it should cause little change in the steady-state error. The uncertainty shown in the steady-state error is a measure of the amount of jitter existing in the error.

TABLE 5-11. PACE ADM LIFE TEST DATA

Date	Time	Temperature, °C	Spin Speed, milliseconds	Steady State Error, milliseconds
12/2	8:30		400	45 ± 14
			500	40 ± 10
			600	15 ± 15
			800	14 ± 10
			1200	60 ± 60
12/3	9:40		400	40 ± 15
	11:00		500	15 ± 7
	12:00		600	20 ± 20
	1:15		800	12 ± 8
	2:15		1200	Equipment in use
12/4	8:30		400	35 ± 5
	9:30		500	19 ± 12
	10:40		600	12 ± 8
	12:00		800	26 ± 22
	1:30		1200	70 ± 60
	8:30		400	32 ± 10
	9:30		500	20 ± 8

TABLE 5-11. (continued)

Date	Time	Temperature, ° C	Spin Speed, milliseconds	Steady State Error, milliseconds
12/5	11:00		600	20 ±20
	12:00		800	20 ±20
	1:30		1200	40 ±40
	8:45		400	30 ±3
	10:00		500	15 ±13
12/6	11:30		600	15 ±13
	2:10		800	25 ±25
			1200	Equipment in use
			400	29 ±9
			500	15 ±13
12/9			600	10 ±2
			800	13 ±11
			1200	
At this point the test was interrupted to make modification to the test equipment and to the waveform generator function board.				

The following input voltages will be supplied to the AEM/ADM continuously:

- 1) +24 volts (PACE) ±3 percent
- 2) -24 volts (PACE) ±3 percent
- 3) +24 volts (PA) ±3 percent
- 4) -24 volts (PA) ±3 percent
- 5) +35 volts (PA) ±5 percent
- 6) -35 volts (PA) ±5 percent

The steady-state error of the frequency lock-loop is defined as the time period between the positive-going edges of the flip-flops F100 and F113. This error will be determined by using the following procedure:

- 1) Connect the output of the $\psi - \psi_2$ simulator to the ψ input of the PACE and adjust the simulator for a pulse rate of 400 milliseconds.
- 2) Connect channel A and channel B of the oscilloscope to F100 and F113. Set the mode switch to chopped and trigger the oscilloscope on the negative going edge of F100.

- 3) Connect channel A and channel B of the electronic counter to F500 and F100. Adjust the counter to read the ratio between the two inputs.
- 4) Allow 1 hour for the loop to stabilize. The ratio count will be 8192 ± 1 count.
- 5) When the loop has stabilized, determine with the oscilloscope the steady-state error. Record the average error and the amount of deviation or jitter on the appropriate portion of the data sheet. Record the time of day and the temperature of the room at the time the measurement was made.

Note: To observe the steady-state error accurately, it will be necessary to use the delaying feature of the oscilloscope.

- 6) Switch the $\psi - \psi_2$ simulator through the other spin rates of 500, 600, 800 and 1200 milliseconds. Repeat steps 4 and 5 for each change of spin rate.
- 7) Repeat the entire procedure daily during each scheduled work day. Note any significant deviations from normal in the comments column of the data sheet.

On the last working day of each week, check the output waveforms as follows:

- 1) Connect channel A and channel B of the oscilloscope to PA1-A and PA1-B, respectively.
- 2) Observe the waveform and note any unusual distortion such as clipping or flattening of the waveform peaks. Check for excessive dc level shift.
- 3) Switch to channel A only. Connect PA1-B to the horizontal input of the oscilloscope. Adjust the attenuation so that a circle is traced on the screen, noting any unusual projections or indentations on any portion of the circle.
- 4) Repeat steps 1, 2, and 3 for waveform outputs PA2-A, PA2-B, through PA8-A, PA8-B.

Phase Shifter Driver Status

The power amplifier cards have been modified to bring them up to the latest design configuration. The chassis has been rewired so that either the dc-dc converter or external power supplies may be used. This was done to ensure that testing of the other parts of the system could proceed even if

the dc-dc converter is not yet ready. The converters are expected to be complete by mid-January.

Electrical Power System – Spin Stabilized, Synchronous Altitude Configuration

System Design

The electrical power system, unchanged since the October Summary Report, is shown in Figure 5-28. In this system, the battery is charged from a series of isolated solar cell strings. The degree of charge is dependent on the voltage of the unregulated bus. The battery on-charge voltage will be 0.5 to 0.7 volt higher than bus voltage due to the voltage drop across the discharge logic diode.

The solar cell specification will be revised to represent the latest cells available. Currently, 10 ohm-cm cells with 0.475 volt /cell at 25 milliwatts are being procured from Heliotek for the Syncom 1 spacecraft. The solar array performance (reflecting the above change) is shown in Figure 5-29.

Reaction Control Systems

A study report has been issued describing the initial tradeoff studies conducted in the area of a Reaction Control System for use in the Synchronous Altitude Gravity-Gradient (SAGGE) configuration.

Preliminary procurement specifications for the synchronous altitude hydrogen peroxide system are being completed.

Structure and Spacecraft Configuration Design

The synchronous altitude spin stabilized configuration utilizes the T-2 model structure with revised mountings for the reaction control system and experimental payloads.

General Arrangement

A general arrangement study was made this month to show the payload volume capability of the vehicle. All of the experiments listed in the November Monthly Report have been installed along with a preliminary reaction control system. The configuration is detailed in Figure 5-30.

The reaction control system and the nuclear arms package shown are not up to date, due to last-minute changes. The revised units and the selected payload will be detailed in the next report.

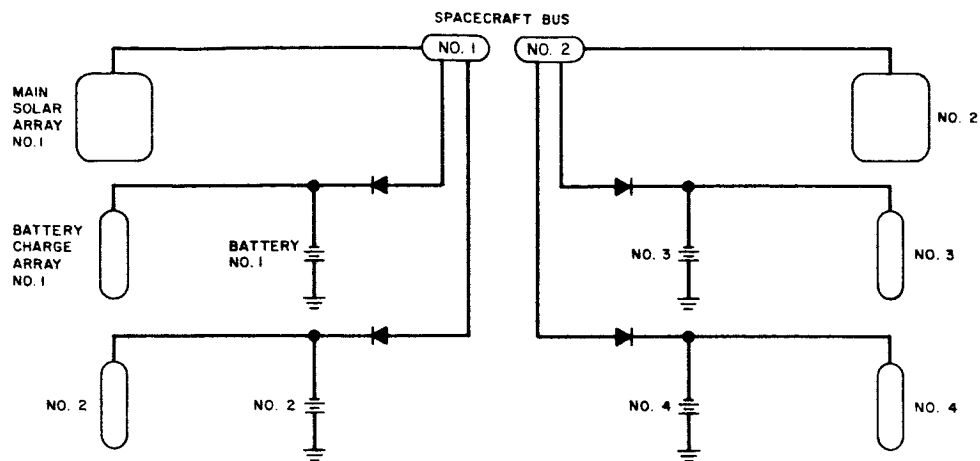


Figure 5-28. Power System Schematic

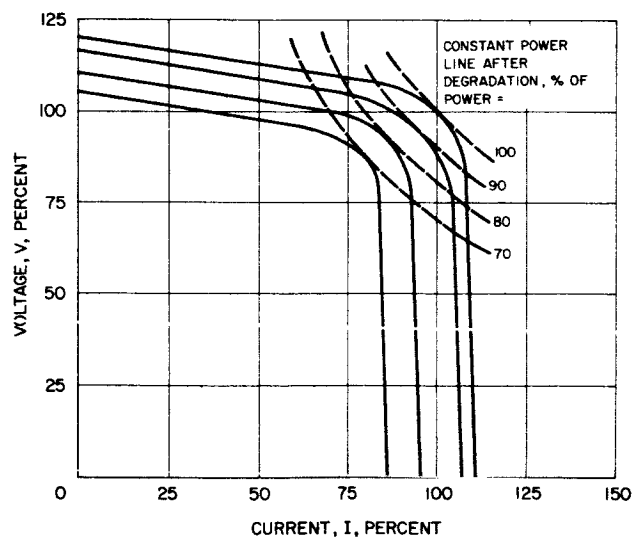


Figure 5-29. Solar Array Performance

Mass Properties

A detailed weight breakdown for the items common to both the spin stabilized vehicles are tabulated as the Advanced Syncom Basic Spacecraft in Table 5-12. The weight changes since the November Report are explained below and are shown under the heading Δ Weight of Table 5-12.

	<u>Weight Change, pounds</u>
Wire harness subsystem	(+23.00)
Main harness - redundancy in wiring added for multiple payload capability	+24.20
Quadrant - wiring included in main harness	- 1.20
Miscellaneous subsystem	(- 3.36)
Nutation damper - deleted from basic spacecraft	- 2.00
Ground planes - revised weight estimate	+ 2.64
Thermal barrier - deleted from basic spacecraft	- 4.00
Basic spacecraft	<u>+19.64</u>

The weight breakdown for the synchronous altitude, spin stabilized spacecraft (SASSE) is shown by Table 5-13. It reflects the weight changes since last reported (ΔW). A brief explanation for each weight change follows:

	<u>Weight Change, pounds</u>
Basic spacecraft	(+19.6)
See Table 5-12	+19.6
Miscellaneous subsystem	(+ 8.4)
Nutation damper - formerly listed in basic spacecraft	+ 2.0
Thermal barrier - revised weight estimate and formerly listed in basic spacecraft	+ 6.4
Controls subsystem	(-22.9)
Cold gas spinup	+ 4.3
Revised weight estimate on system components	
Reaction control system	-27.2
H ₂ O ₂ type system incorporated in lieu of bi- propellant system	

	Weight Change, pounds
Payload	(+ 8.3)
Engineering experiment	+ 3.0
Revised weight estimate	
Meteorological package	(+ 5.3)
Camera hi-resolution - revised weight	
estimate based on updated information	+ 1.4
Installed hardware - revised weight estimate	+ 3.9
Final orbit condition	(+13.4)
Propellant - RCS	(- 9.9)
Revised weight based on new system	
requirements	- 0.9
Yo-Yo despin mechanism deleted from system	- 9.0
Total at apogee burnout	(+ 3.5)
Total at separation from booster	+ 3.5

The mass property data for SASSE is shown in Table 5-14. Although the roll-to-pitch moments of inertia ratios as shown do not meet the minimum design requirements, significant areas exist to exercise the proper mass distribution control necessary to meet the requirements. Since the November Report, the time spent on the SASSE configurations was limited to updating weights. No attempt has been made to date to locate the masses to produce the optimum roll-to-pitch ratios. Therefore, complete distribution analyses will be made. These will be aimed at producing the maximum roll-to-pitch moment of inertia without compromising other design parameters.

Two distinct payload combinations have been investigated for the SASSE spacecraft, one of which has been incorporated to determine the mass properties shown in Tables 5-13 and 5-14. The alternate payload listed in Table 5-15 consists of a Department of Defense transponder, a Communications Satellite Corporation transponder, and an RF propagation experiment and has been investigated from an allowable weight standpoint only. However, it appears that this payload combination has the ability to be located on or near the longitudinal center of gravity plane and at the periphery of the spacecraft which will generate higher roll-to-pitch ratios than indicated for the primary payload.

TABLE 5-12. DETAILED WEIGHT BREAKDOWN OF
ADVANCED SYNCOM BASIC SPACECRAFT

Component		Δ Weight, pounds	Weight, pounds
<u>Electronics Subsystem</u>			(87.19)
Electronic quadrant			(27.71)
Transponder			(15.70)
475101	Regulator (1)		0.17
475102	Regulator (1)		0.17
475104	Internal amplifier (1)		0.17
475109	Limiter (1)		0.15
475111	Postamplifier (1)		0.15
475112	High level mixer (1)		0.35
475113	Master oscillator (1)		0.37
475114	X32 multiplier (3)		1.91
475115	Isolator (7)		1.56
475116	X3 multiplier (2)		0.35
475117	X2 multiplier (2)		0.43
475122	Master oscillator (1)		1.87
475123	Master oscillator amplifier (1)		0.15
475124	Attenuator (3)		0.07
475126	Isolator (3)		0.38
475131	Phase modulator (1)		0.20
475132	Doubler amplifier (1)		0.24
475141	Filter amplifier (1)		0.21
	Bandpass filter (4)		0.61
	Dual filter hybrid (1)		0.35
	Mounting bulkheads (2)		3.38
	RF shield		0.50
	DC connectors		0.16
	Coax cables		1.22
	Miscellaneous attachments		0.58
475221	Telemetry encoder		1.50
475303	Central timer		0.60
	Encoder and timer installation hardware		2.00
475210	Command receiver		0.54
475212	Command regulator		0.56
475201	Diplexer		0.31
	Receiver regulator and diplexer installation hardware		2.50
	PACE		4.00

TABLE 5-12. (continued)

Component		Δ Weight, pounds	Weight, pounds
Rib-mounted units			(34.87)
	Quadrant regulator (3)		3.90
475220	Telemetry transmitter (3)		2.10
475221	Telemetry encoder (3)		4.50
475222	Telemetry regulator (3)		0.84
475212	Command regulator (3)		1.68
475210	Command receiver (3)		1.62
475211	Command decoder (4)		8.00
475201	Diplexer (3)		0.93
475125	Traveling-wave tube (2)		2.20
475174	Traveling-wave tube power supply (2)		2.50
475173	RF switch (1)		0.20
475103	20-db coupler (1)		0.10
475171	3-db coupler (1)		0.20
	Antenna electronics (1)		2.10
475170	Phase shifter (2)		4.00
Communication antenna (1)			19.51
Antenna support structure and cable			1.50
Forward end of spacecraft			(3.60)
	Telemetry regulator (1)		0.30
475220	Telemetry transmitter (1)		0.50
475204	Whip antenna (16)		1.30
475200	Hybrid balun (2)		1.50
Wire Harness Subsystem		(+23.00)	(33.00)
Main harness		+24.20	33.00
Quadrant		- 1.20	0
Power Supply Subsystem			(58.09)
X209781	Substrate - solar cell		23.27
X209888	Solar cell		34.82
Structure Subsystem			(82.82)
X209862	Aft subassembly		(42.86)
X209813	Ring-separation		4.09
X209875	Tube-thrust		4.71
X209812	Ring-motor mount		5.34

TABLE 5-12. (continued)

Component		Δ Weight, pounds	Weight, pounds
X209896	Ribs		16.20
X209816	Ring-frame		0.94
X209882	Bulkhead		6.53
X209862	Miscellaneous hardware		0.87
X209793+879	Attachment - SP		2.78
X209863	Miscellaneous		1.40
X209883	Center subassembly		(24.12)
X209874	Tube-thrust		5.65
X209884	Stiffener-tube		5.68
X209857	Ring-zee support		0.32
X209885	Support-electronic package		0.56
X209883	Miscellaneous hardware		0.78
X209855	Support-solar panel		3.92
X209785	Retainer-solar panel		0.51
X209854	Support-forward channel		3.60
X209863	Miscellaneous		3.10
X209850	Forward subassembly		(10.62)
X209851-1	Tube truss		1.07
X209848	Fittings-forward truss		0.39
X209850	Hardware-forward fittings		0.07
X209849	Fittings-aft truss		0.66
X209850	Hardware-aft fittings		0.10
X209853	Channel-support		0.74
X209871	Torus assembly		4.49
X209880	Support-solar panel		2.60
X209863	Miscellaneous hardware		0.50
	Miscellaneous supports		(5.22)
	Support-wire harness		1.50
	Support-rib mounted units		1.43
X209856	Support-antenna compartment		1.64
X209902	Support-whip antenna		0.65
<u>Miscellaneous Subsystem</u>		(- 3.36)	(14.43)
X209866	Sun sensor		1.15
	Paint		3.00
	Nutation damper	- 2.00	0
X209909	Ground plane-inner	+ 0.87	1.74
X209911	Ground plane-outer	+ 1.77	3.54
X209910	Thermal barrier	- 4.00	0
	Static and dynamic balance		5.00
<u>Basic Spacecraft</u>		+19.64	275.53

TABLE 5-13. WEIGHT BREAKDOWN OF SYNCHRONOUS ALTITUDE
SPIN STABILIZED SPACECRAFT

Description	Δ Weight, pounds	Current Weight, pounds
Electronics subsystem		87.2
Wire harness subsystem		33.0
Solar cell subsystem		58.1
Structure subsystem		82.8
Miscellaneous subsystem		14.4
Basic spacecraft	(+19.6)	(275.5)
Apogee motor (fired)		102.6
Miscellaneous subsystem	(+ 8.4)	(8.4)
Nutation damper	+ 2.0	2.0
Thermal barrier	+ 6.4	6.4
Controls subsystem	(-22.9)	(39.2)
Cold gas spinup	(+ 4.3)	(19.3)
Jets (2) and miscellaneous components	+ 0.3	5.5
Tanks (2) and miscellaneous components	+ 4.0	13.8
Reaction control system	(-27.2)	(19.9)
Jets (4)	- 7.0	3.2
Tanks and supports	-16.0	11.0
Valves, lines and miscellaneous	- 4.2	5.7
Payload*	(+ 8.3)	(110.8)
Radiation and micrometeorite detection package		25.5
Engineering experiment	+ 3.0	28.0
Meteorological package	(+ 5.3)	(57.3)
Camera - lo-resolution		8.1
Camera - hi-resolution	+ 1.4	14.7
Camera electronics		13.6

* Payload does not require multiplexers.

TABLE 5-13. (continued)

Description	Δ Weight, pounds	Current Weight, pounds
Sequence timer		8.0
Flasher		1.8
IMC and IMC electronics		2.2
Installed hardware and miscellaneous	+ 3.9	8.9
Battery power supply subsystem		(69.2)
Batteries		54.6
Supports		14.6
Final orbit condition	(+13.4)	(605.7)
Propellant-RCS	- 0.9	135.2
Yo-Yo despin mechanism	- 9.0	0
Total at apogee burnout	(+ 3.5)	(740.9)
Propellant - apogee motor		752.3
Expendables - apogee motor		19.6
Total at spinup prior to apogee fire	(+ 3.5)	(1512.9)
Propellant - cold gas spinup		6.1
Total at separation from booster	(+ 3.5)	(1519.0)

Structural Analysis

Vibration analyses of the spacecraft adapter combination have been modified to include the current adapter flexibility coefficients. The adapter thickness, required to meet the minimum frequency criterion of 25 cps, is 1/8 inch.

The spacecraft-adapter model used in these calculations includes flexibilities for the Marmon band and for the joint at Agena station 247, and represents the spacecraft by a weightless beam supporting the proper mass and mass moment of inertia. The adapter flexibility coefficients are based on minimum values of material properties and represent an unstiffened fiberglass shell.

TABLE 5-14. SYNCHRONOUS ALTITUDE SPIN STABILIZED
SPACECRAFT MASS PROPERTY DATA

Conditions	Current Weight, pounds	Z-Z, inches	I_{roll} , slug-ft ²	I_{pitch} , slug-ft ²	Roll- to- Pitch Ratio
Final orbit condition	605.7	23.90	58.7	54.0	1.09
RCS propellant	135.2	23.90			
Total at apogee burnout	740.9	23.90	72.6	60.9	1.19
Apogee motor propellant	752.0	23.25			
Apogee motor expendables	20.0	19.64			
Total after spinup prior to apogee motor burn	1512.9	23.02	89.5	78.1	1.15
Cold gas spinup propellant	6.1	8.00			
Total at separation from boost booster	1519.0	22.96	90.1	78.8	1.14

The test plan for developmental structural testing of the production version solar panel has been completed and is being published. Arrangements have been made with North American Aviation for the use of their acoustic test facility.

Thermal Design

The thermal design for the vehicle remains the same as previously reported. Some consideration is being given currently to the amount of thermal protection that may be required to minimize damage caused by plume effects of the apogee motor during firing. Although it was reported in the October Summary Report that convective heating effects on the forward end of the vehicle during apogee motor firing were expected to be of low magnitude and that radiative heating of the sun sensors to 250° F was expected, geometry changes occurring since that analysis have inspired a new look at that problem. Consideration is currently being given to include some form of sensing devices of the Syncom I, F-2 vehicle to possibly obtain some information concerning plume effects that may be directly applicable to the Advanced Syncom design.

TABLE 5-15. ALTERNATE PAYLOAD FOR THE SYNCHRONOUS ALTITUDE SPIN STABILIZED SPACECRAFT

Description	Weight, pounds
Department of Defense transponder	(31.5)
Transponder*	24.0
Traveling-wave tube	2.5
Traveling-wave tube power supply	2.5
Diplexer	1.0
Installed hardware and miscellaneous	1.5
Communications Satellite Corporation transponder	(35.0)
Transponder*	27.5
Traveling-wave tube	2.5
Traveling-wave tube power supply	2.5
Diplexer	1.0
Installed hardware and miscellaneous	1.5
RF propagation experiment	(23.0)
Transponder*	15.7
Traveling-wave tube	3.5
Traveling-wave tube power supply	2.5
Installed hardware and miscellaneous	1.3
Total alternate payload	89.5

* Additional transponders will need addition of multiplexers to system.

Apogee Injection Motor Status

The apogee injection motor is being developed by JPL and will be supplied to Hughes as a Government-furnished equipment item. The motor is a scale-up of the JPL Starfinder which was used successfully on Syncom 2.

The heavywall static tests, hydrotests, and ignition test phases of the program have been completed. Three sets of flight-weight hardware have been received by JPL; processing of the first set will begin during the first week of January. Development static tests of flight-weight hardware will be initiated during January 1964.

Electrical Power System – Synchronous Altitude, Gravity-Gradient Configuration

System Design

As previously reported, the gravity-gradient stabilization method creates two additional solar array problem areas. These are: 1) reduced

solar cell output voltage resulting from the higher stabilized solar panel temperature, and 2) reduced power available as a function of solar cell shadowing by the added stabilization booms and libration damper. The net effect of the boom shadowing (two different locations) is shown in Figure 5-31. These data were based on an experimental shadow model and mathematically checked at several points. As can be deduced from the figures, the power available can vary by approximately 10 percent depending on boom geometry.

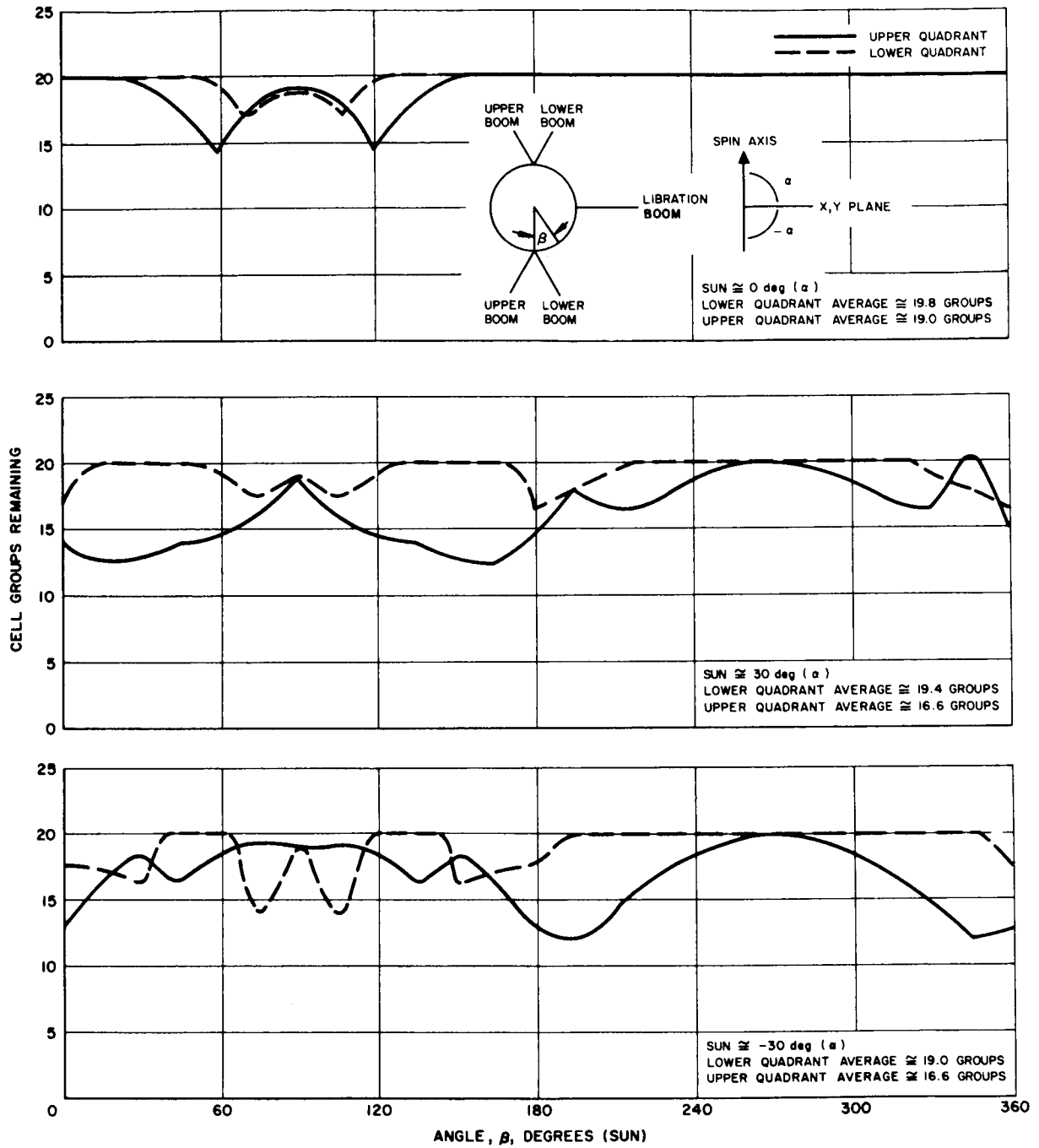
Figure 5-32 represents various methods of connecting the solar cells into the electrical power system. The series connection of the upper and lower quadrants (Figure 5-32a) is, perhaps, the simplest interconnection method resulting in the required output voltage. Since the array output would approximate the least power curve shown, the dissymmetry of power from boom shadowing is quite appreciable. Therefore, the series connection of the upper and lower quadrants is not recommended. Figure 5-32b utilizes dc-dc converters between the array and the bus to transform the low array voltage to a level compatible with the load equipment. This system, although having the advantage of common solar panel design with only an added component required for system operation, has the following major disadvantages:

- 1) Reduced reliability due to the addition of a series element in the system.
- 2) Reduced power available to the bus (converter loss).

The solar cell string groups could also be reconnected, as shown in Figure 5-32c, to a system essentially like the spin stabilized version. The batteries in this system also depend on the main bus voltage for charge condition with the state-of-charge being a function of light and eclipse load conditions. Figure 5-32d represents another method of solar cell interconnection which uses a few series-parallel solar cells to raise the battery on-charge voltage to a level required to fully charge the battery. This system requires a discharge logic device to connect the battery to the bus when required. It also represents a continuous load demand to the bus, since the batteries would be operating under over-charge conditions during noneclipse orbits. This condition could readily be corrected by the addition of a command switch in the battery charging circuit. The system offers the advantages of 1) elimination of bus voltage dependence for battery charging, and 2) batteries can be maintained in a fully-charged state.

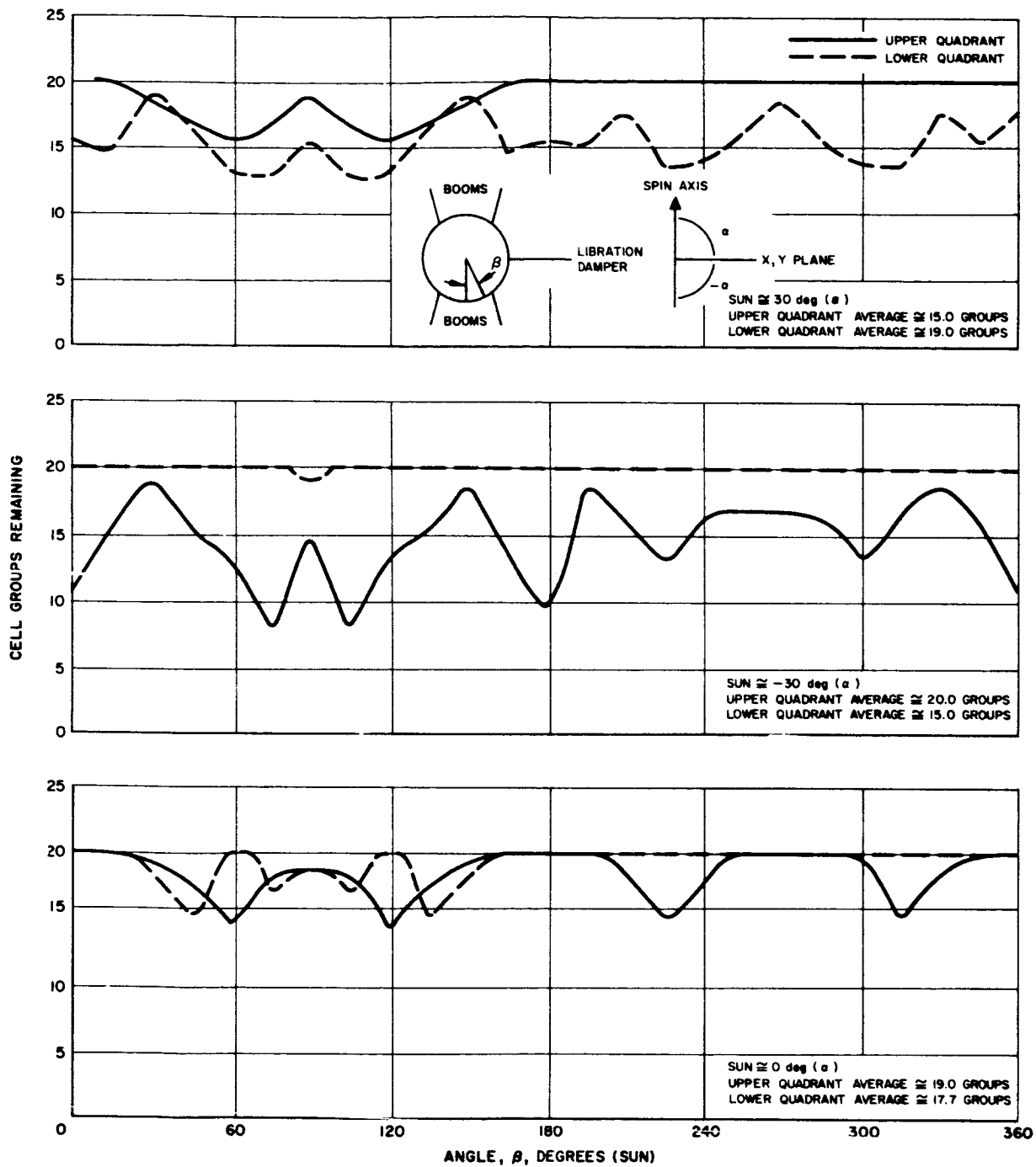
Battery Charging

Figure 5-33 represents the light and dark time electrical load capability of a solar array-rechargeable battery system in a synchronous orbit (22,400 miles). The loads shown are calculated to meet the condition that all the energy expended during the dark period of orbit is replaced in the succeeding light period. The maximum dark time per orbit is fixed for any given orbital altitude.



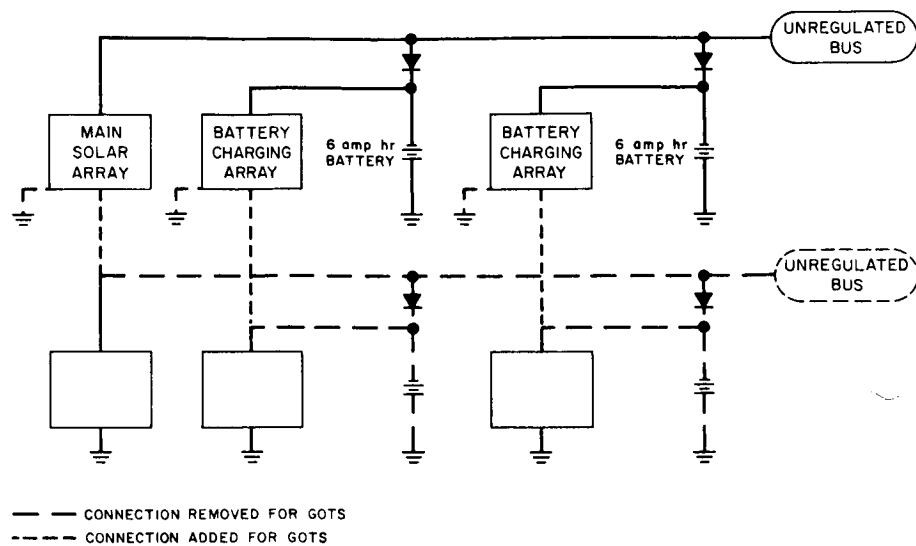
a) Top plane booms

Figure 5-31. Solar Cell Group Loss from Gravity-Gradient Boom Shadows

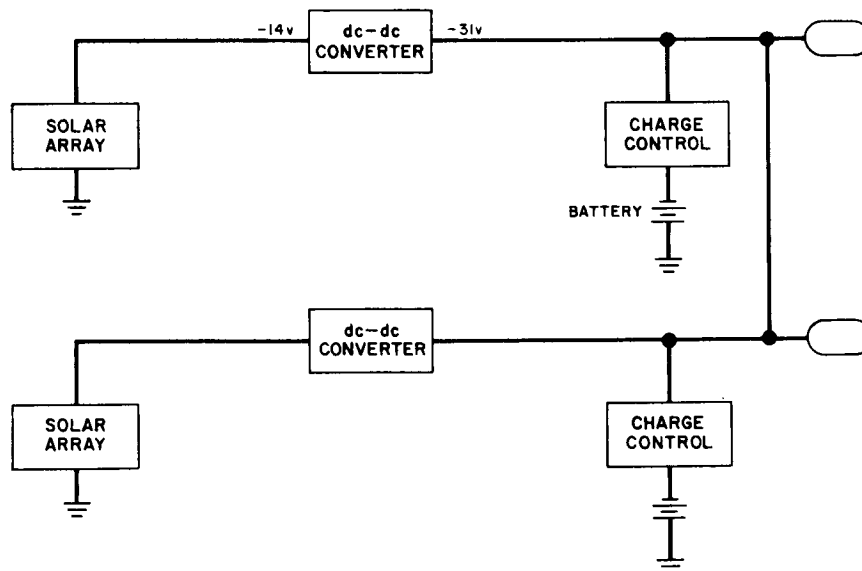


b) Equatorial plane booms

Figure 5-31 (cont). Solar Cell Group Loss from Gravity-Gradient Boom Shadows

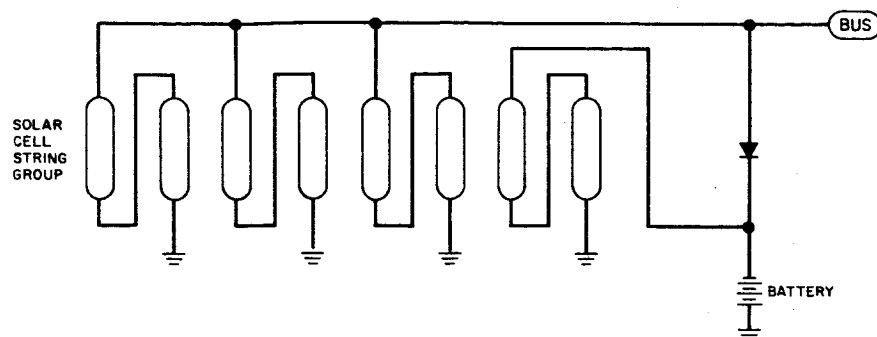


a) Alternate A

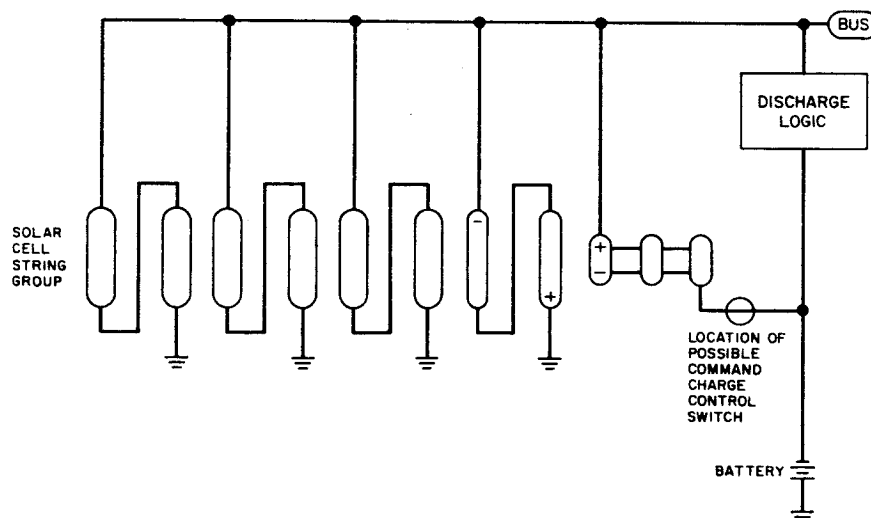


b) Alternate B

Figure 5-32. Electrical System Schematic



c) Alternate C



d) Alternate D

Figure 5-32 (continued). Electrical System Schematic

Since the energy expended in the dark must be replaced during sunlight, the maximum dark time load current will be a function of battery recharge current available during sunlight, the period of sunlight and battery recharge efficiency. The following expression accounts for the charge and discharge currents for zero net energy change per orbit.

$$I_{SA} \cdot t_L = I_L \cdot t_L + \frac{I_D \cdot t_D}{\eta}$$

I_{SA} = solar array current available

t_L = period of sunlight

t_D = period of darkness

I_L = load current during sunlight

I_D = load current during darkness

η = battery ampere-hour recharge efficiency

Normalizing the dark time load current with respect to solar array current available, the expression of the dark time load current becomes:

$$\frac{I_D}{I_{SA}} = \left(1.00 - \frac{I_L}{I_{SA}} \right) \cdot \frac{t_L}{t_D} \cdot \eta$$

Figure 5-33 is a graphical solution of this equation.

The battery recharge current available is the solar array current available minus the light time load current, or $1.00 - I_L/I_{SA}$ for the normalized case. Thus, the battery recharge current required for the power operating condition of zero net energy change per orbit is:

$$I_{BC} = \frac{I_D}{\eta} \cdot \frac{t_D}{t_L}$$

I_{BC} = battery charge current.

Figure 5-34 is the graphical solution of the above equation for dark time load currents up to 2 amperes. Also shown on the chart is the maximum on-charge voltage of a 6 ampere-hour nickel-cadmium sealed cell operating at 77° F for the various charge currents.

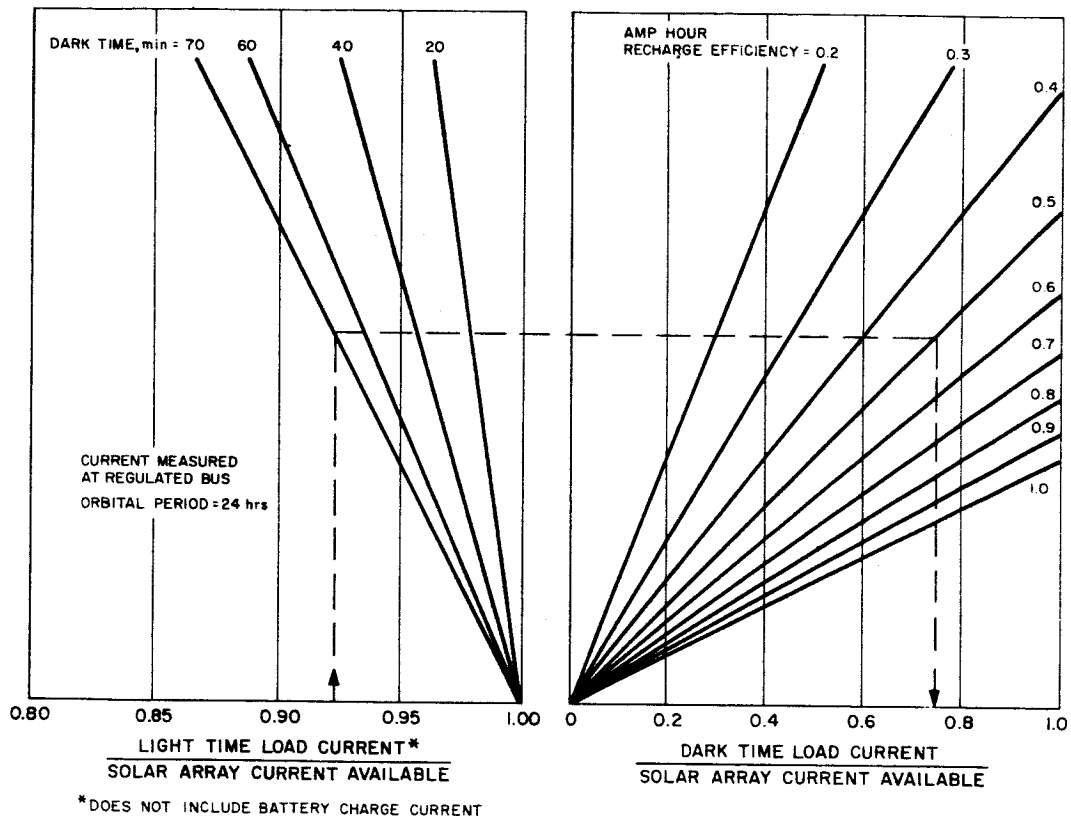


Figure 5-33. Electrical Load Capability—Solar Array and Rechargeable Batteries—Synchronous Circular Orbit

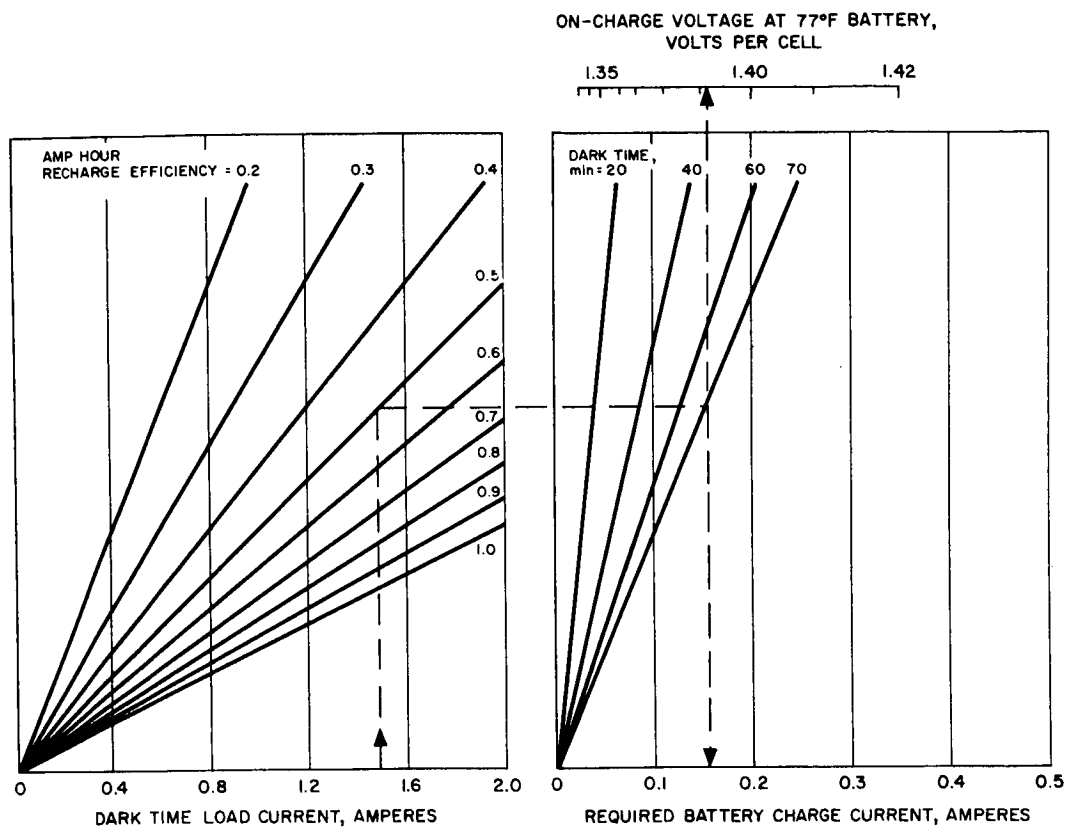


Figure 5-34. Recharge Current Requirements
Synchronous circular orbit

Figure 5-35 shows the relationship between the battery recharge current and the dark time load current for various recharge efficiencies. This relationship is:

$$\frac{I_{BC}}{I_D} = \frac{t_D}{t_L} \cdot \frac{1}{\eta}$$

Reaction Control System

A study report has been prepared which describes the initial tradeoff studies for the SAGGE reaction control system. Additional studies are underway to define pertinent properties of various materials for use as propellant in the valveless SAGGE subliming solid engine.

Preliminary procurement specifications for the SAGGE hydrogen peroxide system and SAGGE specifications relating to the subliming solid system are being completed.

Structure and Spacecraft Configuration Design

The synchronous altitude gravity-gradient design utilizes the same structure as the spin stabilized version with minor modifications to accept the gravity-gradient experiments.

General Arrangement

Most of the effort on SAGGE has been the general arrangement of the basic components and payloads. The rib mounted components were rearranged slightly from the initial layout to balance the libration damper with batteries and to mount the cold gas fuel tanks on the ribs.

Two different sets of layout were made; the first was with the early control system which was comprised of different fuels, supplies, and jets for different spacecraft mission operations. The second was with the latest information on the control system which has a common fuel supply and identical jets for all mission operations. The cold gas spinup system is common to both versions. Late information indicated that additional payload could be carried and the radiation package was included. The second configuration only is detailed, in Figure 5-36.

Mass Properties

Configuration revisions of the synchronous attitude, gravity-gradient spacecraft to provide acceptable roll-to-pitch moment of inertia ratios without employing spin booms and the updating of weight estimates accounted for a major portion of the effort since the last reporting period. Continued effort

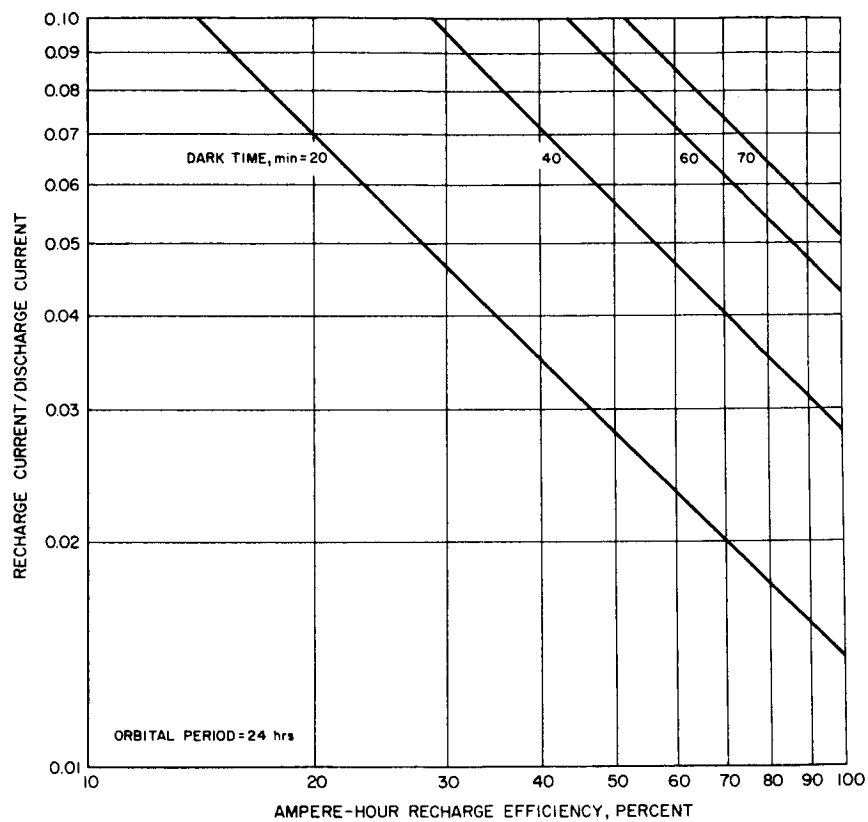
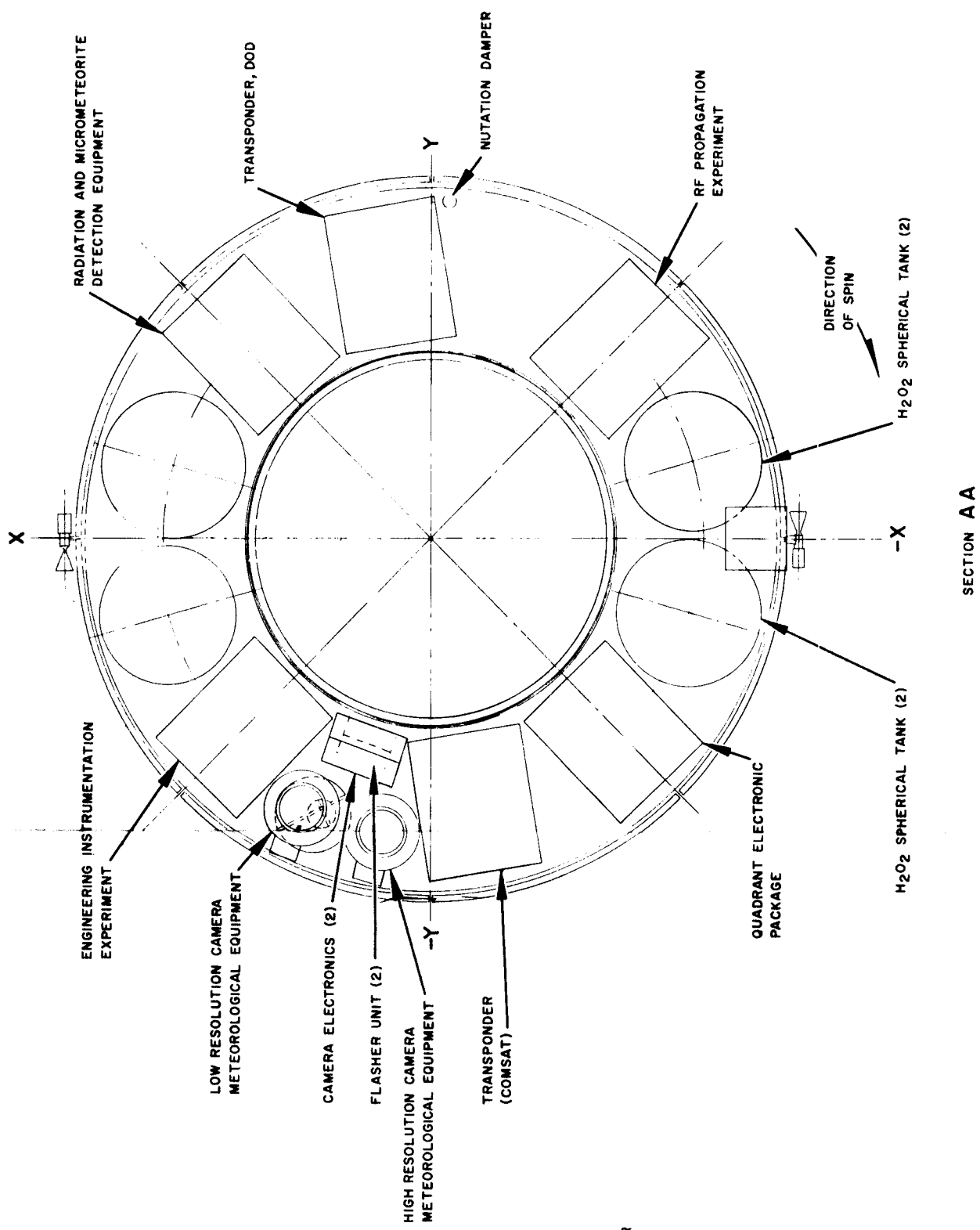
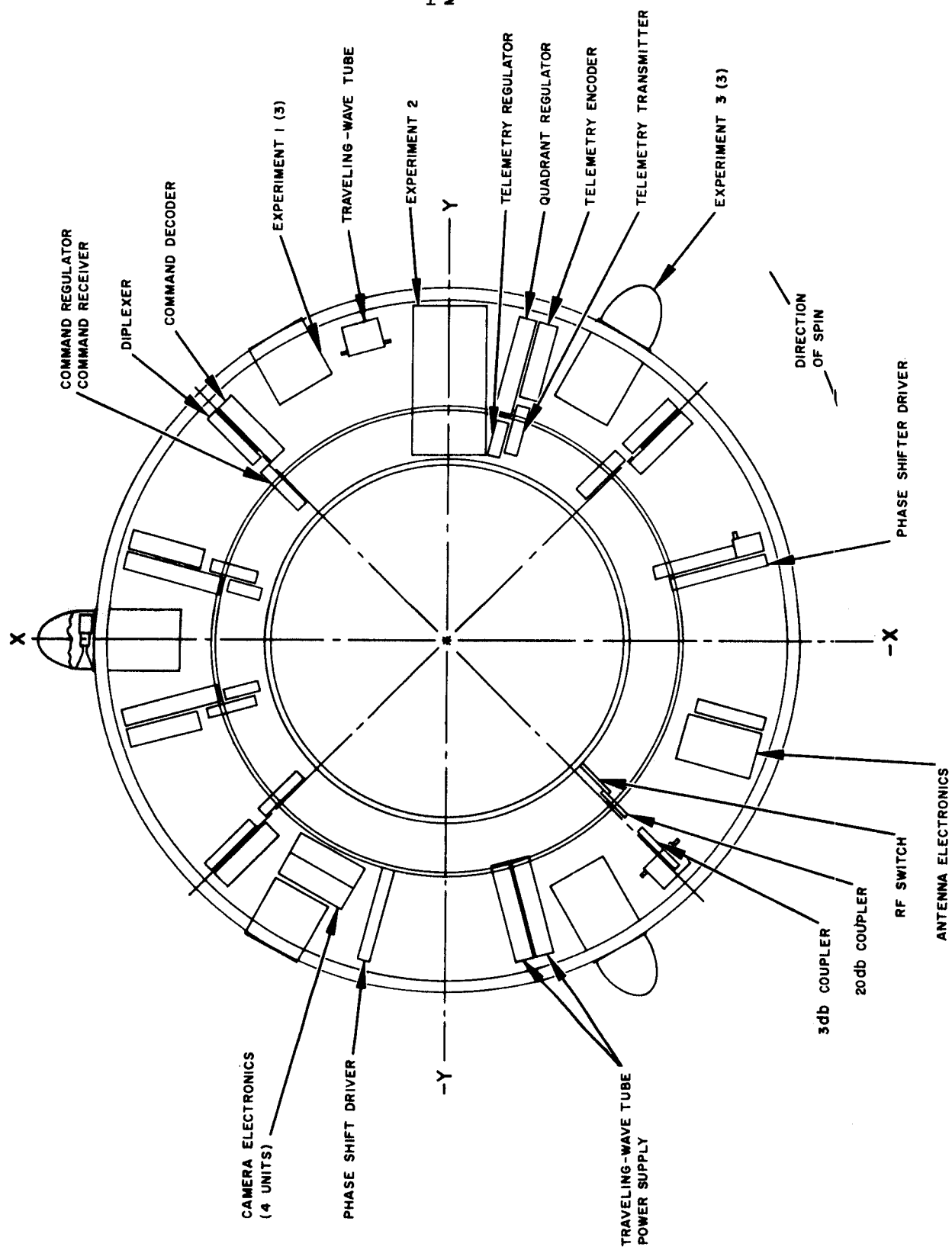


Figure 5-35. Ratio of Recharge Current to Discharge Current for Synchronous Circular Orbit

RETRACTED POSITION



SECTION A A

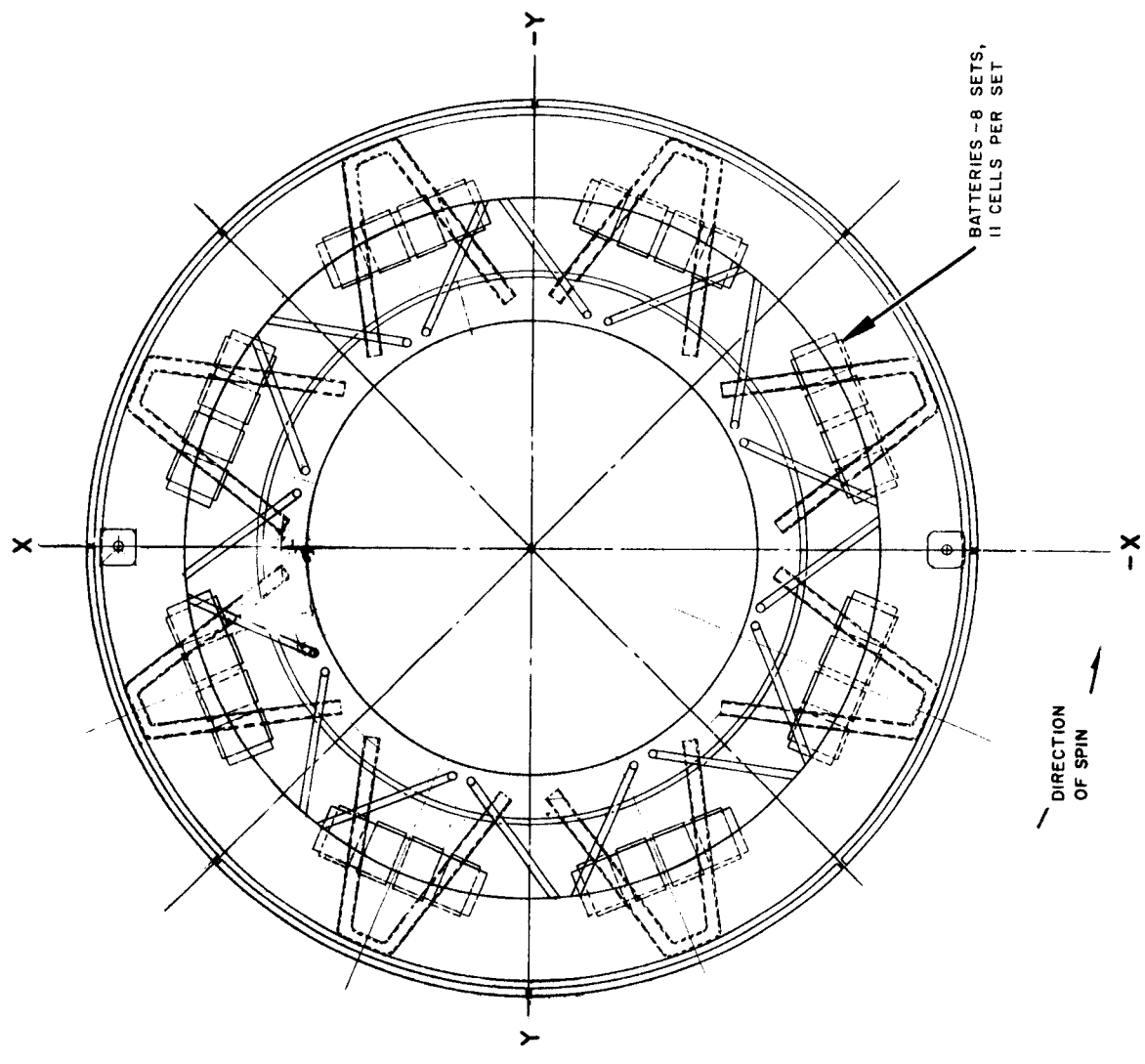
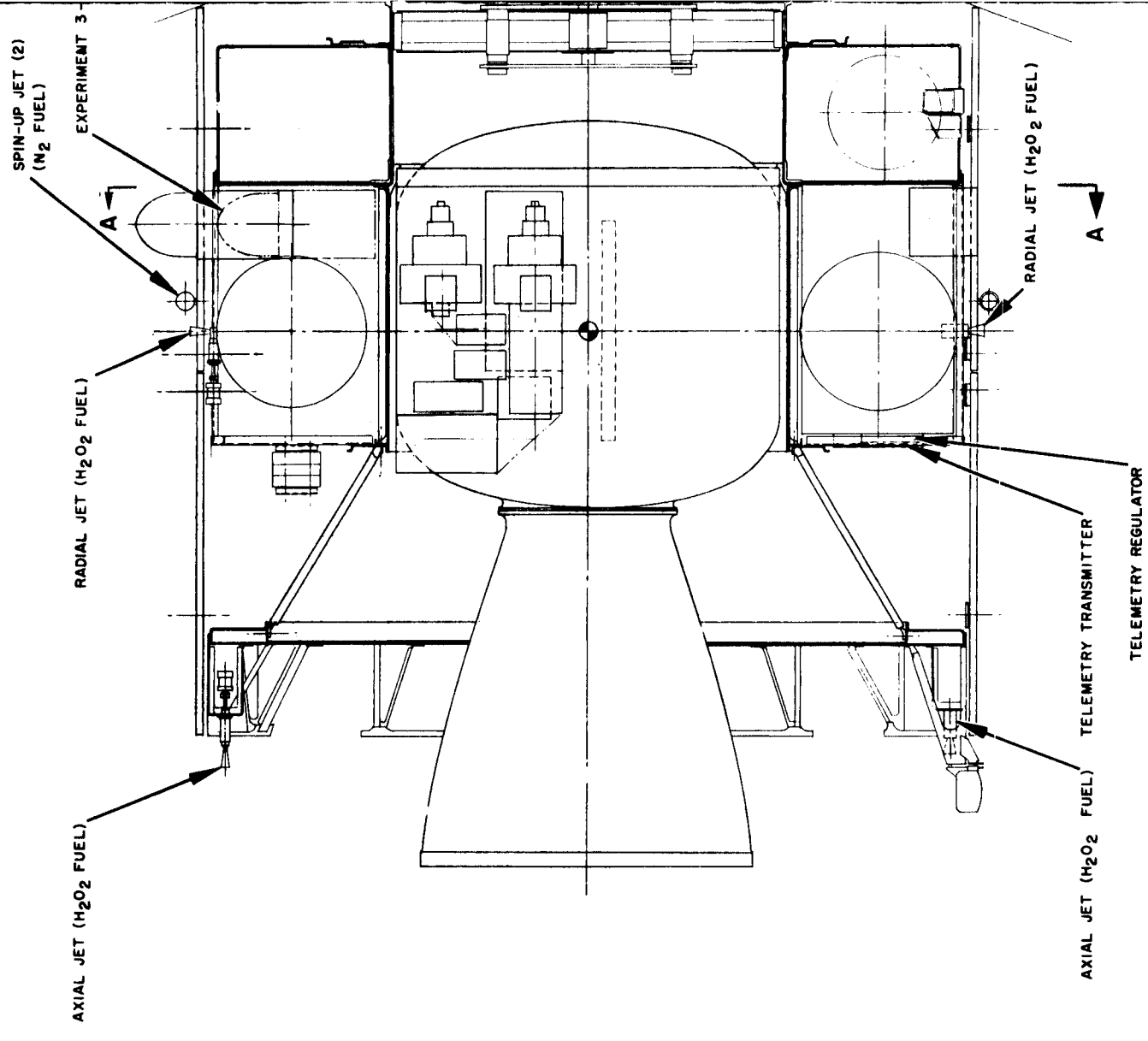


Figure 5-36. General Arrangement, Synchronous Altitude Gravity-Gradient Experiment

toward mass property distribution control is necessary and is planned to prevent exceeding the maximum spacecraft weight and to increase the roll-to-pitch ratios prior to deployment of gravity-gradient stabilization booms. To date, studies of moving the apogee motor aft (towards the separation plane) indicate that a significant increase in roll-to-pitch ratios can be realized:

<u>Aft Movement, inches</u>	<u>Roll-to-Pitch Ratios</u>	
	<u>At Station</u>	<u>At Separation</u>
2	1.02	1.04
3	1.03	1.08
4	1.04	1.08

Table 5-16 lists a weight breakdown for the complete SAGGE satellite. The ΔW values shown are changes in weight since the last report and as such reflect the areas where redesign has occurred or where better weight estimates have been made. Detailed changes in the weight distribution which reflect the current spacecraft configuration are as follows:

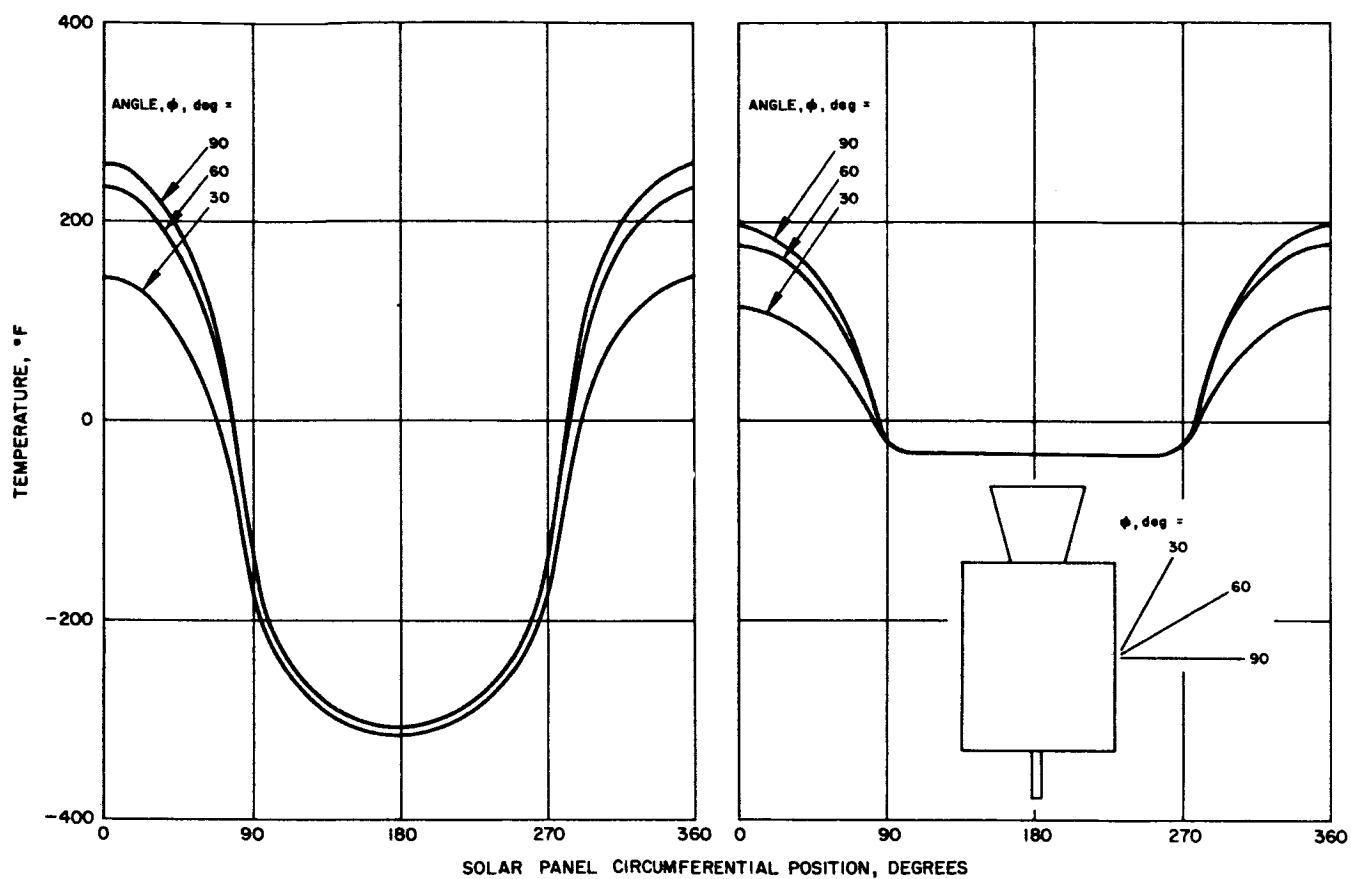
<u>Description of Change</u>	<u>Weight Change, pounds</u>
Basic spacecraft	(19.6)
See Table 5-12	+19.6
Miscellaneous subsystem	(+23.9)
Nutation damper - formerly listed under basic spacecraft	+ 2.0
Thermal barrier - estimate increased; for- merly listed in basic spacecraft	+ 6.0
Thermal insulation - added to spacecraft under solar panels, ground planes, and thermal barrier	+15.9
Gravity-gradient subsystem	(+36.5)
"X" booms - miscellaneous weight change	- 0.1
Damper boom - reduction in tip mass	- 3.6
Retainer and supports - revised estimate based on moving damper to aft end of spacecraft	-32.8
Control subsystem	(-27.4)
Free-body spinup	+ 4.3
Revised weight on associated system components	
Initial station placement	-19.5
H ₂ O ₂ system incorporated in lieu of bipropellants	

<u>Description of Change</u>	<u>Weight Change, pounds</u>
Orbit inclination	- 8.0
System requirement deleted	
180-degree inversion	- 5.2
Valveless system utilizing a subliming solid incorporated in lieu of pulsed plasma jet system	
E-W stationkeeping	+ 1.0
Single jet subliming solid incorporated in lieu of four pulsed plasma jets	
Payload	
Meteorological package	(+ 5.3)
Camera hi-resolution – revised estimate based on updated information	+ 1.4
Installation hardware – revised estimate	+ 3.9
Final orbit condition (booms deployed)	(-15.1)
Propellant E-W stationkeeping – estimate based on new system requirement over old system	+ 9.0
Propellant orbit inclination Requirement deleted	-35.0
Total at station (prior to despin)	(-41.1)
Propellant H ₂ O ₂ – estimate based on new system requirement over old system	- 5.6
Total at spinup (prior to apogee fire)	(-46.7)
Total at separation from booster	<hr/> -46.7

Table 5-17 illustrates by sequence from launch through orbit the mass property distribution of the SAGGE spacecraft. Table 5-18 presents a weight breakdown of the alternate payload for this spacecraft.

Thermal Analysis and Design

The thermal analysis of the solar panels for the gravity-gradient stabilized vehicle has continued. The expected circumferential temperature distribution is shown for solar angles of 30, 60, and 90 degrees in Figure 5-37 for the insulated and noninsulated configuration respectively. Because of the very high expected internal structural temperature gradients in the radial direction inherent in the noninsulated design it is most probable that the insulated panel concept will be utilized. With the insulated concept, the



a) No internal radiation

b) With internal radiation

Figure 5-37. Solar Panel Temperature Distribution versus Solar Angle

TABLE 5-16. SYNCHRONOUS ALTITUDE GRAVITY-GRADIENT
SPACECRAFT WEIGHT BREAKDOWN

Description	ΔW	Weight, pounds
Electronics subsystem		87.2
Wire harness subsystem		33.0
Solar panel subsystem		58.1
Structure subsystem		82.8
Miscellaneous subsystem		14.4
Basic spacecraft	(+19.6)	(275.5)
Apogee motor (fired)		(102.6)
Miscellaneous subsystem	(+23.9)	(23.9)
Nutation damper (2)	+ 2.0	2.0
Thermal barrier	+ 6.0	6.0
Thermal insulation	+15.9	15.9
Gravity-gradient subsystem	(-36.5)	(81.9)
"X" booms	- 0.1	50.0
Libration damper	- 3.6	16.7
Retainer and supports	-32.8	15.2
Controls subsystem	(-27.4)	(46.8)
Free body spinup	(+ 4.3)	(19.3)
Tanks (2) and miscellaneous components	+ 4.0	13.8
Jets and miscellaneous components	+ 0.3	5.5
Initial station placement	(+19.5)	(14.5)
Tanks (2)	-11.7	10.6
Jets and miscellaneous components	- 7.8	3.9
Orbit inclination	(- 8.0)	(0)
180-degree inversion	(- 5.2)	(8.0)
Tanks (4)		6.0
Jets (2)		2.0
E-W stationkeeping	(+ 1.0)	(5.0)
Tank (1)		4.0
Jet (1)		1.0
Payload	(+ 5.3)	(114.8)
Radiation and micrometeorite detection package (1)		25.5
Meteorological package	(+ 5.3)	(57.3)
Camera - lo-resolution (1)		8.1
Camera - hi-resolution (1)	+ 1.4	14.7

TABLE 5-16. (continued)

Description	ΔW	Weight, pounds
IMC and IMC electronics		2.2
Camera electronics (2)		13.6
Sequence timer (2)		8.0
Flasher (2)		1.8
Installation hardware	+ 3.9	8.9
Gravity-gradient package		(32.0)
Camera		8.5
RF sensor		10.8
IR sensor		4.0
Solar sensor		4.0
Installation hardware		4.7
Battery power supply subsystem		(34.6)
Batteries		27.3
Supports		7.3
Final orbit condition	(-15.1)	(680.1)
Propellant E-W stationkeeping	+ 9.0	9.0
Yo-Yo despin mechanism		10.0
Propellant orbit inclination	-35.0	0
Total at station, prior to despin	(-41.1)	(699.1)
Propellant - H_2O_2	- 5.6	42.0
Propellant - apogee motor		752.0
Expendables - apogee motor		20.0
Total at spinup, prior to apogee fire	(-46.7)	(1513.1)
Propellant - cold gas spinup		6.1
Total at separation from booster	(-46.7)	1519.2

large gradients are expected to be contained in the solar panels only and consequently, further efforts have been made to reduce the large temperature excursions to a minimum. If this can be accomplished, the solar panel output will be increased due to lowered temperature on the illuminated side of the spacecraft and nonilluminated side solar panel temperature will be increased. Several methods of approach are being considered. They are as follows:

- 1) Addition of conduction around vehicle
- 2) Addition of change of phase material to panels
- 3) Addition of a circulating fluid
- 4) Increase in power by adding extendible panels

TABLE 5-17. SYNCHRONOUS ALTITUDE GRAVITY-GRADIENT
SPACECRAFT MASS PROPERTY DATA

	Current Weight, pounds	J, inches	I_j , slug-ft ²	I_i , slug-ft ²	I_k , slug-ft ²
Final orbit condition (booms deployed)	680.1	21.19	13,978	2,709	12,761
	Current Weight, pounds	Z, inches	I_z , slug-ft ²	I_x , slug-ft ²	I_y , slug-ft ² R/P
Total at station (prior to despin)	699.1	21.64	70.5	64.6	69.8 1.01
Total at spinup (prior to apogee fire)	1513.1	22.42	91.6	85.5	87.0 1.05
Total at separation from booster	1519.2	22.36	92.2	86.3	87.5 1.05

TABLE 5-18. SYNCHRONOUS ATTITUDE GRAVITY-GRADIENT ALTERNATE PAYLOAD WEIGHT BREAKDOWN

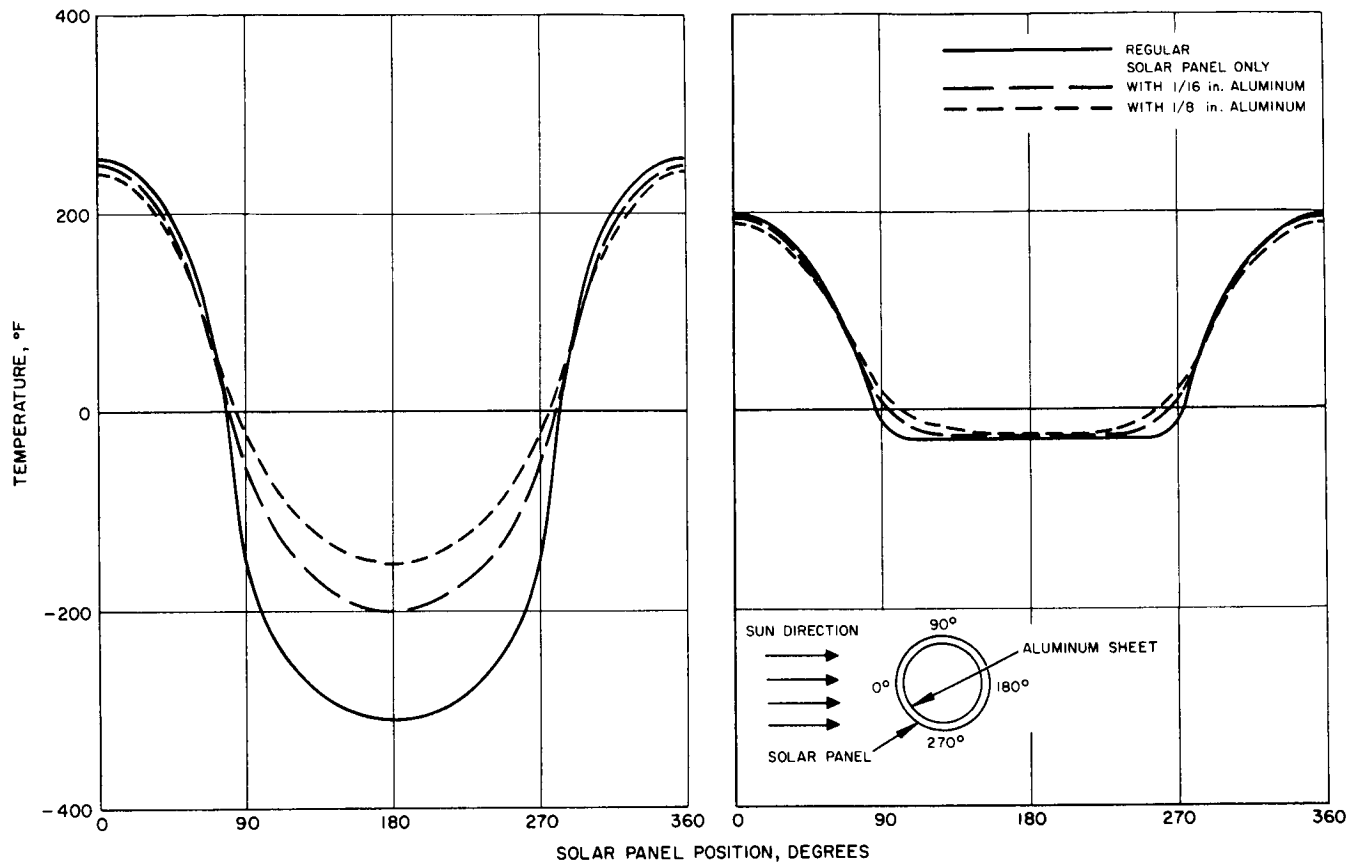
Description	Weight, pounds
RF propagation experiment	(23.0)
Transponder	15.7
Traveling-wave tube	3.5
Traveling-wave tube power supply	2.5
Installed hardware and miscellaneous	1.3
Nuclear arms control package	(25.0)
Gravity-gradient package (Same as Table 5-16)	(32.0)
Total	80.0

The addition of conduction around the vehicle in the form of aluminum sheet has been studied for three solar panel configurations varying from a regular solar panel to a solar panel backed with up to 1/8 inch of aluminum for the purpose of conducting thermal energy to the nonilluminated regions of the panels. Results shown in Figure 5-38 indicate that the addition of even 1/8 inch aluminum backing to the panels reduces the maximum temperature by only 16° F for the insulated panel configuration. The cold side panel temperature, although apparently not as important at this time, is increased significantly from -310° F to 155° F. All of this is at the expense of approximately 140 pounds of aluminum to the spacecraft.

By adding a material to the back side of the solar panels that could undergo a change of phase during the daily solar cycle, there exists the possibility of reducing the temperature excursions at both the maximum and minimum ends. This is currently being investigated with the use of water storage. Water is a natural contender for this application because of the large thermal capacity in the liquid state and the very high heat of fusion (144 Btu/lb) in passing from the liquid to solid state. This concept will also involve the addition of considerable weight to the vehicle.

A concept of circulating a fluid from the warm to cold solar panels could also accomplish the desired end of reducing maximum solar panel temperature. This is currently being analyzed as to weight and center of gravity displacement penalties associated with this concept.

A method of increasing the spacecraft power by adding extendible solar panels is also under consideration. The added panels would be at the



a) Insulated solar panel

b) Noninsulated solar panel

Figure 5-38. Solar Panel Temperature Distribution versus Circumferential Conduction

forward end of the spacecraft and would logically run at a lower temperature excursion than the regular spacecraft panels since the added panels would be designed to transfer energy from the back surface to space and directly to the cooler panels by radiation.

The thermal analysis of the internal temperature distributions of the gravity-gradient vehicle has continued. The assumed analytical model includes solar panels, radial ribs, and an inner ring of structure. Results have yielded approximations of the expected vehicle internal mounting surface temperature distributions for a variety of parametric conditions. A complete tabulation of the results are shown in Figure 5-39. The model shown in the figure has been analyzed for various solar panel-vehicle thermal coupling, solar angles ranging from 30 to 90 degrees, and inclusion of internal packages at various mounting locations, mounting conductances, package insulations, and internal power dissipations. In general, it has been found that with the open spacecraft configuration, i. e., no insulation on solar panels, the vehicle structure will sustain temperature gradients from hot to cold side of approximately 270° F. With the use of thermal decoupling of solar panels from structure through low emittance surface treatment, this gradient can be reduced to the 60 to 100° F range. With higher decoupling, i. e., superinsulation, it is felt that the total temperature excursions of mounting surfaces can be reduced to the 20 to 40° F range. A preliminary conclusion of this analysis is that an insulation between the solar panels and structure will be required to sustain reasonable temperature conditions in the gravity-gradient vehicles. A corollary conclusion is that end plane insulation will probably be required to maintain satisfactory temperature levels at the lower sun angles since internal power dissipation becomes very low at the low sun angles for the gravity-gradient configuration.

The thermal analysis assumes zero thermal conduction between the solar panels and structure with radiation as the only mode of energy transfer. By the nature of the simple model it is also necessary to neglect end effects on the structural temperature distribution. It is felt, however, that the results are very valid for conceptual design purposes.

Electrical Power System – Medium Altitude, Gravity-Gradient Configuration

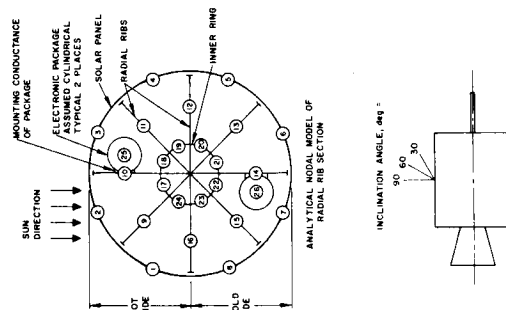
System Design

The system description, presented under the discussion of system design, is also valid for the medium altitude vehicle. Battery curves for the medium altitude case are shown in Figures 5-40 through 5-42.

Run No.	Date	No. Nodes	Emissivities of Internal Surfaces*								External Emissivity Cell Side	Sun Inclination Angle, Degrees			Mounting Conductance			Electronic Package Power Input, Watts		Temperatures °F							
			Surfaces*									30	60		90	Hard 0.3	Soft 0	Hot Side Node 25	Cold Side Node 26	Solar Panel		Structure		Electronic Package			
			1	9	24	16	25	26	Maxi-mum	Mini-mum			Maxi-mum	Mini-mum						Hot Side	Cold Side						
1	12-5	24	0.8	0.3	0.3	0.3	—	—	—	1.0	✓	✓	✓	—	—	—	—	192	-197	174	-112	—	—	—	—		
2	12-5	24	0.8	0.8	0.8	0.8	—	—	—	1.0	✓	✓	✓	—	—	—	—	182	-160	160	-102	—	—	—	—		
3	12-11	24	0.8	0.8	0.8	0.8	—	—	—	0.82	✓	✓	✓	—	—	—	—	212	-133	190	-80	—	—	—	—		
4	12-11	24	0.8	0.8	0.8	0.8	—	—	—	0.82	✓	✓	✓	—	—	—	—	187	-142	166	-90	—	—	—	—		
5	12-11	24	0.8	0.8	0.8	0.8	—	—	—	0.82	✓	✓	✓	—	—	—	—	103	-174	82	-125	—	—	—	—		
6	12-17	24	0.01	0.8	0.8	0.8	—	—	—	0.82	✓	✓	✓	—	—	—	—	237	-285	87	72	—	—	—	—		
7	12-17	24	0.01	0.8	0.8	0.8	—	—	—	0.82	✓	✓	✓	—	—	—	—	213	-291	67	53	—	—	—	—		
8	12-17	24	0.01	0.8	0.8	0.8	—	—	—	0.82	✓	✓	✓	—	—	—	—	126	-312	-1	-7	—	—	—	—		
9	12-18	24	0.05	0.8	0.8	0.8	—	—	—	0.82	✓	✓	✓	—	—	—	—	233	-211	111	48	—	—	—	—		
10	12-18	24	0.05	0.8	0.8	0.8	—	—	—	0.82	✓	✓	✓	—	—	—	—	208	-220	90	31	—	—	—	—		
11	12-18	24	0.05	0.8	0.8	0.8	—	—	—	0.82	✓	✓	✓	—	—	—	—	123	-250	17	-29	—	—	—	—		
12	12-27	25	0.05	0.8	0.8	0.8	0.3	—	—	0.82	✓	✓	✓	✓	—	10	—	235	-194	161	83	189	—	—	—		
13	12-27	25	0.05	0.8	0.8	0.8	0.05	—	—	0.82	✓	✓	✓	✓	—	10	—	235	-194	164	83	233	—	—	—		
14	12-27	25	0.05	0.8	0.8	0.8	0.3	—	—	0.82	✓	✓	✓	✓	—	5	—	234	-202	138	67	152	—	—	—		
15	12-27	25	0.05	0.8	0.8	0.8	0.05	—	—	0.82	✓	✓	✓	✓	—	5	—	234	-202	140	67	176	—	—	—		
16	12-28	26	0.05	0.8	0.8	0.8	0.3	0.3	0.82	—	✓	✓	✓	✓	—	5	5	234	-189	150	98	114	164	—	—		
17	12-28	26	0.05	0.8	0.8	0.8	0.3	0.3	0.82	—	✓	✓	✓	✓	—	10	10	236	-171	182	137	206	165	—	—		
18	1-2	25	0.05	0.8	0.8	0.8	—	0.3	0.82	—	✓	✓	✓	✓	—	—	5	233	-197	125	79	—	99	—	—		
19	1-2	25	0.05	0.8	0.8	0.8	—	0.3	0.82	—	✓	✓	✓	✓	—	—	10	234	-185	138	103	—	142	—	—		

*Typical in Every Sector.

Figure 5-39. Summary of Results of Internal Radial Temperature Distribution Analysis for Gravity-Gradient Vehicle



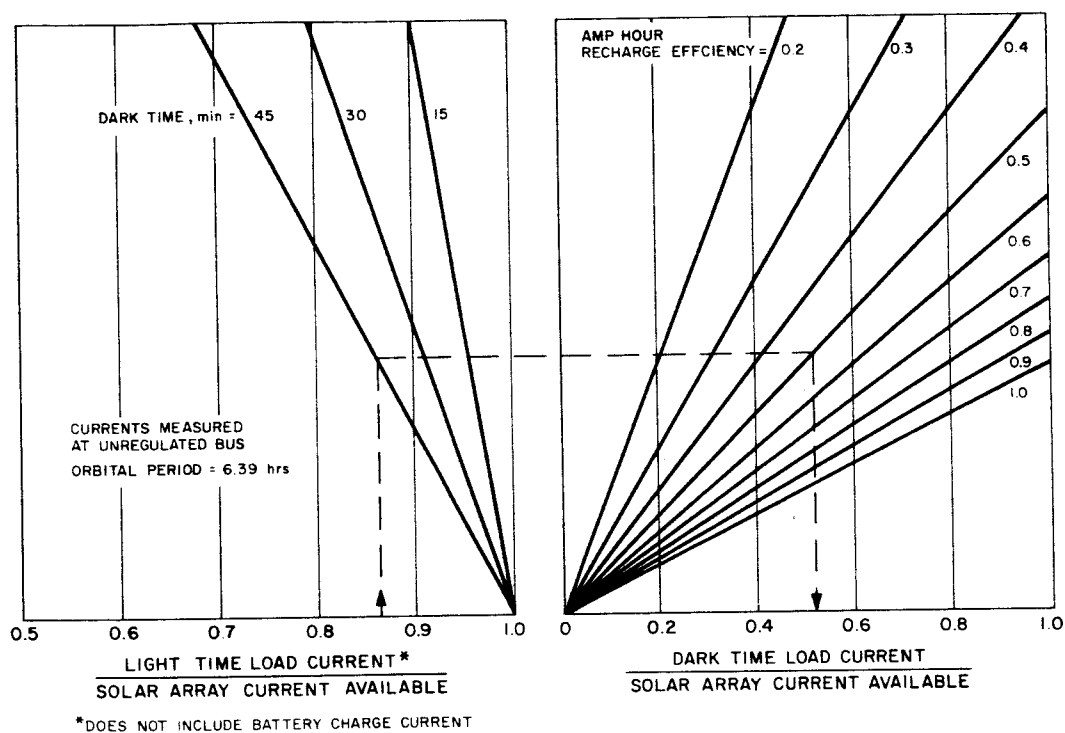


Figure 5-40. Electrical Load Capability—Solar Array and Rechargeable Batteries
Circular orbit: 6000 n.mi. altitude

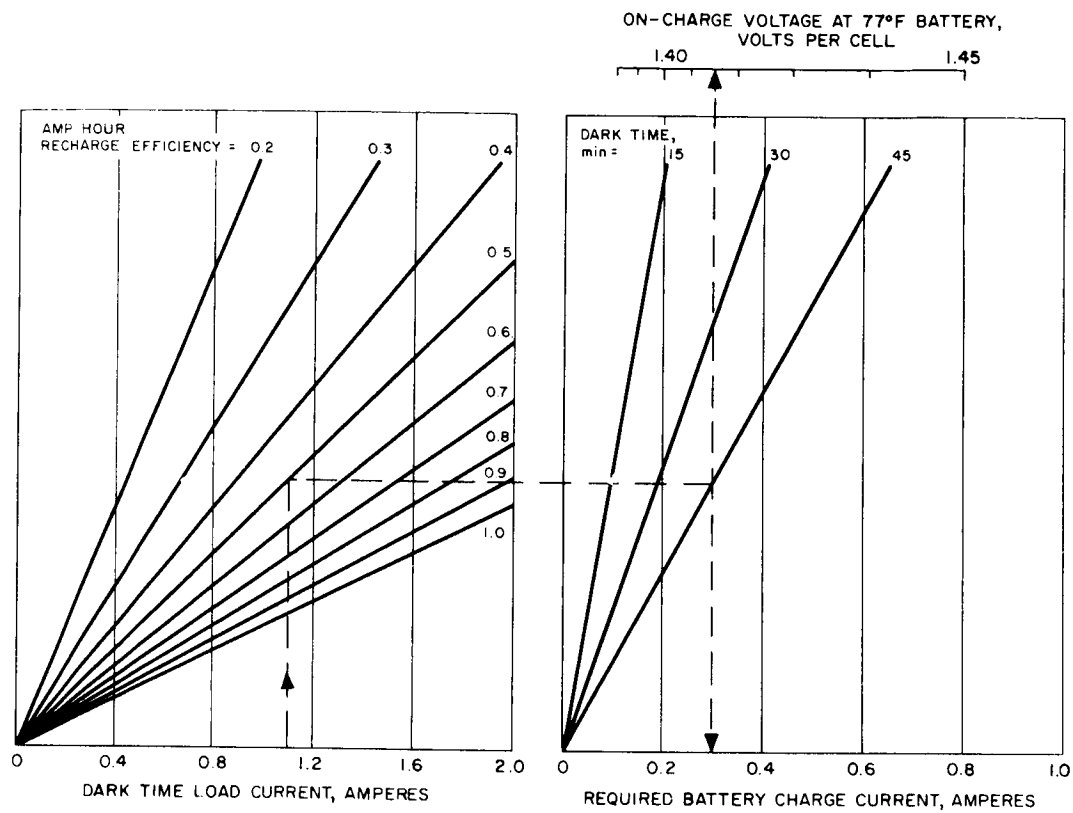


Figure 5-41. Recharge Current Requirements
Circular orbit: 6000 n.mi. altitude

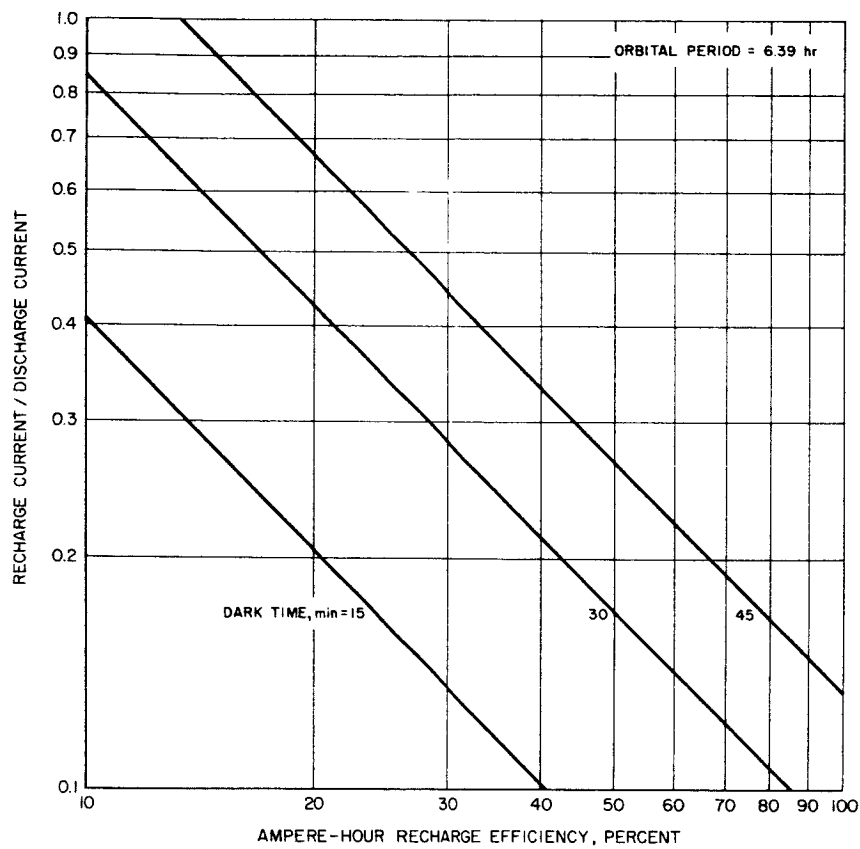


Figure 5-42. Ratio of Recharge Current to Discharge Current for 6000 n.mi. Altitude

Reaction Control System

An initial tradeoff study report for the MAGGE reaction control system has been issued. Additional studies are underway to determine the relevant properties of various materials for use in the MAGGE valveless subliming solid engine. A preliminary evaluation of a simplified active attitude control system for the MAGGE eccentricity maneuver has been initiated in an attempt to reduce the time required to perform this maneuver.

The hydrogen peroxide system specification has been prepared and will undergo finalization during the next report period. Subliming solid system specifications are being prepared.

Structure and Spacecraft Configuration Design

The medium altitude gravity-gradient design utilizes the T-2 structure common to the two synchronous altitude configurations with modifications to the center thrust tube to install the DeHavilland variable angle boom system and the meteorological experiment tape recorder in the cavity vacated by the apogee motor.

General Arrangement

Detailed packaging layouts have been made with an eye to maximum packing density as well as identical, or at least similar, packaging of components in SAGGE and SASSE. The greater payload space in MAGGE permitted efficient packing with little or no revision of the basic Advanced Syncom structure. Inclusion of the DeHavilland variable angle boom system does not seriously impair the packaging capacity of the MAGGE.

The maximum density configuration is detailed in Figure 5-43. A selected payload configuration is detailed in Figure 5-43. A selected payload configuration will be given in the next report.

Mass Properties

The effort for the medium altitude, gravity-gradient spacecraft (MAGGE) has been concerned with updating the weight estimates during the last reporting period. A detailed weight breakdown for MAGGE is shown in Table 5-19 together with the weight changes (Δw) since last reported. The justification for these changes is as follows:

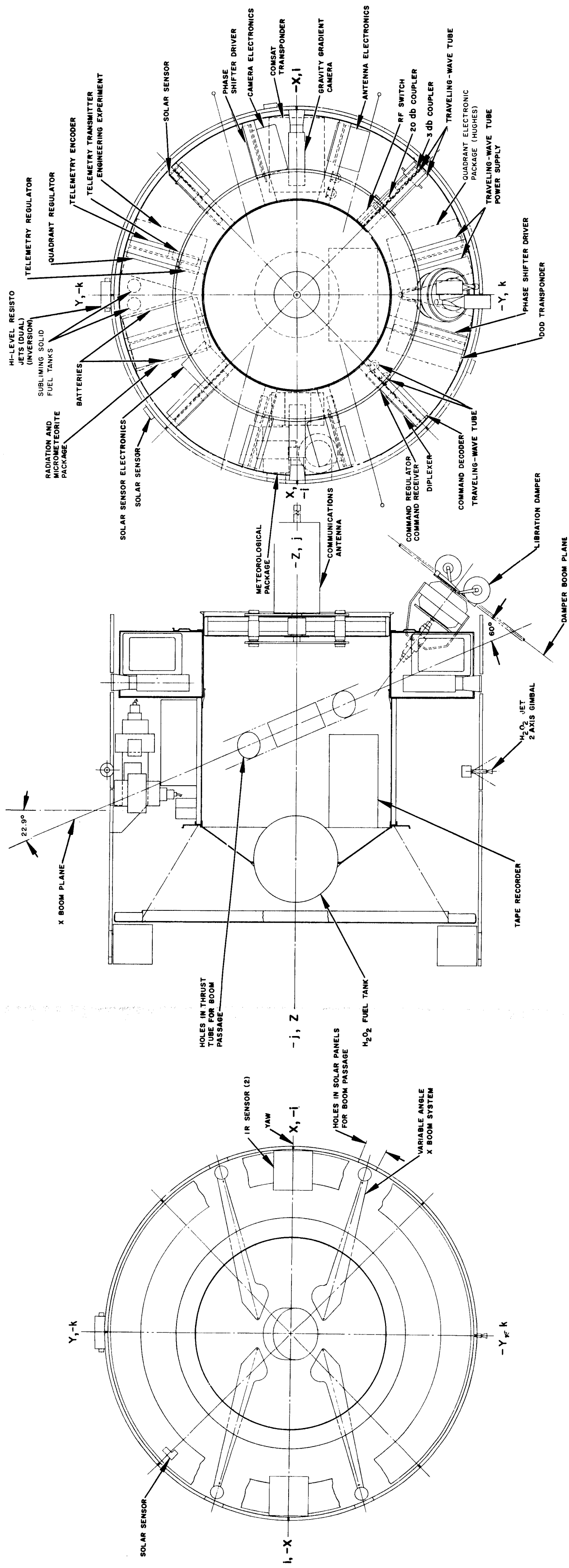


Figure 5-43. General Arrangement—Medium Altitude Gravity-Gradient Experiment

	Weight Change, pounds
Basic spacecraft	(+19.6)
See Table 5-12	+19.6
Wire harness subsystem	(+ 7.0)
Additional wiring over basic for the additional payload capability	
Miscellaneous subsystem	(+27.3)
Thermal barrier estimate increased; formerly listed in basic spacecraft	+11.4
Thermal insulation covering spacecraft under solar panels, ground planes, and thermal barrier. A new requirement.	+15.9
Gravity-gradient subsystem	(-22.0)
"X" booms - miscellaneous weight change	- 0.1
Damper boom - reduced tip mass	- 0.6
Scissor mechanism and supports - revised estimate based on moving damper to aft end of spacecraft	-21.3
Controls subsystem	(- 7.7)
Orbit and attitude control	+11.0
Incorporate a single jet, H ₂ O ₂ system in lieu of multiple system control	
180-degree inversion	- 6.7
Incorporate a subliming solid system in place of pulse plasma system	
Orbit inclination control	- 8.0
Replaced by H ₂ O ₂ system for spacecraft orbit and attitude control	
Orbit eccentricity	- 4.0
Replaced by H ₂ O ₂ system for spacecraft orbit and attitude control	
Payload	(+24.4)
Meteorological package	(+22.4)
New estimate for hi-resolution camera based on updated information	+ 1.4
Tape recorder requirement added to system	+16.0
Revised estimate	+ 5.0
Nuclear arms control package	- 1.0
Revised estimate	

	Weight Change, pounds
Engineering experimental package Revised estimate	+ 3.0
Final orbit condition	(+48.6)
H ₂ O ₂ - orbit and attitude control Revised estimate based on system requirement	- 8.0
Total at separation from booster	+40.6

TABLE 5-19. MEDIUM ALTITUDE GRAVITY-GRADIENT
WEIGHT BREAKDOWN

Description	ΔW	Weight, pounds
Electronic subsystem		87.2
Wire harness subsystem		33.0
Solar cell subsystem		58.1
Structure subsystem		82.8
Miscellaneous subsystem		14.4
Basic spacecraft	(+19.6)	(275.5)
Wire harness subsystem	(+ 7.0)	(7.0)
Miscellaneous subsystem	(+27.3)	(27.3)
Thermal barrier	+11.4	11.4
Thermal insulation	+15.9	15.9
Gravity-gradient subsystem	(-22.0)	(52.8)
"X" booms	- 0.1	20.0
Libration damper	- 0.6	6.1
Scissor mechanism and supports	-21.3	26.7
Controls subsystem	(- 7.7)	(17.5)
Orbit and altitude control	+11.0	11.0
180-degree inversion	- 6.7	6.5
Orbit inclination control	(- 8.0)	(0)
Resisto jet (2)	- 1.5	0
Tank	- 3.5	0
Lines plus fittings	- 1.3	0
Miscellaneous	- 1.8	0

TABLE 5-19. (continued)

Description	ΔW	Weight, pounds
Orbit eccentricity	(- 4.0)	(0)
Resistor jet (4)	- 3.0	0
Mounts	- 0.3	0
Lines plus fittings	- 0.7	0
Payload	(+24.4)	(248.4)
Department of Defense transponder		(31.5)
Transponder		24.0
Traveling-wave tube		2.5
Traveling-wave tube power supply		2.5
Diplexer		1.0
Installed hardware and miscellaneous		1.5
Meteorological package	(+22.4)	(74.4)
Camera - lo-resolution		8.1
Camera - hi-resolution	+ 1.4	14.7
Tape recorder	+16.0	16.0
IMC and IMC electronics		2.2
Camera electronics		13.6
Sequence timer		8.0
Flasher		1.8
Installation hardware	+ 5.0	10.0
Nuclear arms control package (1)	- 1.0	25.0
Engineering experimental package (1)	+ 3.0	28.0
Radiation and micrometeorite detection package (1)		25.5
Gravity-gradient package (2)		(64.0)
Camera		17.0
RF sensor		21.6
IR sensor		8.0
Solar sensor		8.0
Installation hardware		9.4
Battery power supply subsystem		(34.6)
Batteries		27.3
Supports		7.3
Final orbit condition	(+48.6)	(663.1)
H ₂ O ₂ - orbit and altitude control	- 8.0	27.0
Total at separation from booster	+40.6	690.1

Thermal Analysis and Design

The thermal analysis of the MAGGE system includes many of the same constraints as the SAGGE system. The exclusion of the apogee motor for this vehicle eliminates the potential problem of thermal barrier damage due to motor firing. The same general thermal design concept as on the SAGGE system will be utilized with the possible exception that an active thermal control device may be required on the end planes of the MAGGE. This same type of active thermal control may be required for the SAGGE but the possibility is greater that because of the larger inclination angle extremes with the MAGGE mission, this concept will be needed for satisfactory vehicle temperature control. A preliminary analysis of this potential requirement is in progress.

6. EXPERIMENTAL PAYLOADS

METEOROLOGICAL EQUIPMENT

Since the last report, the requirements for Iris control and direction control have been deleted. The required duty cycle for each type of spacecraft is listed below:

Spin-stabilized

Wide-angle picture every 30 minutes

Narrow-angle picture, maximum every minute, normal every 6 minutes

Flight 1 — no pictures of earth night

Narrow-angle pictures during earth night on Flight 2

Synchronous Gravity-Gradient

Wide-angle every 30 minutes

Narrow-angle, maximum every minute, normal every 6 minutes

Narrow-angle pictures during earth night; no pictures during satellite eclipse

6000-Mile Gravity-Gradient

Wide-angle picture every 20 minutes

Narrow-angle every 6 minutes

Pictures directly read out when in sight of station, recorded when not in sight of station and not in eclipse. Pictures in the record mode taken automatically from start sequence until tape recorder is full

Recorder playback at station

Telemetry points for the experiments are analog and 0 to 6 volts with 3- to 10-kilohm output impedance. The following points are required:

- Vidicon filament
- Video output
- High voltage power
- Focus current
- Iris setting
- 5 percent horizontal synchronization
- Vertical synchronization
- Electronics module temperature
- Camera temperature
- Recorder pressure
- Recorder temperature
- Channel 1 record
- Channel 2 record
- Channel 3 record
- Channel 4 record
- Motor inverter output
- Motor power

The required commands are:

- Normal picture taking sequence
- Direct picture taking sequence
- Start sequence
- Camera 1 ON
- Camera 1 OFF
- Camera 2 ON
- Camera 2 OFF
- Initiate shutter
- Bypass recorder
- Playback recorder

IMC will require additional telemetry points (approximately 8 to 10) and commands. However, the tape recorder will be deleted, releasing some commands and telemetry points.

RADIATION AND MICROMETEORITE DETECTION EQUIPMENT

Detailed definition of the radiation and micrometeorite equipment is continuing. The detection equipment on each of the three spacecraft, SASSE, SAGGE, and MAGGE, will vary slightly according to subsequent definition of spacecraft missions.

A tentative list of the measurements to be performed on each spacecraft with approximate weight, volume, window size, power, and tentative vendor is given below:

MAGGE

- 1) Energetic particle measurements
 - a) Silicon P-N junction detector for protons $0.5 \text{ meV} \leq E \leq 5 \text{ meV}$ mounted looking aft through ground plane. (1/2 pound, $3\text{-}1/2$ by $3\text{-}1/2$ by 1 inches, 1-inch diameter, 0.180 watts UCSD)
 - b) Omnidirectional scintillation counter for electrons, $E \geq 1.5 \text{ meV}$ (3/4 pound, 16 in^3 , 3/4-inch diameter, 1/2 watt UCSD)
 - c) Set of four silicon P-N junction detectors, identical except for shielding, with three ranges each; for electrons $0.25 \text{ meV} \leq E \leq 2.5 \text{ meV}$; for protons $3 \text{ meV} \leq E \leq 20 \text{ meV}$, and alpha particles, $14 \text{ meV} \leq E \leq 80 \text{ meV}$. (3 pounds, in^3 , three 2.5-inch squares, 2.5 watts BTL)
 - d) Plasma probe (Faraday cup) sensitive to protons, $20 \text{ eV} \leq E \leq 5 \text{ keV}$ in eight ranges (2 pounds, in^3 , 4.5-inch diameter hole, 1 watt BTL)
 - e) Ion chamber to measure interior spacecraft environment (Dosimeter) (1 pound, in^3 , no window required, 1 watt, BTL)
- 2) Magnetic field measurement to frequency range: 0.05 cps to 0.5 cps, deviation down to 1 gamma. (1 pound, in^3 , 1 watt, BTL) Note: Ideally this experiment should be boom-mounted. The desirability of including the experiment inside the spacecraft is still being evaluated.
- 3) Radiation damage panel, solar cell measurements: various shield thicknesses and compositions; adhesives. (4 pounds, in^3 , 4 by 7 inches, 3 watts, GSFC)
- 4) Micrometeoroid counting and erosion: (3.3 pounds, in^3 , 7 by 7-inch transparent plate, 1 watt, GSFC) Note: This experiment if flown will result in a transparent plate being installed on the outside of the solar panels.

SASSE

Same as MAGGE except the magnetometer will be placed inside the spacecraft and the micrometeoroid experiment will be deleted.

SAGGE

Same as MAGGE with an additional two fast neutron detectors, one facing toward the earth with the other facing away. (1-1/2 pounds, in³, two 1-inch diameter holes, 1 watt, GSFC)

The package will transmit the information via a Hughes telemetry transmitter. It is expected that the equipment (including transmitter) will be required to operate one orbit per day on MAGGE and 5 minutes every hour on SASSE and SAGGE. An exception to the operating schedule will occur during major solar flare activity when continuous operation will be required for approximately 2 days. Major solar flares (3 and 3+ magnitude) are expected to occur during the years 1967 to 1968 at a statistical rate of approximately one per month.

Turn on/Turn off ground commands will be required for each separate measurement. This is required to prevent loss of the entire package because of a short-to-ground in one measurement circuit.

The package will plug into the spacecraft standard harness and occupy no more than a quadrant's volume (11 by 8 by 18 inches) with the exception of one fast neutron detector which will be located 180 degrees away from the package, and of the miniaturized silicon P-N junction detector for protons (1-a) which will be placed in the rib area above the quadrant package.

The MAGGE and SASSE package will draw 15.18 watts (after regulation) while the SAGGE package will draw 16.18 watts (after regulation) excluding telemetry transmitter. The package will require a 10 by 10-inch aperture in the solar panel adjacent to the quadrant package. Details of this window are shown in Figure 6-1.

NAVIGATION EXPERIMENT

A navigation system based on low-inclination synchronous satellites in which a user can determine his position by means of only one satellite in a passive mode (i. e. , no transmitting from the user) can be instrumented in accordance with either of the following concepts:

- 1) Satellite azimuth and elevation.
- 2) Satellite range and azimuth.

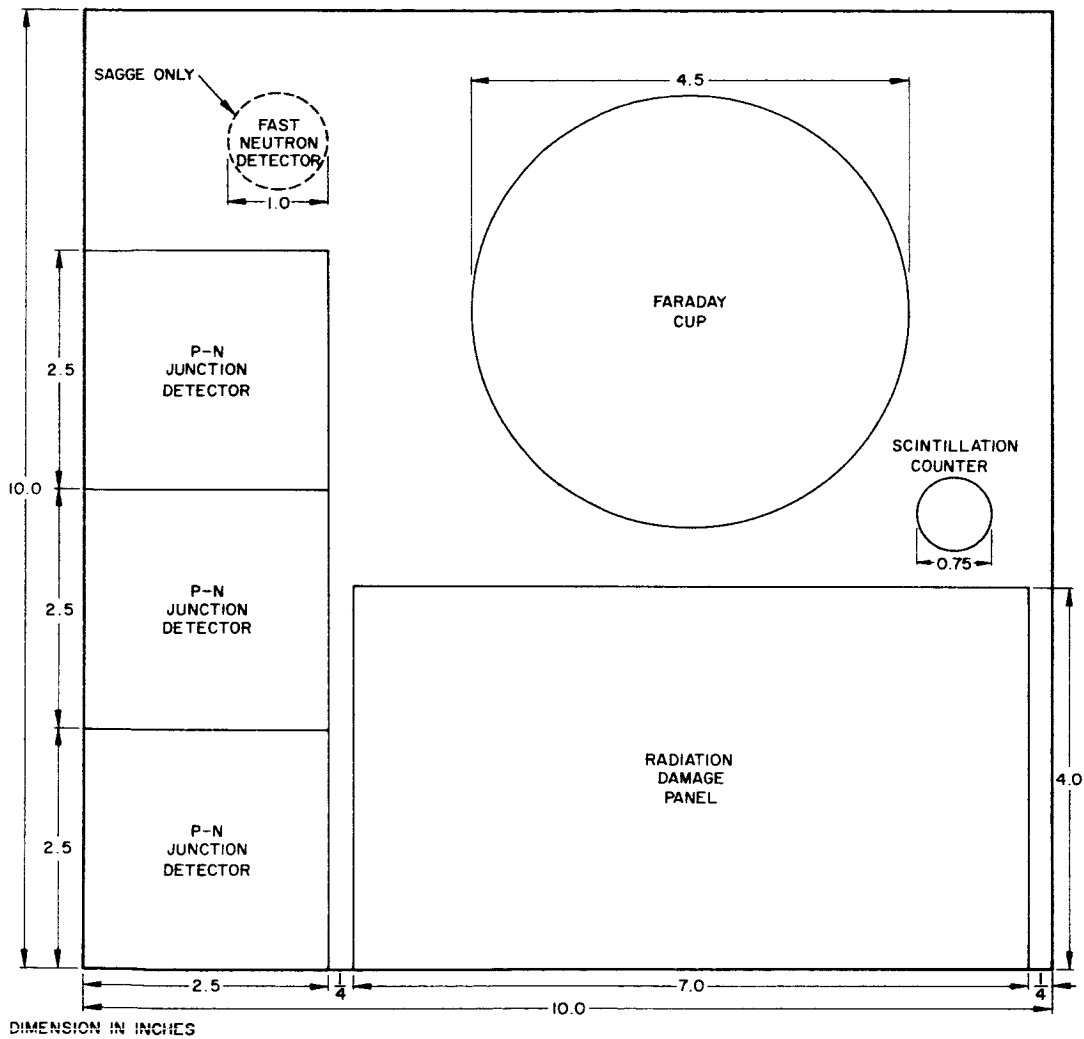


Figure 6-1. Sensor Window

The first option listed involves two angle measurements. The difficulty in obtaining accurate angle measurements and referencing them to a local vertical and north reference presents formidable problems. For the second option, to preclude transmission by the user would involve the utilization of clocks with accuracies in the range of 10^{12} .

NUCLEAR ARMS CONTROL EQUIPMENT

From the standpoint of detection, the environments in which nuclear explosions are possible can be divided into three categories: subsurface (underground or underwater), surface to lower atmosphere, and space. The second category, surface to lower atmosphere, will be discussed below.

For blast detection with a satellite based system, the following reactions should be explored:

- 1) Radiation phenomena
 - Thermal X-rays (more than 50 percent of blast energy)
 - Gamma rays
 - Neutrons
 - Beta particles (electrons)
- 2) Acoustic phenomena
- 3) Electromagnetic pulse (radio signal)
- 4) Visible light and air fluorescence
- 5) Infrared radiation

The most positive indication that a nuclear explosion has occurred is identification of an increase in flux of the radioactive particles previously listed. A satellite-based technique at synchronous and medium altitudes, however, suffers two severe constraints in this application.

- 1) The high background radiation at medium and synchronous altitudes saturates the sensitive detectors.
- 2) Soft thermal X-rays (comprising more than 50 percent of the blast energy) are absorbed by the atmosphere when the blast is 5 miles or less in altitude. In addition, in shielded blasts in

which the nuclear device is surrounded by a thin sheet of lead or other material, the amount of radiation emitted is sharply reduced. Such a shield is particularly effective for thermal X-rays.

The satellite-based detection techniques at the altitudes considered here present difficult problems, and there is no evidence that a foolproof system is possible. At these altitudes natural radiation might produce signals similar to, and thus tend to mask, those from a nuclear explosion.

The blast wave produced by an explosion in air degenerates into an ordinary sound wave which propagates outward to considerable distances. In a homogeneous atmosphere, the amplitude of the air pressure wave scales approximately as the cube root of the yield and inversely as the distance from the blast point. However, the observed amplitude is strongly affected by the state of the atmosphere, so that it may be larger or smaller by a factor of five than is predicted by simplified scaling.

At present the most sensitive microbarographs of special design are sensitive to pressure changes of the order of $0.1 \text{ dyne per cm}^2$, or about 10^{-7} of normal atmosphere pressure. With this instrument and ideal meteorological conditions along the path, a 1-Kiloton blast could be detected about 1000 miles away. This is a factor six below the MAGGE orbit, and of 22 below the SAGGE orbit. In addition, volcanic and meteoric explosions and sonic booms resemble the acoustic waves from nuclear explosions and therefore increase the problem of detecting explosions by the acoustic method.

The electromagnetic pulse, with frequencies lying mainly in the range of 10 to 15 kc, resulting from asymmetric emission of gamma rays accompanying a nuclear explosion, has been suggested as a means of detecting such explosions. The major disadvantage to this radio detection method is that of lightning flashes producing signals (static) in about the same frequency range as the pulse signal from the explosion. Close to point of burst, the characteristics are different from those caused by lightning, but at distances over 600 miles away, they are essentially indistinguishable with presently available equipment. Until more sophisticated equipment is available which provides automatic exclusion of much of the static from lightning, the radio detection method will have an unacceptably high "false alarm" rate.

The visible light from a nuclear explosion offers a means of detection because under excellent meteorological conditions, it is theoretically possible to see a 1-megaton order blast about 200,000 miles in the daytime and a factor of 10 or more greater at night. Unfortunately, cloud cover between the blast and the observation point will render the method useless. It is useful, however, to carry this discussion one step forward. It is assumed that a satellite based detection system is not the only detection

system in operation, and that its compiled data is compared to that of ground based stations operating on any of the other schemes mentioned. Using cloud cover to hide the visible radiation leaves the explosion open to detection by even more positive methods. Clouds become saturated with radioactive particles and subsequently move in a random fashion and, presumably, into the detection range of a ground based radiation detection station. In addition, a dangerous radiation hazard is created in terms of fallout to any area over which the clouds pass. It appears that an optical sensing device is feasible in a satellite based detection scheme. The experimenter will determine the specific type of device, keeping in mind that the light flash under consideration exists for approximately 1 microsecond.

The final item listed as a basis for a possible detection scheme is the infrared effect. The large fireball formed in the brief period following detonation is essentially a black-body radiator at approximately 10^7 Kelvin. An IR detector in the orbits described appears to form a plausible scheme. The apparent disadvantages are cloud cover attenuation, very short observation time (1 microsecond), and the noise problem.

It appears from the foregoing that an optical device of some sort offers the most feasible solution at this time. With this in mind the following recommendations can be made:

- 1) Inclusion of the experiment on the medium altitude version because of the 3.8 distance factor.
- 2) Inclusion of the experiment on the same spacecraft as the meteorological experiment.
- 3) Inclusion on the same spacecraft as the radiation experiment.

MECHANICALLY DESPUN ANTENNA

The mechanically despun antenna will be furnished by NASA/GSFC. The unit is currently on a multiple solicitation procurement bid. The complete antenna unit will weigh approximately 16 pounds and utilize approximately 17 watts of power. The command and stepping circuits will be compatible to the current PACE system. The antenna will mate to the same cruciform as the phased array antenna.

SPACECRAFT ENGINEERING INSTRUMENTATION EXPERIMENT

Two versions of the spacecraft engineering experiment will be flown. One version will be flown on the first of the spin-stabilized satellites to be launched, while the other will be flown on the medium

altitude gravity-gradient stabilized vehicle. Both versions will carry equipment necessary to determine vibration levels to which the spacecraft is subjected and enough thermal sensors to accurately evaluate the thermal models being used in analysis.

In addition, the payload carried on the spin-stabilized vehicle will:

- 1) Allow telemetry and command to be transmitted over the communication link.
- 2) Provide a buffer unit to sample phased-array antenna drive signals for telemetering over the communication link.
- 3) Carry an infrared earth sensor especially designed for use on a spin-stabilized vehicle.

7. GROUND HANDLING AND SERVICING EQUIPMENT

SEMI-AUTOMATIC SYSTEM TEST EQUIPMENT RECORDING SYSTEM

With the semiautomatic recording subsystem of the system test equipment (STE), it is possible to obtain X-Y plots, strip-chart recordings, digital printouts, and magnetic tape recordings of all pertinent engineering data.

One immediate problem arises concerning analog scale factoring of meter voltages. Some test equipment presents ramp voltages from 0 to 1 volt for recording purposes. This ramp voltage is repeated for each scale setting of the meter such that a method of distinguishing the meter scale setting is necessary for automatic recording purposes. The following test equipment must have scale distinguishing provisions:

RMS voltmeter	HP 3400A
Power meters (2)	HP 431B
Calorimeter	HP 434A
RF voltmeter	Boonton 91D

Scale factoring is of particular interest concerning the X-Y recorder. For meaningful X-Y plots, the curves must be continuous and the X-Y recorder inputs must be proportional to the signal to be recorded. (Offset voltages must be supplied for each scale change of the recording instruments listed above).

Two methods of X-Y recording are repeatedly incorporated in Advanced Syncom system test. One method, shown in Figure 7-1, has two analog voltages from test instruments which are amplified in logarithmic converters and scale factored before recording on the X-Y plotter. The second method consists of one analog input and one digital input to the recording subsystem (Figure 7-2). The analog signal is treated by the logarithmic converter and scale factoring circuits as in method one, while the digital input is converted to an analog signal by a digital-to-analog converter. Note that in both cases the data is also recorded digitally on magnetic tape after being processed by the digital data multiplexer.

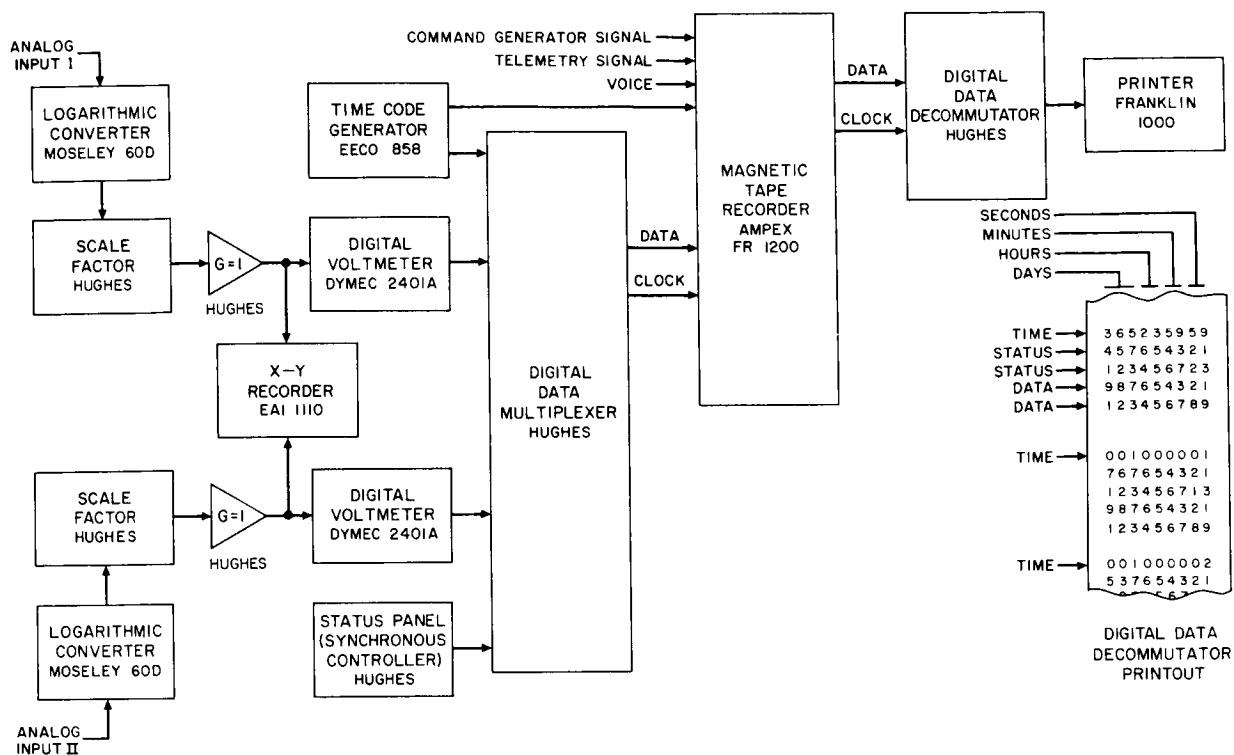


Figure 7-1. Data Recording Subsystem Type 1

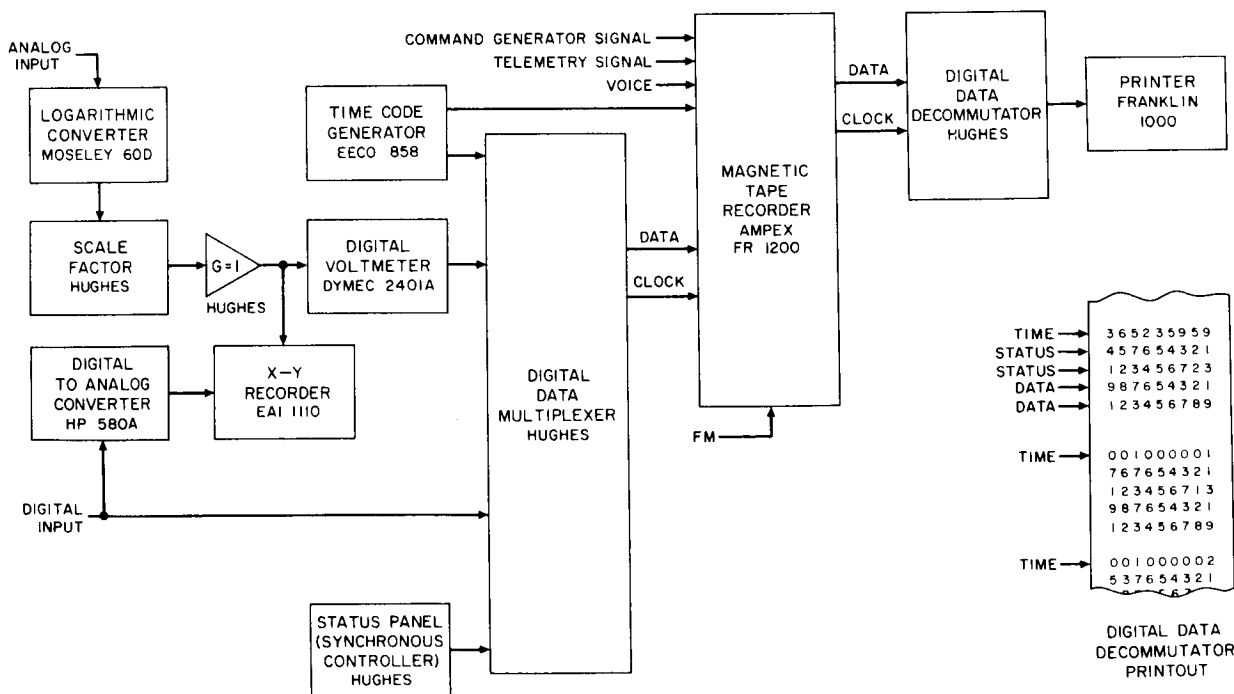


Figure 7-2. Data Recording Subsystem Type 6

Plots may also be obtained by rerunning the tape recorder through the digital data decommutator and the digital-to-analog converters as shown in Figure 7-3.

A proposed solution to the scale factoring problem is shown in Figure 7-4. A logarithmic converter and a scale factoring unit are used in conjunction with a multirange meter having an output which is proportional to the quantity being measured. The logarithmic converter and scale factoring unit produce an output proportional to the logarithm of the input signal and continuous over the full dynamic range of the input meter. This arrangement is useful in data recording of meter outputs where the dynamic range of the input signal is such that range changes of the input meter are necessary during the measurement period. As a result, a varying signal, requiring several range changes, can be recorded graphically in logarithmic form with no discontinuities except the transients developed during range selection.

The multirange meters used with the logarithmic converter produce voltages between 0 and 1 volt on each range setting that are proportional to the measured quantity. The meter range switch is coupled to a motor control unit which causes a stepping motor to follow the meter range switch. With the motor control unit, the meter may be remote from the scale factoring network. The meter ranges are such that each range change results in a 10-db measured voltage range change. The meter voltage output (0 to 1 volt) is fed to the logarithmic converter and results in an output of the converter proportional to the logarithm of the input voltage and varying between 0.0333 and 0.0666 volts for meter outputs ranging from 0.1 to 1 volt. The following amplifier, with a gain of 30, converts this output into voltages ranging from 1 to 2 volts. Thus, a 1-volt change at the amplifier output corresponds to a 20-db change in the meter output, and, consequently, a 10-db change at the meter output causes a 0.5 volt variation in the amplifier output. The scale factor unit at the output of this arrangement adds dc voltages to, or subtracts them from, the output of the amplifier in 0.5-volt steps as a function of the input meter range selector position. Since the added or subtracted 0.5 voltage is programmed so that it cancels the effect of any 10-db input meter range change, an essentially continuous output voltage is maintained. This output is proportional to the logarithm of the measured quantity over the full dynamic range of the input meter.

TELEMETRY AND COMMAND SYSTEM AND CONTROL ITEM TEST EQUIPMENT

No problems have been encountered in using the PACE module tester for testing the telemetry encoder modules. New loads and matchboards are now being built to be used with the new modules.

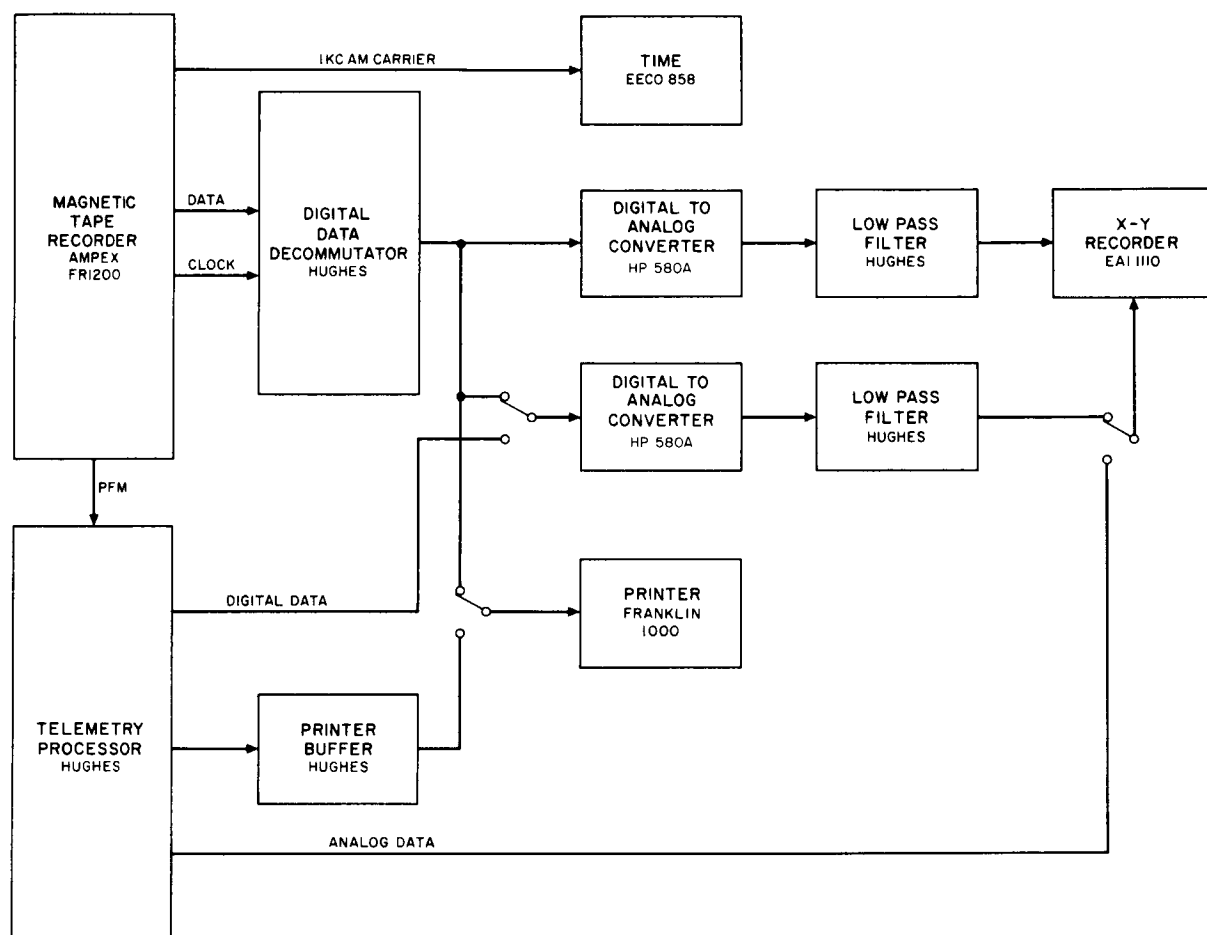


Figure 7-3. Data Recording Subsystem Type 14

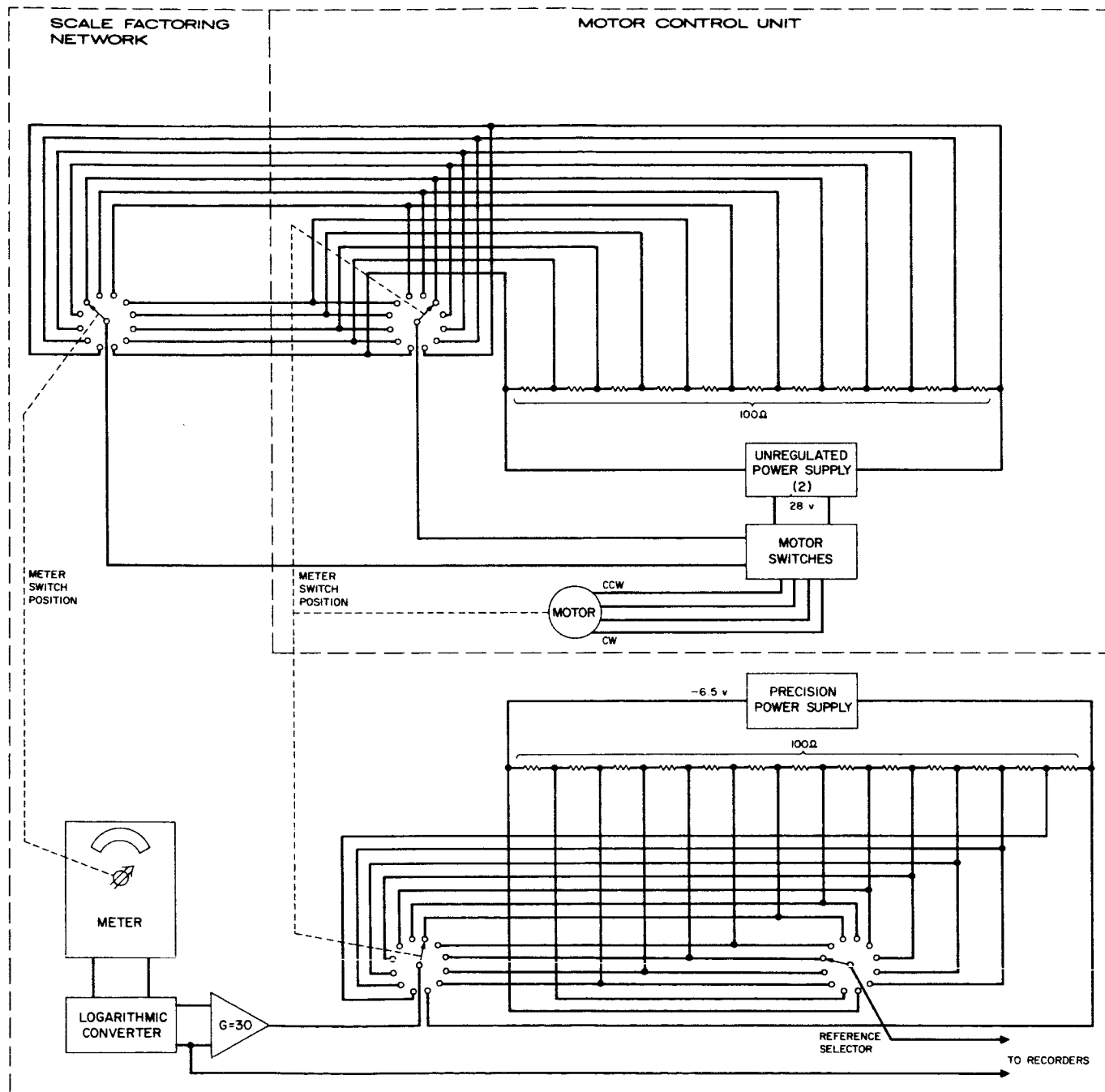


Figure 7-4. Logarithmic Converter

The major effort during December by test personnel was expended on writing checkout procedures for the encoder modules. Procedures now exist for twelve types of modules out of a total of sixteen now being designed.

The PACE unit tester has been slightly modified to make it compatible with the reworked phase shifter drivers. An extension cable is being assembled which will be used to connect the phase shifter drivers to the unit tester so that this unit may be driven by the PACE.

COMMUNICATION SYSTEM AND CONTROL ITEM TEST EQUIPMENT

Effort during this period has been concentrated on measurement and refinement of the transponder test equipment, particularly to determine and reduce contribution of the test equipment to the measured intermodulation and delay distortion.

Transponder Test Equipment Evaluation

Delay distortion and intermodulation distortion tests were performed on the transponder test set receiver (FT mode) to evaluate the divide-by-2 and divide-by-32 circuits. The results of the delay distortion tests as shown in Figures 7-5 and 7-6 were compared to a superheterodyne receiver using a mixer and local oscillator chain made up of spacecraft components. The two receivers produced the same maximum delay distortion, but the delay in the superheterodyne receiver increases monotonically with frequency and is therefore easier to compensate.

The intermodulation tests were performed with a Marconi OA1249B white noise test set. The modulation index was set to give a 25 mc bandwidth at the received frequency. The results are shown in Table 7-1.

TABLE 7-1. INTERMODULATION TESTS

Notch Center Frequency, kc	Noise Power Ratio, db	
	Divider Receiver	Superheterodyne Receiver
105	16	34
534	30	38
1002	29	37.5
2438	20	32.5
3886	22	28

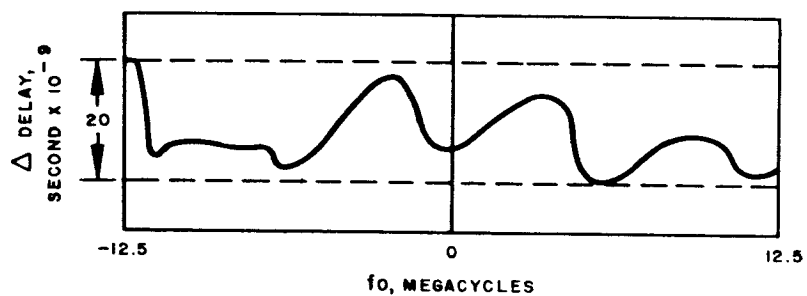


Figure 7-5. Divider Chain

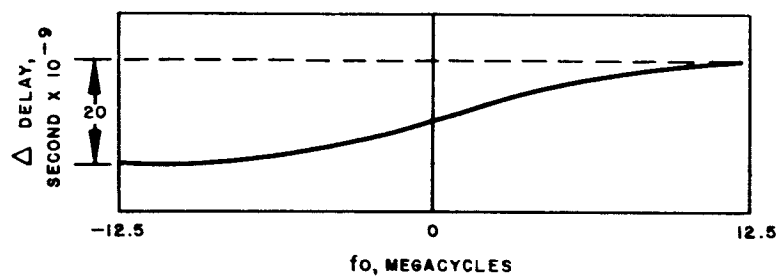


Figure 7-6. Superheterodyne Receiver

The low NPR in the divider receiver at 105 kc is probably due to receiver internal noise.

70-MC IF Amplifier, Limiter and Discriminator

To minimize intermodulation noise that may have been caused by the nonlinearity of transistors in the 70-mc IF system, it is planned that system tests will be made with a 70-mc IF amplifier and discriminator employing vacuum tubes instead of transistors. To accomplish this, modifications are being made in an existing 70-mc IF amplifier and discriminator system that employs vacuum tubes, to change the bandwidth from 12 to 25 mc. These modifications have required considerable effort because of the high degree of linearity required of the discriminator. The modifications are now 90 percent complete.

HANDLING EQUIPMENT

During the reporting period basic handling concepts were formulated and design criteria for required items of equipment were developed. The following is a description of the items of ground handling equipment which were investigated and will be used to support the subject program.

Mobile Assembly Fixture

To substantially reduce the cost, as well as ensure a well integrated fixture, the following alternate design is proposed.

A modified universal balance positioner made and patented by the Aronson Machine Co. of Arcade, New York will be used to facilitate assembly of components within the space frame, performance of various systems tests and checkout operations, as well as positioning of the spacecraft as required for transfer to weight, center of gravity and moment of inertia equipment. The positioner will consist of a pivoted work arm to which a work table is attached. The work table and the work arm may be rotated about their respective axes. In addition, the work arm may be tilted. The spacecraft will be mounted on the work table with its spin axis coinciding with the rotational axis of the work head, thus placing the spacecraft center of gravity on the axis of the work table. A simple adjustment of a worm on a worm gear sector will change the angle of the work arm, allowing its rotational axis to also intersect the spacecraft's center of gravity. With both axes intersecting the center of gravity, the spacecraft may be rotated with a minimum of effort, and may be put and locked in any desired position. The work head will be attached to the work arm through adjustable parallel linkage which will permit tilting of the spacecraft as desired, relative to the axis of the work arm. A sturdy steel frame will support the fixture and will be equipped with wheels for mobility within the work area. Brakes will be provided to secure the fixture in a desired location.

Transportation Trailer

Movement of spacecraft between buildings within the plant area and at the Atlantic Missile Range (AMR) will be accomplished using a specially designed cart. Tubular steel structure supports a spacecraft mounting flange. A special well attached to the flange will be provided for the protection of the antenna. A "V" type clamp will be used to assure secure attachment of spacecraft. Aerol banjo type running gear or its equivalent will be used, incorporating pneumatic tire wheels and cable actuated brakes. The cart will be steerable and will be equipped with a towbar. Jacks will be provided for leveling of the cart.

Sling

An existing sling developed for the T-1 version of the spacecraft will be used. The motor may be hoisted and suitable adapters will permit the hoisting of the spacecraft from either end. The sling consists of a spreader bar to which four cables are attached through coil springs in compression. This permits an even distribution of the load and helps to reduce shock caused by erratic operation of a hoist.

Apogee Motor Stand

Existing motor stand may be used for temporary storage within the assembly area. The stand was designed during the T-1 spacecraft program.

Spacecraft Shipping Container

Spacecraft shipping container will generally follow the design philosophy used with Syncom. The spacecraft with its protective devices attached and encased in a polyethylene bag will be attached to a shock mounted pallet which will form the base of the container. The sides and lid will be attached to the base and will be bolted or clamped together. Forklift pockets and lift points will be provided. The wood container will be of general dimensions compatible with commercial aircraft cargo space and will protect the spacecraft from shock inputs of 15 g.

Dynamic Balance

Equipment described by specification number S2-203-2 "Preliminary Equipment Specification Spin Balance Machine Advanced Syncom System Test" will be used with necessary modification.

Weight, Center of Gravity, and Moment of Inertia Equipment

Special adapters which will attach to the separation plane and motor mounting flange of the SAGGE and SASSE configurations will be used for moment of inertia measurement, employing the bifilar method of suspension.

When suspended from lead cells, weight and center of gravity location may be determined. A cradle will be used with MAGGE configuration to determine weight and center of gravity since there is no mounting area available at the forward end of the spacecraft. Center of gravity location will be found by placing the cradle on two scales. Two hoists will be used to rotate the cradle from the horizontal to the vertical position.

Spin Test Fixture

Systems tests on a spinning spacecraft will be performed using a modified existing design Drawing X209817. Extent of modification will be determined as test requirements are defined.

Alignment Equipment

Alignment equipment to be provided are jet alignment mandrels, and sun sensor alignment equipment. Proven methods of jet alignment will be used, employing mandrels which will reproduce the geometrical axes of the nozzles, permitting measurement which will be accomplished by optical means. A theodolite will also be used for the alignment of solar sensors. Method of gravity-gradient boom alignment cannot be determined at this time because there is no definite engineering data available as yet.

Miscellaneous

Additional shipping and protective devices will be provided as needed for various components such as antenna, ground planes, and similar parts. Spares containers will also be provided as the requirements develop.

8. PROJECT REFERENCE REPORTS

- * P. A. Rubin, "Frequency Comparison for Synchronous Orbit Navigation Satellite," IDC, 9 December 1963.
- * Planning Research Corporation, Technical Progress Report, "A Reliability Study for the Advanced Syncom Satellite Project (ATD Phase)," period ending 31 October 1963, dated 15 November 1963.
- * P. J. Sengstock, "Phase I Tests of Bipropellant Injector Solenoid Valves, Advanced Syncom," Hughes Technical Memorandum, 10 October 1963.
- * "Advanced Syncom Semiconductor Irradiation Tests," Hughes Technical Memorandum, 25 November 1963.
- * L. H. Grasshoff, "Preliminary Evaluation of Several Satellite Configurations for Gravity-Gradient Stabilization," IDC, 29 November 1963.
- * P. E. Norsell, "Goddard Space Flight Center, Stabilization and Control Branch, Report No. 82; Thermo Electric Valve Control Jet for Advanced Syncom," IDC, 30 December 1963.
- * G. L. Schackne, "Advanced Syncom Solar Panel Vibration Test Results and Evaluation," IDC, 9 December 1963.
- * P. E. Norsell, "Technical Development Plan Outline," IDC, 28 December 1963.
- * J. P. Wrzesinski, "Advanced Syncom Gravity-Gradient Version, Design Objectives and Design Requirements," IDC, 6 December 1963.
- * "Alternate Experiment Packages for Advanced Syncom," Advanced Syncom Project Bulletin No. 13, December 1963.
- * "Transmission of Wideband Analog Data from TV Cameras Included in Alternate Mission Packages for Advanced Syncom," Advanced Syncom Project Bulletin No. 14, 5 December 1963.

- * "Coordinate Systems and Reference Axes," Advanced Syncom Project Bulletin No. 15, 6 December 1963.
- * L. A. Gustafson, "GSFC Review of Bipropellant Report," 16 December 1963.
- * Specification X281283 (Preliminary) "Advanced Syncom Reaction Control System for Initial Station Positioning, Spin Stabilized Vehicles," 26 December 1963.
- * Statement of Work No. X281282 (Preliminary) "Initial Station Positioning, Mono-Propellant Reaction Control System, Advanced Syncom Spacecraft," 26 December 1963.
- * L. P. Birindelli, "Attitude Dispersion Due to Tipoff and Initial Tumbling Rate," IDC, 27 December 1963.
- * R. W. Highland, "Factory-to-Launch Procedures for Agena-D Vehicle," IDC, 13 November 1963.
- * R. W. Highland, "Information Regarding Payload Checkout Procedures for Agena-D Launchings," IDC, 21 November 1963.
- * L. A. Gustafson, "Trip Report - Visit to GFSC to Discuss Alternate Packages - 10-12 December 1963," IDC, 19 December 1963.
- * G. Gerson, "Advanced Syncom Telemetry Encoder Subcarrier Oscillator," IDC, 17 December 1963.
- * F. B. Bjorklund, "Advanced Syncom Design Review - Thermal Control," IDC, 17 December 1963.
- * M. J. Neufeld, "Micro-Thrusting Intervals for Small Eccentricity Changes of Near-Circular Orbits," IDC, 12 December 1963.
- * P. E. Norsell, "Payload Information from LMSC for Atlas D/Agena-D Injection into 6000 n.mi. Circular Orbit Altitude," IDC, 16 December 1963.
- * D. D. Williams, "Balancing as a Linear Programming Problem," IDC, 11 December 1963.
- * P. E. Norsell, "Agenda for NASA Design Review, Advanced Syncom, 18-20 December 1963," IDC, 16 December 1963.